

## **INFORMATION TO USERS**

**This manuscript has been reproduced from the microfilm master. UMI films the text directly from the original or copy submitted. Thus, some thesis and dissertation copies are in typewriter face, while others may be from any type of computer printer.**

**The quality of this reproduction is dependent upon the quality of the copy submitted. Broken or indistinct print, colored or poor quality illustrations and photographs, print bleedthrough, substandard margins, and improper alignment can adversely affect reproduction.**

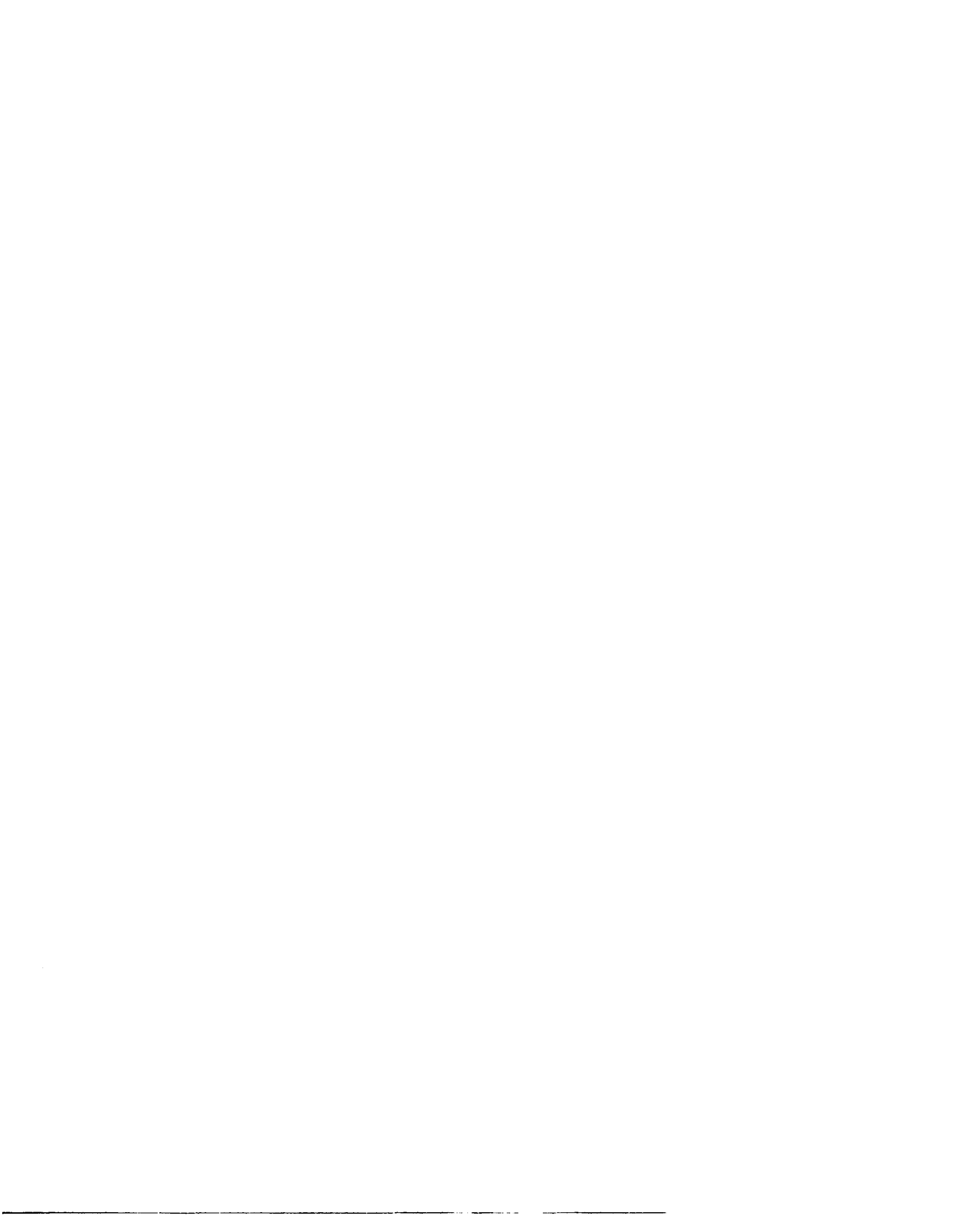
**In the unlikely event that the author did not send UMI a complete manuscript and there are missing pages, these will be noted. Also, if unauthorized copyright material had to be removed, a note will indicate the deletion.**

**Oversize materials (e.g., maps, drawings, charts) are reproduced by sectioning the original, beginning at the upper left-hand corner and continuing from left to right in equal sections with small overlaps. Each original is also photographed in one exposure and is included in reduced form at the back of the book.**

**Photographs included in the original manuscript have been reproduced xerographically in this copy. Higher quality 6" x 9" black and white photographic prints are available for any photographs or illustrations appearing in this copy for an additional charge. Contact UMI directly to order.**

# **U·M·I**

University Microfilms International  
A Bell & Howell Information Company  
300 North Zeeb Road, Ann Arbor, MI 48106-1346 USA  
313/761-4700 800/521-0600



Order Number 9300349

**X-ray photoelectron diffraction studies of structural and  
magnetic disordering transitions near surfaces**

Tran, Thuy Thu, Ph.D.

University of Hawaii, 1992

**U·M·I**  
300 N. Zeeb Rd.  
Ann Arbor, MI 48106

---



**X-RAY PHOTOELECTRON DIFFRACTION STUDIES OF STRUCTURAL  
AND MAGNETIC DISORDERING TRANSITIONS NEAR SURFACES**

**A DISSERTATION SUBMITTED TO THE GRADUATE DIVISION OF THE  
UNIVERSITY OF HAWAII IN PARTIAL FULFILLMENT OF THE  
REQUIREMENTS FOR THE DEGREE OF**

**DOCTOR OF PHILOSOPHY**

**IN**

**CHEMISTRY**

**AUGUST 1992**

**BY**

**Thuy T. Tran**

**Dissertation Committee:**

**Charles S. Fadley, Chairperson  
Thomas T. Bopp  
Roger E. Cramer  
John W. Gilje  
Richard G. Inskeep  
Pui K. Lam**

## ACKNOWLEDGEMENTS

I would like to thank Professor Charles S. Fadley for his expert advice, guidance, and support over the years. Without his ingenuity in planning the different stages of the research projects and his valuable suggestions in data analysis, none of this work would have materialized. I have been very fortunate to have worked with and learned from three extremely talented post-doctoral associates; my sincere appreciation and admiration go to Daniel J. Friedman, Suntharampillai Thevuthasan, and Juerg Osterwalder. I also would like to thank Yongjoo Kim for his contributions to the study of structural disordering on Ge, and the support staff of the Chemistry Department, especially Dave Kempton, for their assistance. Finally, Gregory S. Herman is the person who has made these seven years of graduate school bearable. Thank you!

## ABSTRACT

This thesis deals with order/disorder transitions near solid surfaces as studied by x-ray photoelectron diffraction and photoelectron holography. Transitions involving both atomic positional order and magnetic order have been studied.

Further evidence for a reversible high-temperature surface-disordering phase transition on Ge(111) has been found using Ge 3p x-ray photoelectron diffraction (a short-range-order probe of surface structure that is sensitive to the first 3-5 spheres of neighbors) and photoelectron holography (a recently suggested direct 3-d imaging technique). Azimuthal diffraction data at takeoff angles with respect to the surface of  $\theta=19^\circ$  (including nearest-neighbor forward scattering directions and yielding high surface sensitivity) and  $\theta=55^\circ$  (for which second-nearest-neighbor forward scattering directions and more bulk sensitivity are involved) show abrupt drops in intensity of ~30%-40% over the temperature interval of 900-1200 K. Photoelectron holographic near-neighbor images at temperatures both below and above the transition region furthermore indicate an identical near-neighbor structure for all atoms present in ordered sites. These combined diffraction and holography data show that by 1200 K, the Ge(111) surface is covered by a completely disordered overlayer of about 2 Ge monolayers in thickness. The rate of growth of this overlayer with increasing temperature is also in excellent agreement with recent medium-energy ion scattering results, although the thickness we find for the overlayer is 1.5-2.0x larger than that derived from ion scattering. Based on these data, a disordering model for the Ge(111) surface phase transition occurring at 1050 K is discussed.

Spin-polarized photoelectron diffraction is a recently developed and promising application of photoelectron diffraction to the study of the magnetic structure near surfaces. This technique is based on an internal source of spin-polarized electrons as produced in

core-level multiplet splittings and it is thus sensitive to the short-range magnetic order around a given type of emitter in the crystal. In prior studies, it has been applied to two antiferromagnets,  $\text{KMnF}_3$  and  $\text{MnO}$ , and the effects seen at temperatures well above the Néel (or long-range-order) temperature have been attributed to an abrupt loss of short-range order. In this thesis, data on  $\text{MnO}$  have been extended to include the use of synchrotron radiation at photon energies of 150, 170, and 190 eV. Attempts to measure similar effects on two ferromagnets, Fe and Gd, were also made; these yielded preliminary results that should be useful for future studies.

## TABLE OF CONTENTS

<b>ACKNOWLEDGEMENTS.....</b>	<b>iii</b>
<b>ABSTRACT .....</b>	<b>iv</b>
<b>LIST OF TABLES .....</b>	<b>viii</b>
<b>LIST OF FIGURES.....</b>	<b>ix</b>
<b>LIST OF ACRONYMS .....</b>	<b>xvi</b>
<b>1. Introduction.....</b>	<b>1</b>
<b>References .....</b>	<b>8</b>
<b>Figures.....</b>	<b>10</b>
<b>2. Experimental Methods.....</b>	<b>17</b>
<b>References .....</b>	<b>20</b>
<b>Figures.....</b>	<b>21</b>
<b>3. Theoretical Methods .....</b>	<b>23</b>
<b>References .....</b>	<b>34</b>
<b>Tables .....</b>	<b>35</b>
<b>Figures.....</b>	<b>37</b>
<b>4. Structural Disorder: Photoelectron Diffraction and Photoelectron Holography Study of A Ge(111) High- Temperature Surface Phase Transition .....</b>	<b>44</b>
<b>4.1 A Preliminary Examination.....</b>	<b>44</b>
<b>References.....</b>	<b>50</b>

<b>Figures</b> .....	<b>52</b>
<b>4.2 A Detailed Investigation</b> .....	<b>55</b>
4.2.1 Introduction.....	55
4.2.2 Experimental.....	59
4.2.3 Results .....	60
4.2.4 Discussion .....	66
4.2.5 Summary.....	76
<b>References</b> .....	<b>78</b>
<b>Figures</b> .....	<b>81</b>
<b>5. Magnetic Disordering: Spin-Polarized Photoelectron Diffraction on MnO and Preliminary Results with Possible Future Applications to Fe and Gd</b> .....	<b>89</b>
<b>5.1 Introduction</b> .....	<b>89</b>
<b>5.2 Experimental</b> .....	<b>92</b>
<b>5.3 Results and Discussion</b> .....	<b>94</b>
5.3.1 MnO(001).....	94
5.3.2 Fe(001).....	96
5.3.3 Gd (polycrystalline) .....	98
<b>5.4 Conclusions</b> .....	<b>99</b>
<b>References</b> .....	<b>100</b>
<b>Tables</b> .....	<b>101</b>
<b>Figures</b> .....	<b>102</b>
<b>6. Concluding Remarks</b> .....	<b>108</b>

## LIST OF TABLES

Table 3.1	A sample input file for a SSC calculation.....	35
Table 3.2	Treatment of vibrational effects at the surface and in the bulk.....	36
Table 5.1	Intensity ratio, $R$ , and spin asymmetry, $S_{\text{expt}}$ , from Mn 3s versus temperature, listed in the time sequence the data points were taken .....	101

## LIST OF FIGURES

- Fig. 1.1 The two basic modes of photoelectron diffraction are scanned-angle PD and scanned-energy PD. In the scanned-angle mode, the polar,  $\theta$ , and azimuthal,  $\phi$ , emission angles can be varied. In the scanned-energy mode (also known as angle-resolved photoemission fine structure or ARPEFS), the emission direction is kept fixed while the photon energy is changed. This mode thus requires synchrotron radiation. ....10
- Fig. 1.2 X-ray photoelectron valence-band spectra at 295 K and 803 K from the W(110) surface at a polar angle of  $\theta=45^\circ$  taken over the azimuthal range of  $\phi=0^\circ-90^\circ$  in  $1.8^\circ$  steps. ....11
- Fig. 1.3 X-ray photoelectron spectra showing elastic and inelastic peaks in W 4f emission from W(110) and Ge 3d emission from Ge(111). ....12
- Fig. 1.4 Azimuthal scans of the elastic intensity and its associated plasmon loss intensity, together with the normalized ratio of the plasmon loss intensity to the elastic intensity for W 4f and Ge 3d, both at the polar angle of  $\theta=55^\circ$ ....13
- Fig. 1.5 Projection of the  $\chi(\vec{k})$  hologram for Si 2p emission from Si(111) at 1388 eV onto the  $k_x$ - $k_y$  plane; hologram opening angle  $\alpha=172^\circ$ . (a) Experiment, with several low-index directions labeled. (b) Experiment, with Gaussian removal of forward scattering intensities along low-index directions marked in (a). (c)

As (a), but for full scattering strength single scattering (SS) theory. (d) As (b), but for full scattering strength SS. ....14

Fig. 1.6 Fourier transform contour plots of the  $\chi(\vec{k})$  data in Fig. 1.5 in the horizontal  $z=3.13 \text{ \AA}$  plane. (a) Experiment. (b) Experiment, with Gaussian removal of forward scattering intensities along low-index directions. (c) As (a), but for full scattering strength SS. (d) As (b), but for full scattering strength SS. . 15

Fig. 1.7 Comparison between experimental scans taken at  $\theta=19^\circ$  and single scattering (SS) theoretical curves obtained for both the A (cationic) and B (anionic) surface terminations of a  $\text{Hg}_{1-x}\text{Cd}_x\text{Te}(111)$  sample. The overall anisotropy as judged from  $(I_{\text{max}}-I_{\text{min}})/I_{\text{max}}$  in % is also indicated for each curve. R factor values are also included to indicate the goodness of fit. It is typical in such analyses for theory to predict a significantly higher anisotropy than is observed, with reasons being the presence of surface disorder, the presence of an amorphous layer of surface impurities, and/or multiple scattering effects such as defocussing along low-index directions.....16

Fig. 2.1 Data for Ge 3d emission as obtained from the Hewlett-Packard 5950A spectrometer showing the detailed temperature dependence of the height of the nearest-neighbor forward scattering peak along  $\theta=19^\circ$ ,  $\phi=0^\circ$ . Upright triangles represent increasing temperature and inverted triangles decreasing temperature. Angular resolution is  $\sim\pm 3.6^\circ$ .....21

Fig. 2.2	Data similar to those shown in Fig. 2.1 but for Ge 3p emission and as obtained from the Vacuum Generators ESCALAB5 spectrometer. Angular resolution is $\pm 3.0^\circ$ (single aperture).....	22
Fig. 3.1	Illustration of the origin of the diffraction features expected as a result of emission from a 2-atom chain, with the 0 <sup>th</sup> order (forward scattering) peak and the higher-order peaks labeled. The scattering phase shift is, for simplicity, assumed to be zero.....	37
Fig. 3.2	The magnitude of the atomic scattering factor $ f(\theta) $ for Cu as a function of scattering angle $\theta$ for various electron kinetic energies from 500 to 10,000 eV. Note the enhanced forward peaking as energy increases and the concomitant decrease in the importance of any backscattering.....	38
Fig. 3.3	The scattering phase shift $\Psi(\theta)$ for Cu as a function of scattering angle $\theta$ for various electron kinetic energies from 500 to 10,000 eV.....	39
Fig. 3.4	Single and multiple scattering calculations of Ge 3d photoelectron diffraction at 1457.0 eV from linear Ge [111] chains. The emitter is at one end of the chain (from Refs. 9 and 11).....	40
Fig. 3.5	(a) Total Ge 3d photoelectron diffraction intensity from linear Ge [111] chains at 1457.0 eV as a function of the number of atoms in the chain. (b) The percent defocussing in 3d photoelectron diffraction intensity based upon the results of (a).....	41

Fig. 3.6	Chain configurations used in multiple scattering calculations for the two forward scattering directions at $\theta=19^\circ$ and $55^\circ$ .....	42
Fig. 3.7	Results from multiple scattering calculations on chains of up to ten Ge atoms at $\theta=19^\circ$ and $55^\circ$ . Intensities from a single emitter (left panels) as well as from the sum of all emitters (right panels) are shown, with the point at which the summed total intensity from the chain converges being indicated as "~conv.".....	43
Fig. 4.1.1	(a) An unreconstructed Ge(111) surface showing nearest-neighbor and second-nearest-neighbor scattering directions at takeoff angles of $\theta=19^\circ$ and $\theta=55^\circ$ with respect to the surface; $\phi=0^\circ$ ( $[11\bar{2}]$ azimuth) for both of these directions. (b) Temperature-dependent azimuthal XPD data for Ge 3p emission from Ge(111) at 1365 eV and a low takeoff angle of $\theta=19^\circ$ . (c) As (b), but for a takeoff angle of $\theta=55^\circ$ .....	52
Fig. 4.1.2	(a) The temperature dependence of the height of the nearest-neighbor forward scattering peak in Fig. 4.1.1(b) along $\theta=19^\circ$ , $\phi=0^\circ$ . Also shown are the temperature dependence of the background intensity under the forward scattering peak and the intensity expected on the basis of Debye-Waller effects in a single scattering cluster model. (b) As (a), but for the next-nearest-neighbor forward scattering peak in Fig. 4.1.1(c) along $\theta=55^\circ$ , $\phi=0^\circ$ .....	53

Fig. 4.1.3 (a) Projection of the experimental  $\chi(\vec{k})$  for Ge(111) at 970 K onto the  $k_x$ - $k_y$  plane. Several low-index directions are labeled. (b) As (a), but at 1130 K. (c), (d) Horizontal FT contour plots in the  $z=3.27 \text{ \AA}$  plane obtained with Gaussian removal of forward scattering intensities along low-index directions in the initial  $\chi(\vec{k})$  functions of (a), (b). Contour plots are shown at (c) 970 K and (d) 1130 K.....54

Fig. 4.2.1 (a) An unreconstructed Ge(111) surface showing nearest-neighbor and second-nearest-neighbor scattering directions at takeoff angles of  $\theta=19^\circ$  and  $\theta=55^\circ$  with respect to the surface;  $\phi=0^\circ$  ( $[11\bar{2}]$  azimuth) for both of these directions. Note the two symmetry-inequivalent emitter types. (b) Temperature-dependent azimuthal XPD data for Ge 3p emission from Ge(111) at 1365 eV and a low takeoff angle of  $\theta=19^\circ$ . (c) As (b), but for a takeoff angle of  $\theta=55^\circ$ .....81

Fig. 4.2.2 (a) Temperature dependence of the background intensity under the nearest-neighbor forward scattering peak in Fig. 4.2.1(b) along  $\theta=19^\circ$ ,  $\phi=0^\circ$ . (b) The temperature dependence of the height  $\Delta I = I_{\text{peak}} - I_{\text{background}}$  of the same nearest-neighbor forward scattering peak.  $\Delta I(T)$  values are plotted as a percentage of the room temperature value. Also shown in (b) is the intensity expected on the basis of Debye-Waller effects in a single scattering cluster model. (c) and (d) are as (a) and (b), but for the next-nearest-neighbor forward scattering peak in Fig. 4.2.1(c) along  $\theta=55^\circ$ ,  $\phi=0^\circ$ .....82

- Fig. 4.2.3 (a) Projection of the experimental  $\chi(\vec{k})$  for Ge(111) at 300 K onto the  $k_x$ - $k_y$  plane. (b) As (a), but at 970 K; several low-index directions are labeled. (c) As (a), but at 1130 K.....83
- Fig. 4.2.4 Horizontal FT contour plots in the  $z=3.27 \text{ \AA}$  plane obtained with Gaussian removal of forward scattering intensities along low-index directions in the initial  $\chi(\vec{k})$  functions of Fig. 4.2.3 (a-c). Contour plots are shown at (a) 300 K, (b) 970 K, and (c) 1130 K. ....84
- Fig. 4.2.5 Plot of  $\ln \hat{\Delta I} = \ln[\Delta I/W]$ , the vibrationally-corrected intensity change, versus  $\ln(T_m - T)$  for  $\theta=19^\circ$ ,  $\phi=0^\circ$  ( $\bullet$ ) and for  $\theta=55^\circ$ ,  $\phi=0^\circ$  ( $\square$ ).....85
- Fig. 4.2.6 (a) XPD and MEIS data plotted as measured overlayer thickness (ML) versus temperature. (b) As in (a) but with XPD and MEIS curves normalized to the same maximum and minimum values. (MEIS data from Ref. 14).....86
- Fig. 4.2.7 Plot of the change in free energy,  $\Delta F$ , as a function of overlayer thickness at 1050, 1125, and 1200 K, as calculated with the model of Mikheev and Chernov [15].....87
- Fig. 4.2.8 (a) The ratio of the average total absolute intensity of each azimuthal scan taken at 1130 K to that of each corresponding azimuthal scan for the same polar angle taken at 970 K. (b) Overall anisotropies from our holography data at 300, 970, and 1130 K plotted versus  $1/\sin\theta$ . (c)

$\ln[\hat{\Delta}(1130\text{K})/\hat{\Delta}(970\text{K})]$  versus  $1/\sin\theta$ ; the best-fit straight line through the data points has a slope of  $-d/\lambda_e = -0.104$ . .....88

Fig. 5.1 (a) The multiplet-split Mn 3s spectrum of  $\text{KMnF}_3$ , with the initial and final states and the predominant photoelectron spin orientations indicated (from Ref. 3). (b) Spin-integrated (solid line) and spin-resolved (dashed lines) Fe 3s photoemission spectra after subtraction of background and averaging over the data points (from Ref. 5). ..... 102

Fig. 5.2 The temperature dependence of Mn 3s spin asymmetries  $S_{\text{expt}}$  for MnO taken with standard Mo  $M\zeta$  radiation (■, ▲) and with synchrotron radiation (○).103

Fig. 5.3 The spin-up/spin-down intensity ratio for the Mn 3s level of MnO as a function of polar angle, taken at three temperatures 373 K (◆), 473 K (■), and 573 (●)..... 104

Fig. 5.4 The temperature dependence of Mn 3s spin asymmetries  $S_{\text{expt}}$  for MnO taken with synchrotron radiation at  $h\nu$  of 150 eV (■) and 170 eV(●)..... 105

Fig. 5.5 Fe 3s spectra taken four times and at two different temperatures (room temperature and 1106 K) during a single run: (1)=initial room temperature, (2)=first 1106 K, (3)=second 1106 K, and (4)=final room temperature. . . 106

Fig. 5.6 (a) Gd 4s doublet and (b) Gd 5s doublet, as excited by Al  $K\alpha$  radiation. . 107

## LIST OF ACRONYMS

AES	Auger electron spectroscopy
AED	Auger electron diffraction
ARPEFS	Angle-resolved photoemission fine structure
DW	Debye-Waller
FT	Fourier transform
HP	Hewlett-Packard
HWHM	Half-width at half-maximum
IPD	Inelastic photoelectron diffraction
LEED	Low-energy electron diffraction
MD	Molecular dynamics
MEIS	Medium-energy ion scattering
ML	Monolayer
MS	Multiple scattering
PD	Photoelectron diffraction
PH	Photoelectron holography
SM	Surface melting
SPPD	Spin-polarized photoelectron diffraction
SPT	Surface phase transition
SS	Single scattering
SSC	Single scattering cluster
STM	Scanning tunneling microscopy
UHV	Ultra-high vacuum
VG	Vacuum Generators

**XPD** X-ray photoelectron diffraction  
**XPS** X-ray photoelectron spectroscopy

# Chapter 1

## Introduction

*'Disorder is not mere chaos: it implies defective order'*

-J.M. Ziman

To describe a disordered state, it is first necessary to begin with the ordered state from which deviations occur. The perfect order found in a three-dimensional crystal can be altered by changes in the physical conditions of its surroundings. One simple type of disorder consists of forming a surface: that is, effectively splitting the crystal in two along some plane. This dissertation examines two additional types of disorder, structural and magnetic, that can occur near crystalline solid surfaces as a function of temperature. In the first case, it has been found that the Ge(111) surface undergoes a surface structural disordering phase transition near 1050 K, or 160 K below its bulk melting point. The idea of a temperature-dependent re-arrangement of the Ge(111) surface structure was first suggested by Lever [1] based on a marked drop in the oxygen sticking coefficient beginning at approximately 1050 K. The first actual observation of a high-temperature structural phase transition was made by McRae and coworkers [2] using temperature-dependent low-energy electron diffraction (LEED). Further evidence for this reversible process and a proposed model of the disordering associated with it will be presented in Chapter 4. In the second case, abrupt short-range-magnetic-order transitions have been observed previously in the two antiferromagnets  $\text{KMnF}_3$  [3] and  $\text{MnO}$  [4] at temperatures well above their long-range-order or Néel temperatures. An extension of prior work on  $\text{MnO}$  to include synchrotron radiation measurements, an attempt to detect similar transitions

in the ferromagnet Fe, and preliminary data on Gd in preparation for future studies will be described in Chapter 5.

Photoelectron diffraction (PD) is a widely used probe of surface structure. Complete reviews of this technique including descriptions of the photoemission process and experimental as well as theoretical aspects can be found elsewhere [5]. The basic process involves exciting a core photoelectron with a flux of nearly monoenergetic radiation  $h\nu$ , and measuring resulting intensity modulations as a function of either emission direction or  $h\nu$  that are due to scattering from atoms neighboring the emitter. The photoelectric equation describing energy conservation is:

$$h\nu = E_b^V(k) + E_{kin} \quad (1.1)$$

where  $E_b^V(k)$  is the binding energy of the  $k^{\text{th}}$  level with respect to the vacuum level and  $E_{kin}$  is the photoelectron kinetic energy. Because a core-level is excited, the measurement is atom-specific: that is, emitters of each atomic number in the sample can be studied separately. Since PD is primarily sensitive to the first three to five spheres of neighbors around each emitter, it is a short-range probe of the local environment around a given type of emitter. For the studies in this dissertation, three different variations of PD were used: x-ray photoelectron diffraction (XPD), photoelectron holography (PH), and spin-polarized photoelectron diffraction (SPPD). There are two modes of XPD, as illustrated in Fig. 1.1. Scanned-angle XPD, performed with a conventional fixed-energy x-ray source, involves measuring the angular distribution of a particular photoelectron intensity while varying either or both the two electron emission angles: the polar angle  $\theta$  (here defined relative to the surface) and the azimuthal angle  $\phi$ . The majority of the data in Chapter 4 is of this type. In the second mode of XPD, the photon energy of the incident x-rays is allowed to vary

while the electron emission direction is kept fixed. A portion of the data in Chapter 5 is of this type. PH, a new variation on XPD, was also used to study the Ge(111) high-temperature structural disordering phase transition in Chapter 4. This technique stems from suggestions first made by Szoeké [6] and later elaborated at a theoretical level by Barton [7] that the angular distributions of photoelectrons or Auger electrons above a single crystal surface form holograms which can be inverted via a two-dimensional Fourier transform (FT) to yield direct images of atomic structure. Tonner, Saldin, and co-workers [8] for the first time showed this procedure to be promising for the analysis of experimental data. In particular, they found that certain features in the images derived for both Auger emission and elastically back-scattered Kikuchi electrons can be associated with the positions of near-neighbor atoms of typical emitters in both the Cu lattice and an epitaxial overlayer of Cu on Ir(111) [8,9]. More recently, Herman and co-workers [10] have found that features in the holographic images for core-level photoelectrons from Si(111), a semiconductor with an open diamond lattice structure and two symmetry-inequivalent emitter types that is very similar to the Ge(111) studied in this thesis, also correspond to atomic positions. These few studies represent the first successful holographic images derived from experimental data to date. Finally, SPPD, used mainly to obtain the data in Chapter 5, is a promising probe of short-range magnetic order [3,4]. It measures spin-dependent scattering effects as produced by spin-split core level photoelectron peaks. No external spin detector is needed and the technique can be applied to specimens with no net magnetization such that studies of both antiferromagnets and ferromagnets should be possible.

Other than studies of structural and magnetic disorder in the surface and near-surface regions to be presented in this dissertation, the author also participated in four other surface science experiments which will be briefly described here. Valence photoelectron diffraction and direct-transition effects were examined by measuring the temperature dependence of

valence and core x-ray photoelectron intensities for W(110) [11]. Inelastic photoelectron diffraction was also studied by considering the diffraction patterns from W(110) and Ge(111) due to both inelastically-scattered electrons and elastically scattered electrons [12]. Photoelectron holography was applied, for the first time, to image near-neighbor atoms in the semiconductor Si [10]. Finally, the surface polarity of a  $\text{Hg}_{1-x}\text{Cd}_x\text{Te}(111)$  epitaxial surface was determined by XPD [13].

In the study of valence PD and direct transition effects, W(110) valence spectra, shown in Fig. 1.2 at ambient temperature (295 K) and high temperature (803 K), were taken as a series of energy scans at a constant polar angle of  $\theta=45^\circ$  and spanning an azimuthal range of  $\phi=0^\circ-90^\circ$  in  $1.8^\circ$  steps [11]. At 295 K, after normalization to the same maximum height for the 2.8 eV peak, significant oscillations in the height of the 5.3 eV peak as a function of azimuthal angle were observed. These oscillations are associated with direct-transition effects in valence emission due to the high Debye-Waller factor (W) of 0.55 (or equivalently the high percentage of direct transitions). At 803 K, however, the valence spectra are essentially constant with  $\phi$ , indicating the reduced effect of direct transitions due to a Debye-Waller factor of 0.20 at this temperature. That is, at the higher temperature, there is essentially complete Brillouin-zone averaging due to vibrational effects. In addition, temperature-dependent energy-integrated core and valence-band intensities were also measured as azimuthal scans of range  $200^\circ$  in  $\phi$  and at a polar angle of  $\theta=45^\circ$ . It was found that at 295 K, these curves were similar in form, but showed significant differences in fine structure. At 803 K, they retained differences due to the atomic-orbital character of the initial and final states involved.

Surface structure determinations via PD and Auger electron diffraction (AED) usually involve examining spectral features that arise from elastically scattered or "no loss" photoelectrons. In the second study, inelastic photoelectron diffraction (IPD) patterns

resulting from inelastically-scattered electrons were instead measured for W(110) and Ge(111) surfaces [12]. Figure 1.3 shows the elastic peaks and inelastic "plasmon" loss satellites at lower kinetic energy for both W 4f and Ge 3d emission. Corresponding elastic and inelastic azimuthal patterns at a polar angle of  $\theta=55^\circ$  are shown in Fig. 1.4. The ratio between the two normalized diffraction patterns in the lower panel of the figure indicates reductions in the inelastic intensities of 20% and 13% for the W 4f and Ge 3d curves, respectively, along forward scattering directions such as  $\langle 001 \rangle$  and  $\langle 11\bar{2} \rangle$ . This selective reduction of the inelastic peaks can be quantitatively explained by defocussing effects due to multiple elastic scattering. An additional observation deduced from this study is that the ratio  $I(\text{inelastic})/I(\text{elastic})$  can also serve as a means for identifying low-index directions above a surface.

In the third study, PH was applied to the Si(111) surface [10]. Theoretical considerations and experimental details were very similar to those used in the Ge(111) structural disordering phase transition study which are described fully in chapter 4. It suffices to summarize the Si(111) results and their interpretation here. The measured three-dimensional intensity distribution  $I(\vec{k})$  in the electron wave vector  $\vec{k}$ , with angles of emission  $\theta$  and  $\phi$ , was converted to a normalized  $\chi(\vec{k})$ . Figure 1.5 shows several experimental and calculated  $\chi(\vec{k})$  plots as projected down onto the  $k_x$ - $k_y$  plane. ( $k_z$  is along the surface normal.) The raw experimental data with several low-index directions labeled shown in Fig. 1.5(a) can be compared to the corresponding theoretical simulation using a curved-wave single scattering cluster approach shown in Fig 1.5(c). The theory curves overestimate certain low-index forward scattering features, especially with the  $\langle 110 \rangle$  directions, both in terms of intensity and angular width; otherwise, however, theory is found to yield a very good description of the remaining diffraction features. Figures 1.5(b) and 1.5(d) were obtained by multiplying Figs. 1.5(a) and 1.5(c), respectively, by a

Gaussian function of the form  $[1-\exp(-0.691\delta^2/\gamma^2)]$ , where  $\delta$  is the angular deviation of  $\vec{k}$  from a given low-index forward scattering axis and  $\gamma$  is a variable half-width at half maximum intensity (HWHM), empirically chosen here as  $7.5^\circ$  for all directions. This Gaussian multiplier is used to reduce non-ideal forward scattering effects that are known to cause aberrations in holographic images [14]. After a holographic inversion of the four  $\chi(\vec{k})$ 's in Fig. 1.5, the FT images obtained in the  $z=3.13 \text{ \AA}$  plane for which both Si emitter types are expected to yield strong features are shown in Fig. 1.6. The distances from the center of each of the images in Fig. 1.6 to one of the peaks labeled "a" are 4.83, 4.26, 4.56, and 4.57  $\text{\AA}$  for Fig. 1.6(a), 1.6(b), 1.6(c), and 1.6(d), respectively. These values are in good agreement with the distance of 4.42  $\text{\AA}$  in the known bulk lattice. However, an examination of the FT images at different  $z$  planes revealed that features associated with scatterers in the first double layer above that of a given emitter are significantly elongated along bond directions. Nonetheless, this study has shown for the first time that an approximate holographic imaging of the rather complex diamond structure of Si with two emitter types is possible, and we will apply this methodology in Chapter 4 to the study of the Ge surface phase transition.

Finally, the fourth study is a straightforward application of XPD to determining the surface polarity of  $\text{Hg}_{1-x}\text{Cd}_x\text{Te}(111)$ . Due to the lack of a center of symmetry in the zinc-blende structure, the  $\text{Hg}_{1-x}\text{Cd}_x\text{Te}(111)$  surface can exist as a cationic (type A) or an anionic (type B) surface. Full  $360^\circ$  azimuthal patterns for each of the Hg  $4f_{7/2}$ , Cd  $3d_{5/2}$ , and Te  $3d_{5/2}$  photoelectron peaks were obtained at each of the polar angles  $\theta=19^\circ$ ,  $35^\circ$ , and  $55^\circ$ . Figure 1.7 shows three of these azimuthal patterns for the case of  $\theta=19^\circ$  along with single scattering cluster (SSC) calculations for the two types of surface polarity. Overall anisotropy, defined as  $(I_{\max}-I_{\min})/I_{\max}$ , is also given for each curve. A comparison of the results from SSC calculations to the experimental data, using R factors as a quantitative

measure of the goodness of fit, led to an unambiguous assignment of the cationic termination to the sample used in the study and also provided means by which the different lattice sites of Cd, Hg, and Te could be clearly distinguished.

The remainder of this dissertation is organized as follows: In Chapter 2, the three experimental systems that were used to perform the measurements are discussed. In Chapter 3, theoretical considerations, beginning with the SSC approximation at the plane wave limit and extending to the full multiple scattering level with the inclusion of both inelastic scattering and vibrational effects, are examined. Chapter 4 covers various aspects of structural disordering as seen through a combined XPD and PH study of a Ge(111) high-temperature surface phase transition. Chapter 5 deals with various aspects of magnetic disordering as seen through a SPPD study on MnO and preliminary results with possible future applications to Fe and Gd. Finally, Chapter 6 gives the author's general impression and concluding remarks concerning the utility of XPD and its variants, PH and SPPD, as well as suggests future directions and possible extensions of the work presented in this dissertation.

## References

- [1] R.F. Lever, Surf. Sci. **9**, 370 (1968).
- [2] E.G. McRae and R.A. Malic, Phys. Rev. Lett. **58**, 1437 (1987); E.G. McRae and R.A. Malic, Phys. Rev. **B38**, 13163 (1988).
- [3] B. Sinkovic, B. Hermsmeier, and C.S. Fadley, Phys. Rev. Lett. **55**, 1227 (1985); B. Sinkovic, B. Hermsmeier, and C.S. Fadley, J. Magn. Magn. Mater. **54-57**, 975 (1986).
- [4] B. Hermsmeier, J. Osterwalder, D.J. Friedman, and C.S. Fadley, Phys. Rev. Lett. **62**, 478 (1989); B. Hermsmeier, J. Osterwalder, D.J. Friedman, B. Sinkovic, T. Tran, and C.S. Fadley, Phys. Rev. **B42**, 11895 (1990).
- [5] C.S. Fadley in *Electron Spectroscopy: Theory, Techniques, and Applications*, C.R. Brundle and A.D. Baker, Eds. (Academic Press, London, 1978) Vol. II, Ch.1; C.S. Fadley, Prog. Surf. Sci. **16**, 275 (1984); C.S. Fadley, Physica Scripta **T17**, 39 (1987); C.S. Fadley in *Synchrotron Radiation Research: Advances in Surface Science*, R.Z. Bachrach, Ed. (Plenum, New York, 1992).
- [6] A. Szoeké, in *Short Wavelength Coherent Radiation: Generation and Applications*, D.T. Attwood and J. Bokor, Eds., AIP Conference Proceedings No. 147 (AIP, New York, 1986).
- [7] J.J. Barton, Phys. Rev. Lett. **61**, 1356 (1988); J.J. Barton, J. Electron Spectrosc. **51**, 37 (1990).
- [8] G.R. Harp, D.K. Saldin, and B.P. Tonner, Phys. Rev. Lett. **65**, 1012 (1990); G.R. Harp, D.K. Saldin, and B.P. Tonner, Phys. Rev. **B42**, 9199 (1990).
- [9] S. Hardcastle, Z.-L. Han, G.R. Harp, J. Zhang, B.L. Chen, D.K. Saldin, and B.P. Tonner, Surf. Sci. **245**, L190 (1991).

- [10] G.S. Herman, S. Thevuthasan, T.T. Tran, Y.J. Kim, and C.S. Fadley, *Phys. Rev. Lett.* **68**, 650 (1992).
- [11] G.S. Herman, T.T. Tran, K. Higashiyama, and C.S. Fadley, *Phys. Rev. Lett.* **68**, 1204 (1992).
- [12] G.S. Herman and C.S. Fadley, *Phys. Rev.* **B43**, 6792 (1991); G.S. Herman, A.P. Kaduwela, T.T. Tran, Y.J. Kim, S. Lewis, and C.S. Fadley, in *The Structure of Surfaces III*, S.Y. Tong, M.A. van Hove, K. Takayanagi, and X.D. Xie, Eds. (Springer-Verlag, Berlin 1991) p. 85.
- [13] G.S. Herman, D.J. Friedman, T.T. Tran, C.S. Fadley, G. Granozzi, G.A. Rizzi, J. Osterwalder, S. Bernardi, *J. Vac. Sci. Technol.* **B9**, 1870 (1991).
- [14] S. Thevuthasan, G.S. Herman, A.P. Kaduwela, R.S. Saiki, Y.J. Kim, W. Niemczura, M. Burger, and C.S. Fadley, *Phys. Rev. Lett.* **67**, 469 (1991).

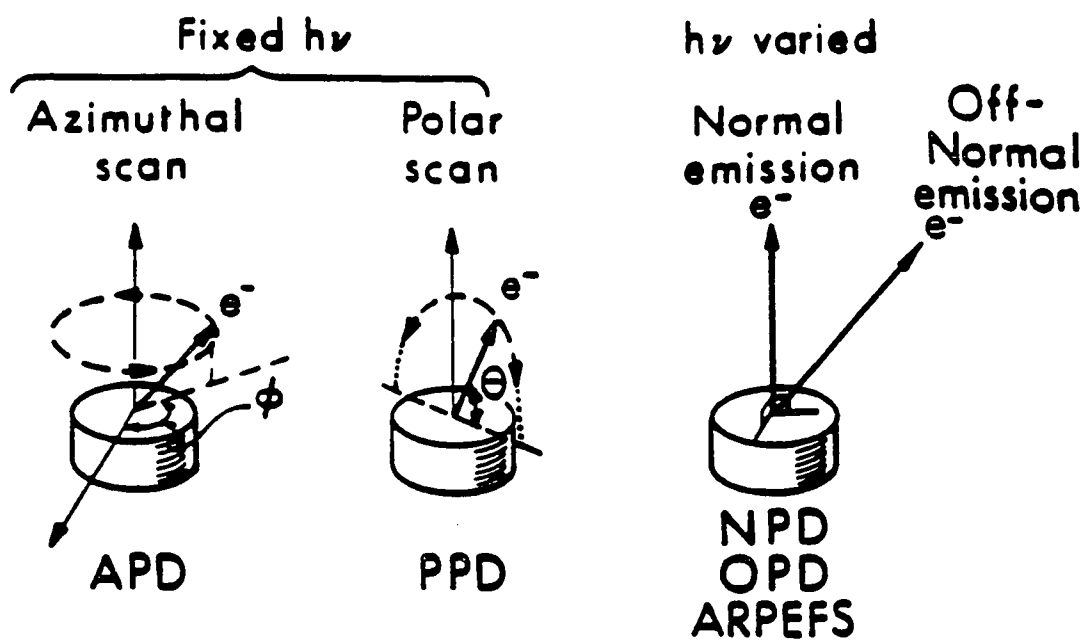


Fig. 1.1 The two basic modes of photoelectron diffraction are scanned-angle PD and scanned-energy PD. In the scanned-angle mode, the polar,  $\theta$ , and azimuthal,  $\phi$ , emission angles can be varied. In the scanned-energy mode (also known as angle-resolved photoemission fine structure or ARPEFS), the emission direction is kept fixed while the photon energy is changed. This mode thus requires synchrotron radiation.

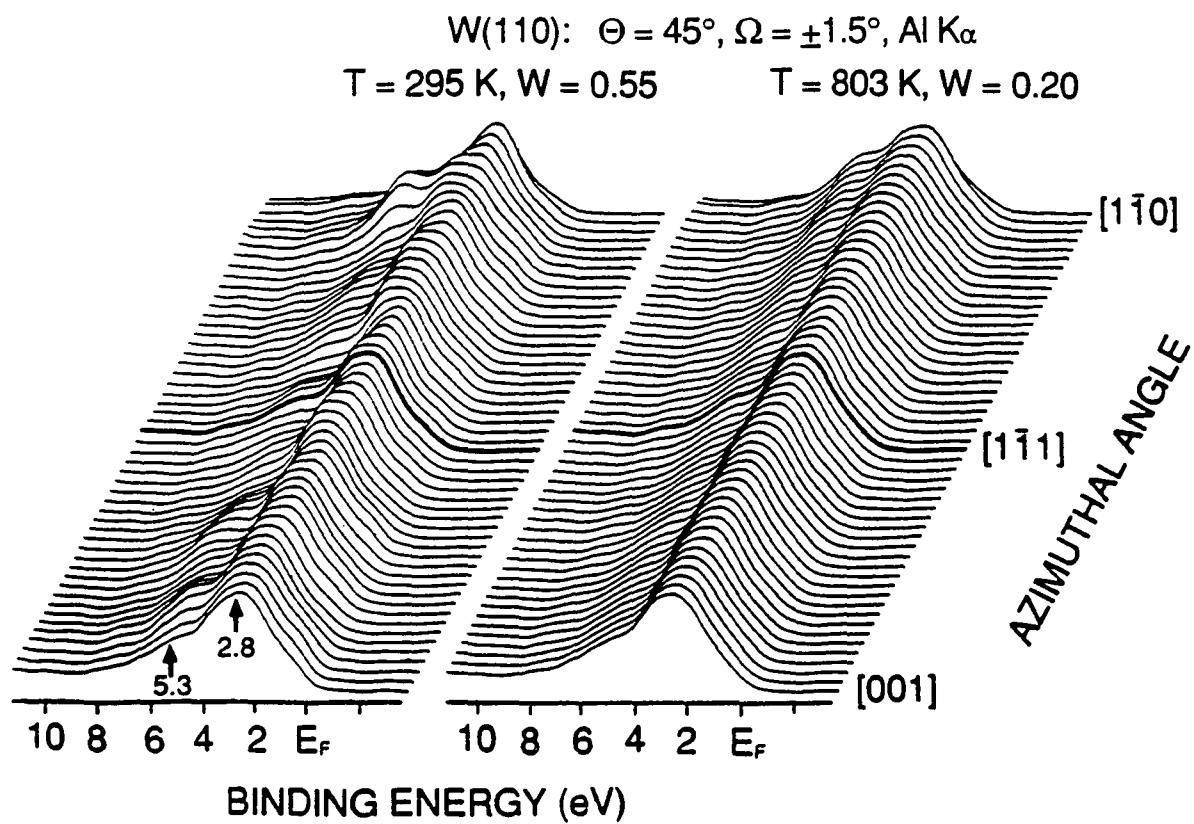


Fig. 1.2 X-ray photoelectron valence-band spectra at 295 K and 803 K from the W(110) surface at a polar angle of  $\theta=45^\circ$  taken over the azimuthal range of  $\phi=0^\circ-90^\circ$  in  $1.8^\circ$  steps.

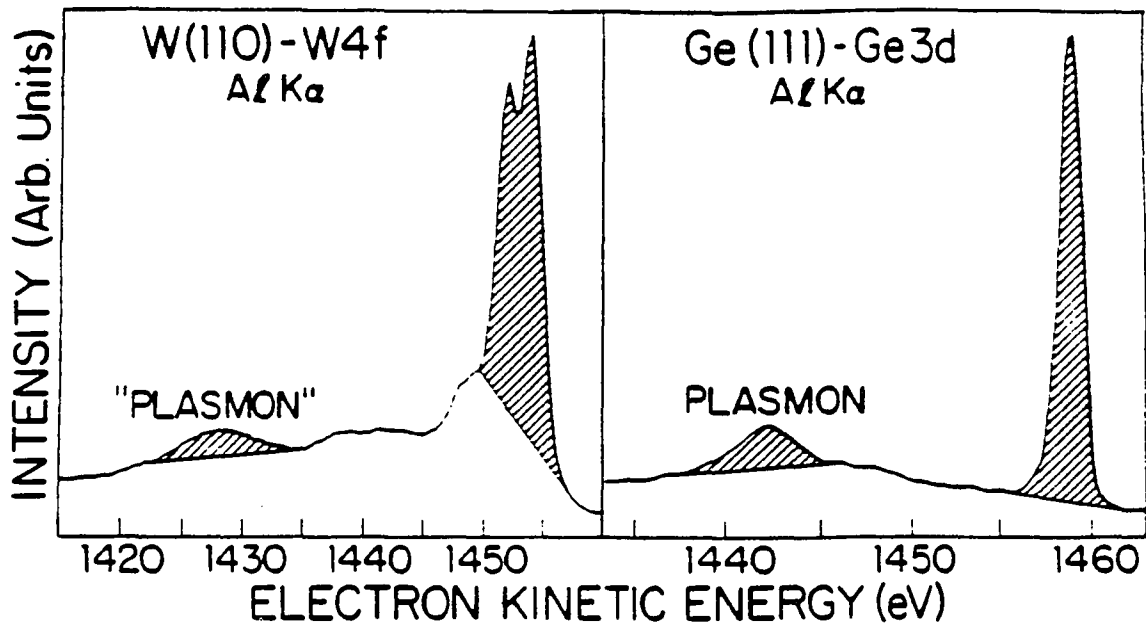


Fig. 1.3 X-ray photoelectron spectra showing elastic and inelastic peaks in W 4f emission from W(110) and Ge 3d emission from Ge(111).

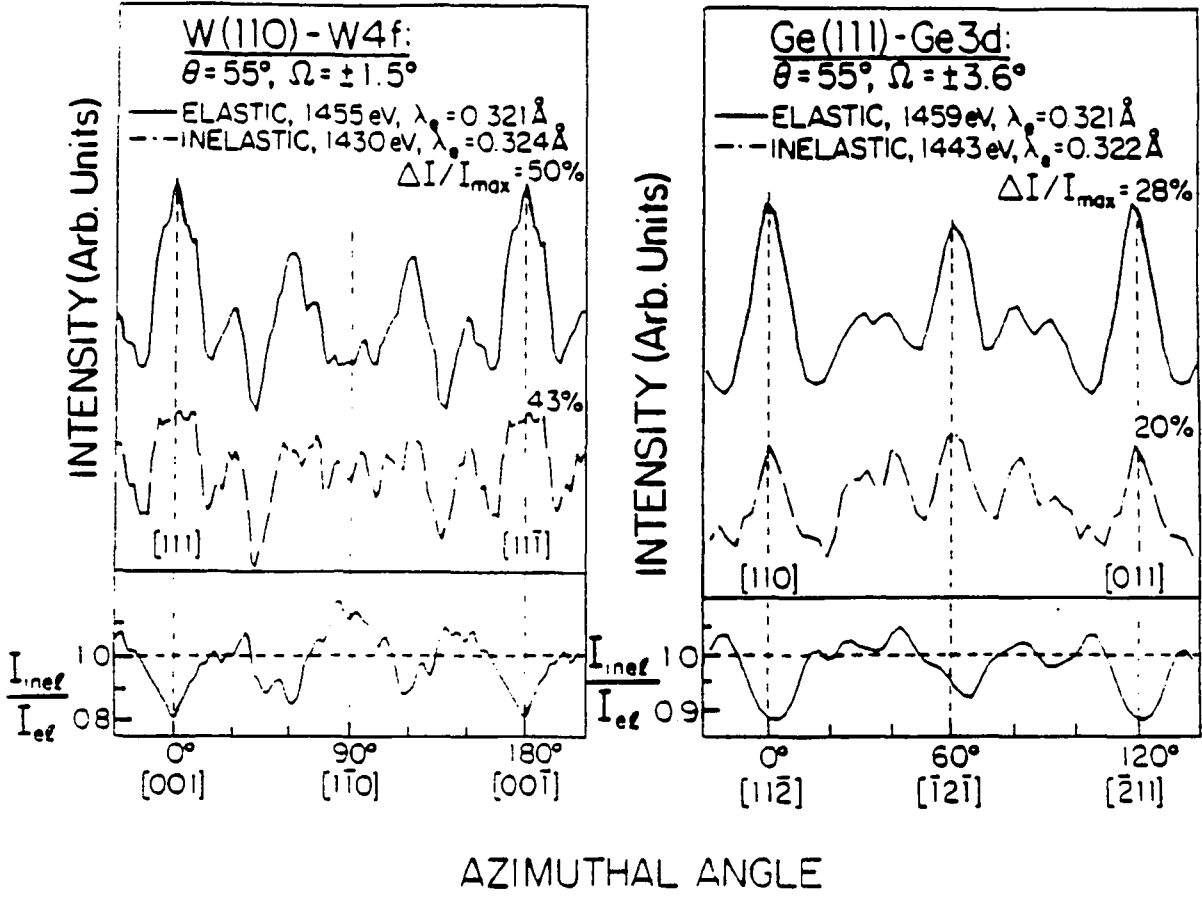


Fig. 1.4 Azimuthal scans of the elastic intensity and its associated plasmon loss intensity, together with the normalized ratio of the plasmon loss intensity to the elastic intensity for W 4f and Ge 3d, both at the polar angle of  $\theta=55^\circ$ .

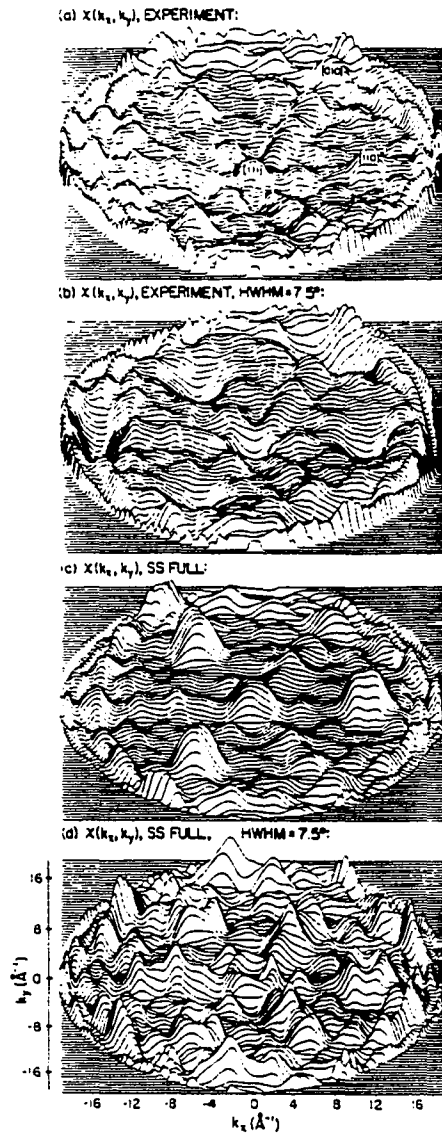


Fig. 1.5 Projection of the  $\chi(\vec{k})$  hologram for Si 2p emission from Si(111) at 1388 eV onto the  $k_x$ - $k_y$  plane; hologram opening angle  $\alpha=172^\circ$ . (a) Experiment, with several low-index directions labeled. (b) Experiment, with Gaussian removal of forward scattering intensities along low-index directions marked in (a). (c) As (a), but for full scattering strength single scattering (SS) theory. (d) As (b), but for full scattering strength SS.

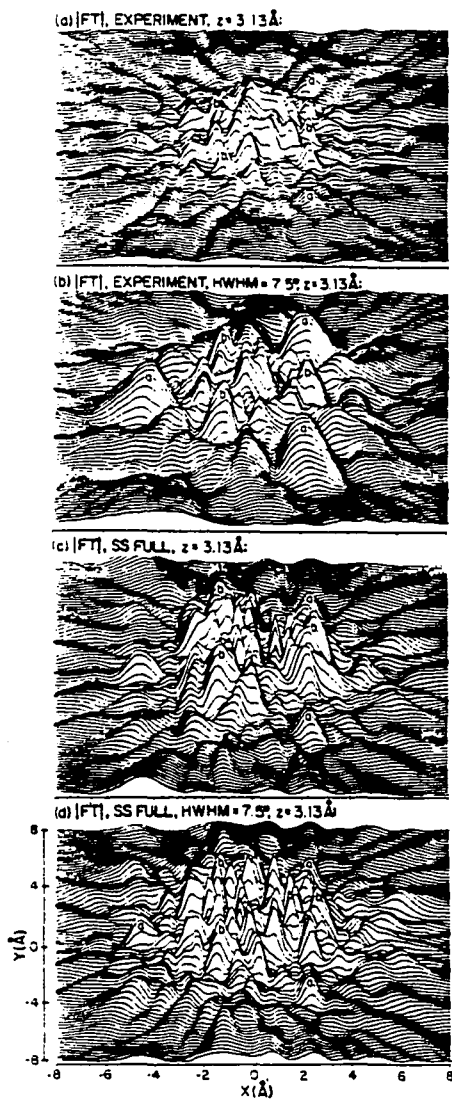


Fig. 1.6 Fourier transform contour plots of the  $\chi(\vec{k})$  data in Fig. 1.5 in the horizontal  $z=3.13 \text{ \AA}$  plane. (a) Experiment. (b) Experiment, with Gaussian removal of forward scattering intensities along low-index directions. (c) As (a), but for full scattering strength SS. (d) As (b), but for full scattering strength SS.

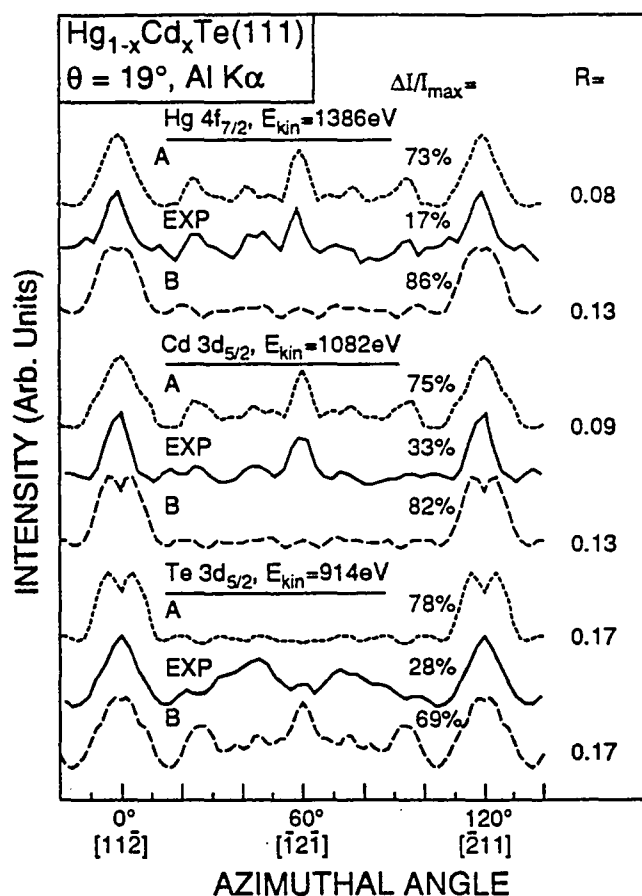


Fig. 1.7 Comparison between experimental scans taken at  $\theta=19^\circ$  and single scattering (SS) theoretical curves obtained for both the A (cationic) and B (anionic) surface terminations of a  $\text{Hg}_{1-x}\text{Cd}_x\text{Te}(111)$  sample. The overall anisotropy as judged from  $(I_{\max}-I_{\min})/I_{\max}$  in % is also indicated for each curve. R factor values are also included to indicate the goodness of fit. It is typical in such analyses for theory to predict a significantly higher anisotropy than is observed, with reasons being the presence of surface disorder, the presence of an amorphous layer of surface impurities, and/or multiple scattering effects such as defocussing along low-index directions.

## Chapter 2

### Experimental Methods

The initial experimental work on the Ge(111) high-temperature surface phase transition was performed on a Hewlett-Packard (HP) 5950A x-ray photoelectron spectrometer located at the University of Hawaii. This spectrometer is equipped with a monochromatized Al  $K\alpha$  radiation source ( $h\nu=1486.6$  eV), a full hemispherical electrostatic analyzer, a multichannel detector based on a chevron channel-plate multiplier with a Surface Science Laboratories Model 239 resistive-strip anode for multichannel position sensing, and a custom-designed manipulator. This manipulator is equipped with a two-axis goniometer allowing automated rotation of both the polar ( $\theta$ ) and azimuthal ( $\phi$ ) angles of emission, and also serves as the sample transfer mechanism between the preparation chamber and the main analysis chamber. This spectrometer and its custom modifications are discussed in detail elsewhere [1]. The preparation chamber includes low energy electron diffraction (LEED), in situ sample cleaning by ion sputtering, and sample temperature measuring capabilities. Ultra-high vacuum (UHV) conditions, typically in the  $10^{-10}$  torr range for the preparation chamber and  $10^{-11}$  torr range for the main x-ray photoelectron (XPS) chamber, were maintained with ion and titanium sublimation pumps. Additional details on the cleaning and preparation of specific surfaces for study appear in later chapters. The first phase of our study of the Ge(111) surface phase transition was performed on this HP system, and it was these data that first showed we could reliably observe the transition using photoelectron diffraction. However, the monochromatized source on this spectrometer leads to intensities that are about 4.3x lower than in a second Vacuum Generators (VG) ESCALAB5 spectrometer system to be described below. Thus, the project was shifted for its completion to the second system, and it is these data that are

reported exclusively in Chapter 4. For reference, Fig. 2.1 gives an example of data on the Ge(111) phase transition as obtained from the HP spectrometer [2], and this can be compared directly to similar data in Fig. 2.2 and chapter 4, as obtained from the VG spectrometer. The more accurate measurements in Fig. 2.2 show the transition shifted to higher temperatures by ~150 K; the reason for this discrepancy is most likely due to the less accurate temperature measurements taken in the preparation chamber followed by the transfer of the sample to the main analysis chamber of the HP system compared to the set-up on the VG which allows simultaneous temperature measurements and data acquisition.

All experimental data in chapter 4 were acquired with the VG ESCALAB5 spectrometer (also at the University of Hawaii). Most aspects of the VG spectrometer such as the specimen manipulator, the x-ray source, the detector, and the analyzer are similar to those found in the HP spectrometer. It is also equipped with a Surface Science Laboratories Model 3390 multichannel detector [3]. However, the radiation source here is a standard (i.e. non-monochromatized) Al K $\alpha$  x-ray tube (again at  $h\nu=1486.6$  eV) that is much more intense than that in the HP system. In addition to titanium sublimation pumps, an oil-diffusion pump is used to maintain UHV conditions. An important difference is the higher angular resolution capability afforded by a set of fixed length-to-diameter tube arrays mounted on a rotatable plate which allows several different angular acceptance cones to be brought into use [4]. The possible configurations are tube array assemblies of  $\pm 1.5^\circ$  and  $\pm 3.0^\circ$  angular acceptance and open apertures of  $\pm 3.0^\circ$  and  $\pm 6.0^\circ$ . As a comparison, the highest angular resolution data, taken with the  $\pm 1.5^\circ$  angular acceptance, necessitate a 56x reduction in intensity compared to  $\pm 6.0^\circ$  operation and lead to a corresponding increase in data acquisition time. Nonetheless, juxtaposing the results in Figs. 2.1 and 2.2, results measured with the HP and VG spectrometers, respectively, it is clear that the VG spectrometer provides significantly higher intensity and therefore yields data with less

scatter than the HP for comparable data collecting time. However, except for the shift in temperature, the two curves are fully in agreement as to the overall shape of the intensity loss occurring through the transition.

Finally, the results discussed in chapter 5, on spin-polarized photoelectron diffraction (SPPD) studies of MnO and Fe were obtained with an angle resolved  $127^\circ$  cylindrical electron analyzer with an angular resolution of  $1^\circ$  or better and with radiation from a  $15^\circ$  toroidal grating monochromator at the SA73 beamline of the Super-ACO storage ring at LURE, Orsay, France [5]. This system also was equipped with LEED and Auger electron spectroscopy (AES) allowing the verification of specimen surface quality. This work thus involved tuneable-energy synchrotron radiation as the excitation source. These experiments were carried out in two separate runs that required the author's travel to France, the preparation of special samples and their mounting in the spectrometer system there, and the carrying out of measurements on the synchrotron radiation beamline. These runs were both of about two weeks duration, and in both cases, unexpected and unavoidable problems with the electron storage ring and/or the quality of the sample surfaces significantly reduced the amount of useful data acquisition time. Thus, what is reported in Chapter 5 cannot be considered as a completed study, but rather a significant step toward the planning of the next phases of this research to be carried on by others. Photon energies ranging from 150 eV to 190 eV were used in different portions of the experiment. Preliminary SPPD data on Gd, on the other hand, were measured with the VG spectrometer described above.

## References

- [1] R.J. Baird and C.S. Fadley, *J. Electron Spectrosc. Relat. Phenom.* **11**, 39 (1977);  
C.S. Fadley, *Prog. in Surf. Sci.* **16**, 275 (1984).
- [2] T.T. Tran, D.J. Friedman, Y.J. Kim, G.A. Rizzi, and C.S. Fadley, in *The Structure of Surfaces III*, S.Y. Tong, M.A. Van Hove, K. Takayanagi, and X.D. Xie, Eds. ,  
(Springer-Verlag, Berlin, 1991).
- [3] J. Osterwalder, M. Sagurton, P.J. Orders, C.S. Fadley, B.D. Hermsmeier, and D.J. Friedman, *J. Electron Spectrosc. Relat. Phenom.* **48**, 55 (1989).
- [4] R.C. White, C.S. Fadley, and R. Trehan, *J. Electron Spectrosc. Relat. Phenom.* **41**,  
95 (1986).
- [5] C. Guillot, C. Thuault, Y. Jugnet, D. Chauveau, R. Hoogewijs, J. Lecante, M.D. Tran, G. Treglia, M.C. Desjonqueres, and D. Spanjaard, *J. Phys. C: Solid State Phys.* **15**, 4023 (1982); C. Guillot, M.C. Desjonqueres, D. Chauveau, G. Treglia, J. Lecante, D. Spanjaard, and M.D. Tran, *Solid State Commun.* **50**, 393 (1984).

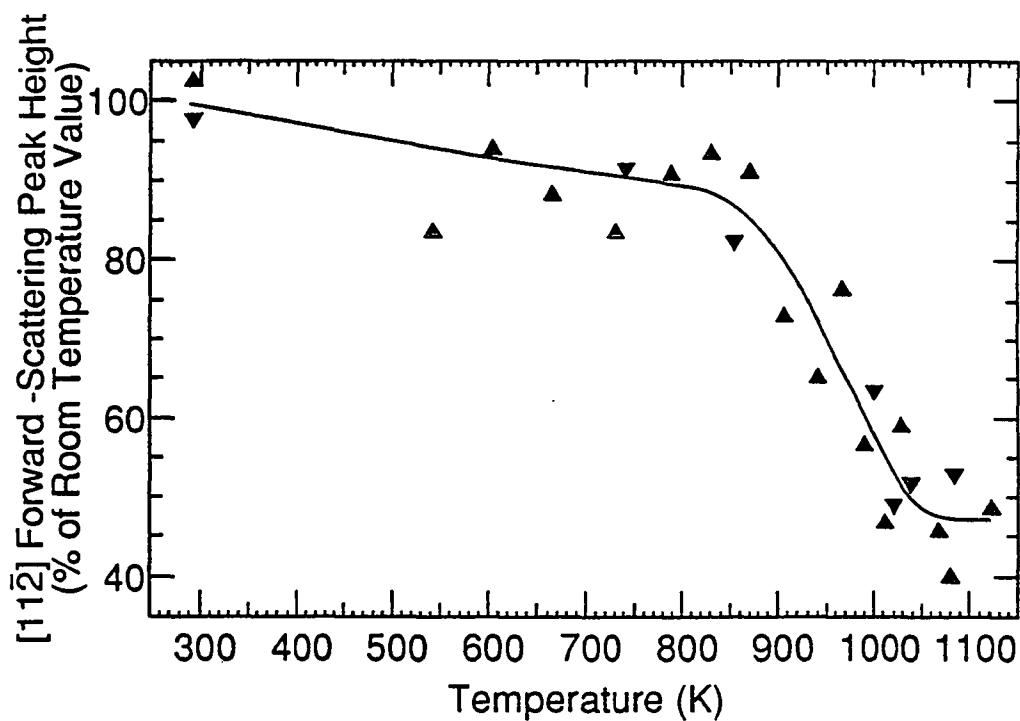


Fig. 2.1 Data for Ge 3d emission as obtained from the Hewlett-Packard 5950A spectrometer showing the detailed temperature dependence of the height of the nearest-neighbor forward scattering peak along  $\theta=19^\circ$ ,  $\phi=0^\circ$ . Upright triangles represent increasing temperature and inverted triangles decreasing temperature. Angular resolution is  $\sim\pm 3.6^\circ$ .

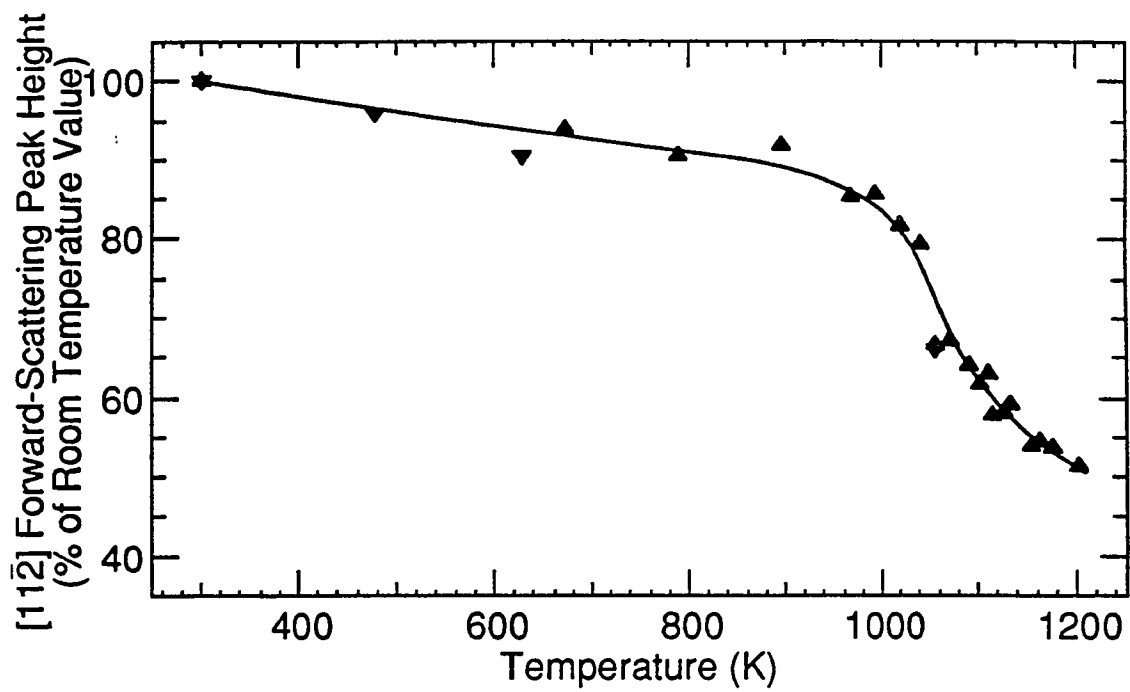


Fig. 2.2 Data similar to those shown in Fig. 2.1 but for Ge 3p emission and as obtained from the Vacuum Generators ESCALAB5 spectrometer. Angular resolution is  $\pm 3.0^\circ$  (single aperture).

## Chapter 3

### Theoretical Methods

In photoelectron diffraction (PD) the interference and scattering effects of photoelectrons emitted from core levels produce modulations in the photocurrent when either the emission angle or kinetic energy of the photoelectron is varied above a single crystal surface. In order to quantitatively analyze the experimental data obtained in PD experiments, computer simulations are performed. A number of different approximations can be made in these simulations and cluster-based techniques have proven to be very useful [1,2]. It has been found that at higher kinetic energies ( $E_{\text{kin}} > 500$  eV) single scattering cluster (SSC) calculations very well describe the experimental data, but in certain cases, such as along low-index directions and/or at lower  $E_{\text{kin}}$ , multiple scattering (MS) effects need to be considered [2]. In this chapter, we will discuss two different methods, the first, a plane wave approximation which includes only single scattering (SS), and the second, a spherical wave scattering matrix formalism of Rehr and Albers [3] which can be easily applied to both single and multiple scattering limits.

The first step is to model the experimental intensity of the interference structure between the emitted electron waves, which can be described by the following equation,

$$I(\vec{k}) \propto \left| \phi_0(\vec{k}) + \sum_j \phi_j(\vec{k}) \right|^2, \quad (3.1)$$

where  $I(\vec{k})$  is the measured intensity of the photocurrent,  $\phi_0(\vec{k})$  is the final state wave for the photoelectron without scattering (often called the direct wave),  $\phi_j(\vec{k})$  is the final state wave for the photoelectron after scattering with the  $j^{\text{th}}$  atom (often called the scattered wave), and  $\vec{k}$  is the wave vector of the photoelectron so that the direction of the

photoelectron from the emitter towards the detector is  $\hat{k} = \vec{k} / |\vec{k}|$ . The  $\phi_j(\vec{k})$ 's can have contributions from both single and multiple scattering events, where  $j$  is the scatterer index in a SS picture and the path index if MS is included. The oscillations in PD can then result from the interference between the direct wave  $\phi_0(\vec{k})$  and the scattered waves  $\phi_j(\vec{k})$ , as well as a weaker interference of the scattered waves with one another. In Fig. 3.1 the interference pattern for the simplest two-atom case, including only the emitter and one scatterer, is illustrated. The modulations in intensity are directly related to the orientation of the bond between emitter and scatterer (forward or 0<sup>th</sup> order peak) or to the distance between the emitter and the scatterer (1<sup>st</sup>, 2<sup>nd</sup>, 3<sup>rd</sup>, ... order peaks). Structural parameters such as bond distances and bond angles come into the oscillations as phase shifts due to path length differences between the various waves. These quantities and extra phase shifts due to electron-atom scattering must be included in Eq. 3.1 to adequately describe experimental PD data.

For simplicity, the SSC approximation at the plane wave limit (the first model used to describe such data in Refs. 1 and 2) will be the first method presented. In this model, the scattered wave can be written as  $\phi_j(\vec{k}) = f_j(\theta_j) \exp\left(\frac{ikr}{r}\right)$  with the complex electron-atom plane wave scattering factor  $f_j(\theta_j)$ , with magnitude  $|f_j(\theta_j)|$  and phase  $\Psi_j(\theta_j)$ , being calculated from,

$$f_j(\theta_j) = (2ik)^{-1} \sum_{l=0}^{l_{\max}} (2l+1) (\exp\{2i\delta_l^j\} - 1) P_l(\cos(\theta_j)), \quad (3.2)$$

where  $l$  is the angular momentum of each partial wave,  $\delta_l^j$  is the phase shift of the  $l^{\text{th}}$  partial wave for the  $j^{\text{th}}$  scatterer,  $P_l$  is the Legendre polynomial of order  $l$ , and  $\theta_j$  is the scattering angle. The limit on the sum is  $l_{\max} \approx kR_{\text{MT}}$  with  $R_{\text{MT}}$  being the effective or muffin-tin radius of the scattering potential. In Fig. 3.2 the amplitudes of some plane wave scattering

factors are illustrated for a number of different energies [4]. At higher  $E_{\text{kin}}$ , it is important to note that the maximum in intensity occurs when  $\theta_j=0^\circ$  which is often referred to as the forward scattering direction. In Fig. 3.3 the scattering phase shifts are illustrated for the same set of energies as for Fig. 3.2. For higher energies, the values of  $\Psi_j(\theta_j)$  are found to be near zero in the forward direction (the case illustrated in Fig. 3.1), but they can become quite large upon increasing  $\theta_j$ . When Eqs. 3.1 and 3.2 are combined, and when it is further assumed that the initial state of the photoelectron before scattering is a p-wave, the final expression is [2,4,5],

$$I(\vec{k}) \propto \left| \hat{\epsilon} \cdot \hat{k} \exp\{-L_0/2\lambda_e\} + \sum_j \hat{\epsilon} \cdot \hat{R}_j \frac{|f_j(\theta_j)|}{R_j} W_j \exp\{-L_j/2\lambda_e\} \exp\{-ikR_j(1-\cos\theta_j) + \Psi_j(\theta_j)\} \right|^2, \quad (3.3)$$

where  $\hat{\epsilon}$  is the direction of the radiation polarization vector,  $L_0$  is the distance from the emitter to the surface,  $\lambda_e$  is the inelastic mean free path of the electron in the solid,  $\vec{R}_j$  is the vector pointing from the emitter to the  $j^{\text{th}}$  scattering atom and  $R_j$  is its magnitude,  $\hat{R}_j = \vec{R}_j/R_j$ ,  $W_j$  is the Debye-Waller factor,  $L_j$  is the total path length from the emitter to the scatterer to the surface, and  $k$  is the magnitude of the photoelectron wave vector.

The various elements of this model can be described as follows. The direct wave going to the detector is proportional to  $\hat{\epsilon} \cdot \hat{k}$ , and the scattered wave amplitude is proportional to  $\hat{\epsilon} \cdot \hat{R}_j |f_j(\theta_j)|/R_j$ . Both waves are attenuated by an inelastic loss exponential depending upon the distances  $L_0$  and  $L_j$  over which the electrons travel through the sample, as appropriate to the direct and scattered waves respectively. The quantity  $R_j(1-\cos\theta_j)$  is the path length difference between the direct wave and the  $j^{\text{th}}$  scattered wave, and  $kR_j(1-\cos\theta_j)$  in Eq. 3.3 thus represents the geometric phase shift associated with scattering. This

arises due to the different distances traveled by  $\phi_0(\vec{k})$  and  $\phi_j(\vec{k})$ . Thus the total differences between the phases of the direct and scattered waves are  $kR_j(1-\cos\theta_j) + \Psi_j(\theta_j)$ . The Debye-Waller factor allows in an approximate way for the attenuation of the diffraction effects due to atomic vibrational motion and the resultant averaging over phases.

Although the plane wave SSC formalism has a simple interpretation, significant deviations can exist when compared to more accurate spherical wave SSC calculations. The largest difference is an overestimation of the forward scattering strength at the plane wave limit [6]. Thus in the following paragraphs, the scattering matrix formalism of Rehr and Albers will be described. For this formalism the photocurrent in the absence of inelastic and vibrational effects can be written as,

$$I(\vec{k}) \propto \frac{d\sigma}{d\Omega}(\vec{k}) \propto \left| \sum_{L,N} G_{00,L}^{(N)}(k\vec{R}_\infty) m_{L,c}(\hat{\epsilon}) \exp(i\delta_L^c) \right|^2 \quad (3.4)$$

where  $I(\vec{k})$  is the intensity at the detector with wave vector  $\vec{k}$ , the core photoelectric cross section for emission from a given sublevel  $n_i l_i m_i$  is given by  $\frac{d\sigma}{d\Omega}(\vec{k})$ ,  $G_{00,L}^{(N)}$  is the exact scattering Green's function for an N-fold scattering path (for single scattering N=2) from the emitter at  $\vec{R}_0$  via scatterers at  $\vec{R}_1, \vec{R}_2, \dots$ , to  $\vec{R}_N$ , to the detector at  $\infty$ ,  $L=(l,m)$  is the angular momentum of the electron for a given final state, and  $m_{L,c}(\hat{\epsilon})$  and  $\delta_L^c$  are the amplitude and phase of the core-to-continuum matrix element.

For single scattering Eq. 3.4 can be expanded to,

$$I(\vec{k}) \propto \left| \sum_L \left[ G_{00,L}^{(1)}(k\vec{R}_\infty) + G_{00,L}^{(2)}(k\vec{R}_j, k\vec{R}_\infty) \right] m_{L,c}(\hat{\epsilon}) \exp(i\delta_L^c) \right|^2, \quad (3.5)$$

where the emitter is at the origin,  $G_{00,L}^{(1)}(k\vec{R}_\infty)$  is the direct wave term, and  $G_{00,L}^{(2)}(k\vec{R}_j, k\vec{R}_\infty)$  is the scattered wave term which is summed over all single scattering

paths. To further apply this formalism to PD, the z-axis is first taken for simplicity to be along the direction of the light polarization, and a given bond direction (corresponding to  $\vec{\rho} = k\vec{R}_j$ , a "bond vector", in units of  $2\pi$ ) is then rotated onto the z-axis to further simplify the calculation. In part, this only allows transitions satisfying  $m_i = m_f$ . The direct wave can then be written as,

$$G_{00,L}^{(1)}(k\vec{R}_\infty) = [\exp\{i\rho_\infty\}/\rho_\infty] 4\pi^{1/2} Y_{lfm_i}(\theta_k, \phi_k), \quad (3.6)$$

where  $\rho_\infty = |k\vec{R}_\infty|$ ,  $Y_{lfm_i}(\theta_k, \phi_k)$  is a spherical harmonic, and  $(\theta_k, \phi_k)$  are the angles of  $\vec{k}$  measured with respect to  $\hat{E}$  as the z axis. Likewise, the single scattering term can be written as,

$$G_{00,L}^{(2)}(k\vec{R}_j, k\vec{R}_\infty) = \sum_{j,L_j} G_{00,L_j}(\vec{\rho}_\infty) t_j(\vec{R}_j) G_{L_j,L}(\vec{\rho}_j), \quad (3.7)$$

where now  $\vec{\rho}_\infty = k(\vec{R}_\infty - \vec{R}_j)$ ,  $\vec{\rho}_j = k\vec{R}_j$ ,  $G_{00,L_j}(\vec{\rho}_\infty)$  and  $G_{L_j,L}(\vec{\rho}_j)$  are matrix elements of the free-electron propagator in both angular momentum and site basis, and  $t_j = \exp\{i\delta_j\} \sin\delta_j$  is a diagonal element of the t-matrix for scattering and  $\delta_j$  refers to the conventional scattering phase shifts (as used in the plane-wave approximation of Eq. 3.2).

The resulting matrix elements can then be expanded to,

$$G_{00,L_j}(\vec{\rho}_\infty) = [\exp\{i\rho_\infty\}/\rho_\infty] \sum_{\mu'} R_{0\mu'}^0(\hat{\rho}_\infty^{-1}) \left[ \sum_{\nu'=0}^{[0, l_j - |\mu'|]} \tilde{\gamma}_{\mu'\nu'}^0(\rho_\infty) \gamma_{\mu'\nu'}^{l_j}(\rho_\infty) \right] \\ \times \left[ R_{\mu'm_j}^{l_j}(\hat{\rho}_\infty) \right] \quad (3.8)$$

and,

$$G_{L,j,L}(\vec{\rho}_j) = [\exp\{i\rho_j\}/\rho_j] \sum_{\mu''} R_{m_j \mu''}^{l_j}(\hat{\rho}_j^{-1}) \left[ \sum_{\nu''=0}^{[0, l_j - |\mu''|]} \tilde{\gamma}_{\mu'' \nu''}^{l_j}(\rho_j) \gamma_{\mu'' \nu''}^{l_f}(\rho_j) \right] \\ \times \left[ R_{\mu'' m_i}^{l_f}(\hat{\rho}_j) \right] \quad (3.9)$$

where  $R_{\mu' m_j}^{l_j}(\hat{\rho}_\infty)$  and  $R_{\mu'' m_i}^{l_f}(\hat{\rho}_j)$  are the rotation matrices which rotate the unit vector  $\hat{\rho}$  onto the z axis,  $R_{0 \mu'}^{l_j}(\hat{\rho}_\infty)$  and  $R_{m_j \mu''}^{l_j}(\hat{\rho}_j^{-1})$  are the inverse rotation matrices which rotate the unit vector  $\hat{\rho}$  into a new direction, and only terms which satisfy the conditions  $|\mu'| < l, 0 < |\nu'| < l, |\mu' + \nu'| < l$  are included (likewise,  $\mu''$  and  $\nu''$  can be substituted into these conditions).

The separable approximation to a z-axis propagator can be written as,

$$\gamma_{\mu \nu}^l(\rho) = (-1)^\mu N_{l \mu} C_l^{(\mu + \nu)}(z) \frac{z^{\mu + \nu}}{(\mu + \nu)!} \quad (3.10)$$

and

$$\tilde{\gamma}_{\mu \nu}^l(\rho) = (2l + 1) C_l^{(\nu)}(z) \frac{z^\nu}{(N_{l \mu} \nu!)} \quad (3.11)$$

where  $N_{l \mu} = [(2l + 1)(l - \mu)! / (l + \mu)!]^{1/2}$ ,  $C_l(z)$  is the polynomial portion of the spherical Hankel function, and  $C_l^{(\nu)}(z) = \frac{\partial^\nu C_l}{\partial z^\nu}$

Finally, the total single scattering intensity for emission into a single final state can be written as,

$$I_L^{(1)}(\vec{k}) \propto \left| (-i)^{l_f} \exp(i\delta_{l_f}^c) R_{l_f}(E_{\text{kin}}) \langle l_f m_i | 10 | l_i m_i \rangle \right. \\ \left. \times \left[ G_{00,L}^{(1)}(k\vec{R}_\infty) + G_{00,L}^{(2)}(k\vec{R}_j, k\vec{R}_\infty) \right] \right|^2 \quad (3.12)$$

From Ref. 7, the Gaunt coefficients,  $\langle l_f m_i | 10 | l_i m_i \rangle$ , needed in our calculation when  $\hat{z}$  is rotated to be parallel to  $\hat{E}$  are:

$$\langle l_f m_i | 10 | l_i m_i \rangle = \langle l_f m_i | 10 | l_i m_i \rangle = (-1)^{m_i} (3/4\pi) (2l_f+1) (2l_i+1) A \quad (3.13)$$

where A is a product of two 3j symbols:

$$A = \begin{pmatrix} l_f & 1 & l_i \\ -m & 0 & m \end{pmatrix} \begin{pmatrix} l_f & 1 & l_i \\ 0 & 0 & 0 \end{pmatrix} \quad (3.14)$$

To calculate this product, we define  $l_> \equiv \max(l_f, l_i)$  and  $l_< \equiv \min(l_f, l_i)$ , and use the properties of the 3j symbols [8], to show that

$$A = (-1)^{m_i} \frac{[(l_<+m_i+1) (l_<-m_i+1)]^{1/2}}{(2l_<+3) (2l_<+1)} \quad (3.15)$$

where  $|l_f - l_i| = 1$ , or finally,

$$\langle l_f m_i | 10 | l_i m_i \rangle = \left[ \frac{[(l_<+m_i+1) (l_<-m_i+1)]^{1/2}}{(2l_<+3) (2l_<+1)} \right] \quad (3.16)$$

Photoemission for an initial state ( $l_i$ ) can occur into two separate but interfering final channels ( $l_i \pm 1$ ), where the final amplitudes with correct relative phases are summed over the various possible  $m_i$  excitations. The final intensity expression can then be expanded to:

$$\begin{aligned}
I_{n_i l_i}^{(1)}(k, \theta, \phi) \propto \sum_{m_i} \left| \sum_{l_f}^{l_i \pm 1} (-i)^{l_f} \exp(i\delta_{l_f}^c) R_{l_f}(E_{kin}) \langle l_f m_i | 10 | l_i m_i \rangle \right. \\
\times \left[ (4\pi)^{1/2} Y_{l_f m_i}(\theta, \phi) + \sum_{j=1}^M [\exp\{i\rho_j(1-\cos\theta_j)\}/\rho_j] \right. \\
\left. \left. \times \sum_{\lambda''} F_{00, \lambda''}(\vec{\rho}_\infty, \rho_j) W_{00, \lambda''}^{00, L}(\vec{\rho}_j) \right] \right|^2 \quad (3.17)
\end{aligned}$$

where

$$F_{00, \lambda''}(\vec{\rho}_\infty, \rho_j) = \sum_{l=0}^{l_{\max}} t_l(\vec{R}_j) \gamma_{00}^l(\rho_\infty) R_{0\mu''}^l(\hat{\rho}_\infty, \hat{\rho}_j^{-1}) \tilde{\gamma}_{\lambda''}^l(\rho_j) \quad (3.18)$$

and

$$W_{00, \lambda''}^{00, L}(\vec{\rho}_j) = \gamma_{\lambda''}^{l_f}(\rho_j) R_{\mu'' m_i}^{l_f}(\hat{\rho}_j) \quad (3.19)$$

Likewise, the full multiple scattering intensity with the effects of both inelastic scattering and vibrational effects can be written in a similar form as Eq. 3.17:

$$\begin{aligned}
I_{n_i l_i}^{N_{\max}}(k, \theta, \phi) \propto \sum_{m_i} \left| \sum_{l_f} (-i)^{l_f} \exp(i\delta_{l_f}^c) R_{l_f}(E_{kin}) \langle l_f m_i | 10 | l_i m_i \rangle \right. \\
\times \left[ (4\pi)^{1/2} Y_{l_f m_i}(\theta, \phi) \exp\{-i\vec{R}_{0S}/2\lambda_e\} \right. \\
+ \sum_{j_1} [\exp\{i\rho_{j_1}(1-\cos\theta_{j_1})\}/\rho_{j_1}] \exp\{-i\vec{R}_{j_1 S}/2\lambda_e\} \exp\{-i\vec{R}_{j_1}/2\lambda_e\} W_{j_1 0} \\
\left. \left. \times \sum_{\lambda_1} F_{00, \lambda_1}(\vec{\rho}_\infty, \rho_{j_1}) W_{00, \lambda_1}^{00, L}(\vec{\rho}_{j_1}) \right] \right|^2
\end{aligned}$$

$$\begin{aligned}
& \sum_{N=2}^{N_{\max}} \sum_{\{j_1\}} \left[ \prod_{k=1}^N [\exp\{i\rho_{jk}j_{k-1}(1-\cos\theta_{jk}j_{k-1})\}/\rho_{jk}j_{k-1}] \exp\{-|\vec{R}_{j_N}S|/2\lambda_e\} \right. \\
& \times \exp\{-|\vec{R}_{j_{N-1}}S|/2\lambda_e\} \dots \exp\{-|\vec{R}_{j_2}S|/2\lambda_e\} \exp\{-|\vec{R}_{j_1}S|/2\lambda_e\} \\
& \times W_{j_N j_{N-1}} \cdot W_{j_{N-1} j_{N-2}} \dots W_{j_1 j_2} W_{j_1 0} \\
& \times \sum_{\{j_1\}} F_{00, \lambda_N}(\vec{\rho}_{\infty}, \vec{\rho}_{j_N j_{N-1}}) F_{\lambda_N, \lambda_{N-1}}(\vec{\rho}_{j_N j_{N-1}}, \vec{\rho}_{j_{N-1} j_{N-2}}) \dots \\
& \left. \dots F_{\lambda_2, \lambda_1}(\vec{\rho}_{j_2 j_1}, \vec{\rho}_{j_1}) W_{00, \lambda_1}^{00, L}(\vec{\rho}_{j_1}) \right]^2 \quad (3.20)
\end{aligned}$$

where  $\vec{R}_{0S}$  is the vector from the emitter to the surface in the direction of  $\vec{k}$ ,  $\vec{R}_{jk}j_{k-1} = \vec{R}_{jk} - \vec{R}_{j_{k-1}} = \vec{\rho}_{jk}j_{k-1}/k$ ,  $\vec{R}_{j_N}S$  is the vector from atom  $j_N$  to the surface in the direction of  $\vec{k}$ , and the inelastic attenuation length of the photoelectron  $\lambda_e$  is included as an exponential decay factor  $\exp\{-L/2\lambda_e\}$ . Vibrations at the surface can be included by a Debye-Waller factor  $W_{j_1 0}$  where these values depend upon the atom and the distances between them and are defined in more detail elsewhere [9].

Most prior PD analyses have followed one or a combination of the following assumptions: initial and final angular momenta of  $l_i=0$  and  $l_f=1$  (i.e., s-level emission in the dipole approximation), or the plane wave approximation for scattering, or the neglect of  $l \neq 1$  interchannel interference for emission from non-s levels. Friedman et al. have for the first time applied the Rehr and Albers formalism described above to simulate experimental PD patterns with none of those simplifying assumptions [10]. In addition, Kaduwela et al. have shown that the theory can easily be extended to the multiple scattering regime [11].

In fact, Kaduwela et al. have performed MS on chains of Ge atoms and have observed an increase in MS effects, including a suppression of forward scattering intensity, as the number of atoms in the chain is increased [9]. Such intensity reductions, termed "defocussing", were first discussed by Tong et al. [12]. Figure 3.4 shows SS and MS calculations of Ge 3d photoelectron diffraction at 1457.0 eV from a linear Ge chain with the emitter at one end of the chain. The direction of the chain at  $\theta=19^\circ$  corresponds to one of the forward scattering directions along which the structural surface disordering study to be discussed in Chapter 4 was performed. As can be seen in Fig. 3.4, the SS peak along the forward direction has contributions from more than ten (111) monolayers, whereas the MS peak comes from about the top eight monolayers. Both defocussing intensity reduction and peak narrowing are observed as chain length increases. Figure 3.5 illustrates an interesting "saw tooth" effect in total forward scattering intensity as the chain length is increased (in both SS and MS curves). This is due to the alternating short-long-short-long nature of the interatomic separations between atoms along the chain. The enhanced intensity for even-numbered chains is due to the presence of a strong forward-focussing nearest-neighbor scatterer very close to the emitter.

Because the nature of the electron escape from Ge(111) will be an important ingredient in the analysis of our data for the phase transition in the next chapter and because MS defocussing along the chain axis is expected, additional MS calculations have been performed on chains of up to ten Ge atoms as shown in Fig. 3.6 to determine how quickly intensity converges with depth. The two chain configurations are both along forward scattering directions of  $\theta=19^\circ$  and  $55^\circ$ , with the former having atoms separated by alternating short-long-short-long-... distances of 2.45 Å-7.35 Å-... and the latter having atoms separated by the same interatomic distance of 4.00 Å. Figure 3.7 shows four panels of results from these Ge 3p MS chain calculations for the case where only a single emitter

is considered as well as the case where the intensity is summed over all emitters for a given chain length. At  $\theta=19^\circ$ , convergence of the total intensity is obtained for about  $n=6$ , or three Ge(111) double layers, whereas at  $\theta=55^\circ$ , this occurs at  $n=9$ , or nine double layers.

Finally, the last ingredients for the theoretical methods used specifically for the surface disordering study to be presented in this dissertation are the actual input parameters and the treatment of vibrational effects of the surface layer versus that of the bulk. The input file for SS calculations is shown in Table 3.1 with the parameters defined. The output, coordinate and phase shift file names as well as the the emission angles  $\theta$  and  $\phi$  are self-explanatory. Other parameters are Debye vector= $1.377 \text{ \AA}$ , Debye temperature= $374 \text{ K}$ , experimental temperature ranges from  $300$  to  $1200 \text{ K}$ , mass for correlated vibration= $12.051$ , initial-state angular momentum ( $l_i$ )= $1$  for p-emission, order= $2$ , kinetic energy for Ge  $3p=1362.8 \text{ eV}$ , inner potential ( $V_0$ )= $10 \text{ eV}$ , inelastic mean free path ( $\lambda_e$ )= $25.0 \text{ \AA}$ , back-scattering radius= $3.3 \text{ \AA}$  (so as to include about one double layer below each emitter), angular broadening= $3.0^\circ$ , angle between the photon incidence and electron detection is  $48^\circ$ , radial matrix elements  $R_{me}(l_i-1)$  and  $R_{me}(l_i+1)$  are  $0.0038$  and  $0.0110$  respectively, and finally, the phase shifts,  $\partial C(l_i-1)$  and  $\partial C(l_i+1)$ , of the radial parts of the photoelectron wave functions are  $5.294$  and  $2.529$  respectively. A hemispherical 354-atom cluster of  $14 \text{ \AA}$  in both radius and depth (which includes 10 Ge (111) monolayers) was used. The muffin-tin potentials and partial-wave phase shifts were generated with the MUF POT program by J. Pendry . Table 3.2 shows a modification of the "params" subroutine in the SSC code which allows the surface atoms to have a larger vibrational effect compared to those in the bulk. Specifically, the mean-squared amplitude of atoms in the top  $5 \text{ \AA}$  of the surface was made to be twice as large as that of atoms found deeper in the bulk.

## References

- [1] S. Kono, S.M. Goldberg, N.F.T. Hall, and C.S. Fadley, *Phys. Rev. Lett.* **41**, 1831 (1978).
- [2] S. Kono, S.M. Goldberg, N.F.T. Hall, and C.S. Fadley, *Phys. Rev.* **B22**, 6085 (1980).
- [3] J.J. Rehr and R.C. Albers, *Phys. Rev.* **B41**, 8139 (1990).
- [4] C.S. Fadley, *Prog. in Surf. Sci* **16**, 275 (1984).
- [5] C.S. Fadley, *Physica Scripta T17*, 39 (1987); C.S. Fadley in *Synchrotron Radiation Research: Advances in Surface Science*, R.Z. Bachrach Ed., (Plenum, New York, 1992).
- [6] M. Sagurton, E.L. Bullock, R. Saiki, A. Kaduwela, C.R. Brundle, C.S. Fadley, and J.J. Rehr, *Phys. Rev.* **B33**, 2207 (1986).
- [7] M. Jacob and G.C. Wick, *Ann. Physics* **7**, 425 (1959).
- [8] M. Weissbluth, *Atoms and Molecules*, (Academic Press, 1978).
- [9] A.P. Kaduwela, D.J. Friedman, and C.S. Fadley, *J. Electron Spectrosc. Relat. Phenom.* **57**, 223 (1991).
- [10] D.J. Friedman and C.S. Fadley, *J. Electron Spectrosc. Relat. Phenom.* **51**, 689 (1990).
- [11] A.P. Kaduwela, G.S. Herman, D.J. Friedman, C.S. Fadley, and J.J. Rehr, *Physica Scripta* **41**, 948 (1990).
- [12] S.Y. Tong, H.C. Poon, and D.R. Snider, *Phys. Rev.* **B32**, 2096 (1985).

Table 3.1 A sample input file for a SSC calculation

ge3p300.out	!	Output filename
1.377	!	Debye vector (Angstroms <sup>-1</sup> )
374	!	Debye temperature (K)
300	!	Experimental temperature (K)
12.051	!	Mass for correlated vibration
1 2	!	$l_i$ , order
25.0 3.3	!	$\lambda_e$ , back-scatt radius (Angstroms)
1362.8 10	!	KE-outside (eV), $V_0$
19 30 120 2	!	$\theta$ , $\phi$ initial, $\phi$ range, $\phi$ step
3.0	!	Angular broadening (degrees)
48	!	angle between hv and k (degrees)
0.0038 5.294	!	$R_{me}(l_i-1)$ , $\partial C(l_i-1)$
0.0110 2.529	!	$R_{me}(l_i+1)$ , $\partial C(l_i+1)$
gecoord.354	!	Coordinate filename
ge3p.pha	!	Phase shift filename

Table 3.2 Treatment of vibrational effects at the surface and in the bulk

C Get vibration amplitudes sig2. This part will have to be customized if  
 C doing anything fancy. Remember, in uncorrelated limit, sig2 ->> 2\*<uj2>.

```

-----
do 80 iemitr = 1, nEmitr
  do 90 jatom = 1, natoms
    rj2 = 0
    do 405 ixyz = 1,3
405   rj2=rj2 +(xiAtom(jatom,ixyz)-xiAtom(indxEmitr,ixyz))**2
    rj = sqrt(rj2)
    iatyp = atmtyp(jatom)
    iemtyp = atmtyp(indxEmitr)
    if (jatom.ne.indxEmitr) then
      sig2(jatom,iemitr)=sigatm(rj,qd,tdeb,texp,amass)
    endif
  90 continue
80 continue
  
```

C Get vibration amplitudes sig2. This part will have to be customized if  
 C doing anything fancy. Remember, in uncorrelated limit, sig2 ->> 2\*<uj2>.

```

-----
do 80 iemitr = 1, nEmitr
  do 90 jatom = 1, natoms
    rj2 = 0
    do 405 ixyz = 1,3
405   rj2=rj2 +(xiAtom(jatom,ixyz)-xiAtom(indxEmitr,ixyz))**2
    rj = sqrt(rj2)
    iatyp = atmtyp(jatom)
    iemtyp = atmtyp(indxEmitr)
    if (jatom.ne.indxEmitr) then
      if (xiatom(jatom,3).ge.-5.00) then
        vibamp = 2.0
      else
        vibamp = 1.0
      endif
      sig2(jatom,iemitr)=vibamp*sigatm(rj,qd,tdeb,texp,amass)
    endif
  90 continue
80 continue
  
```

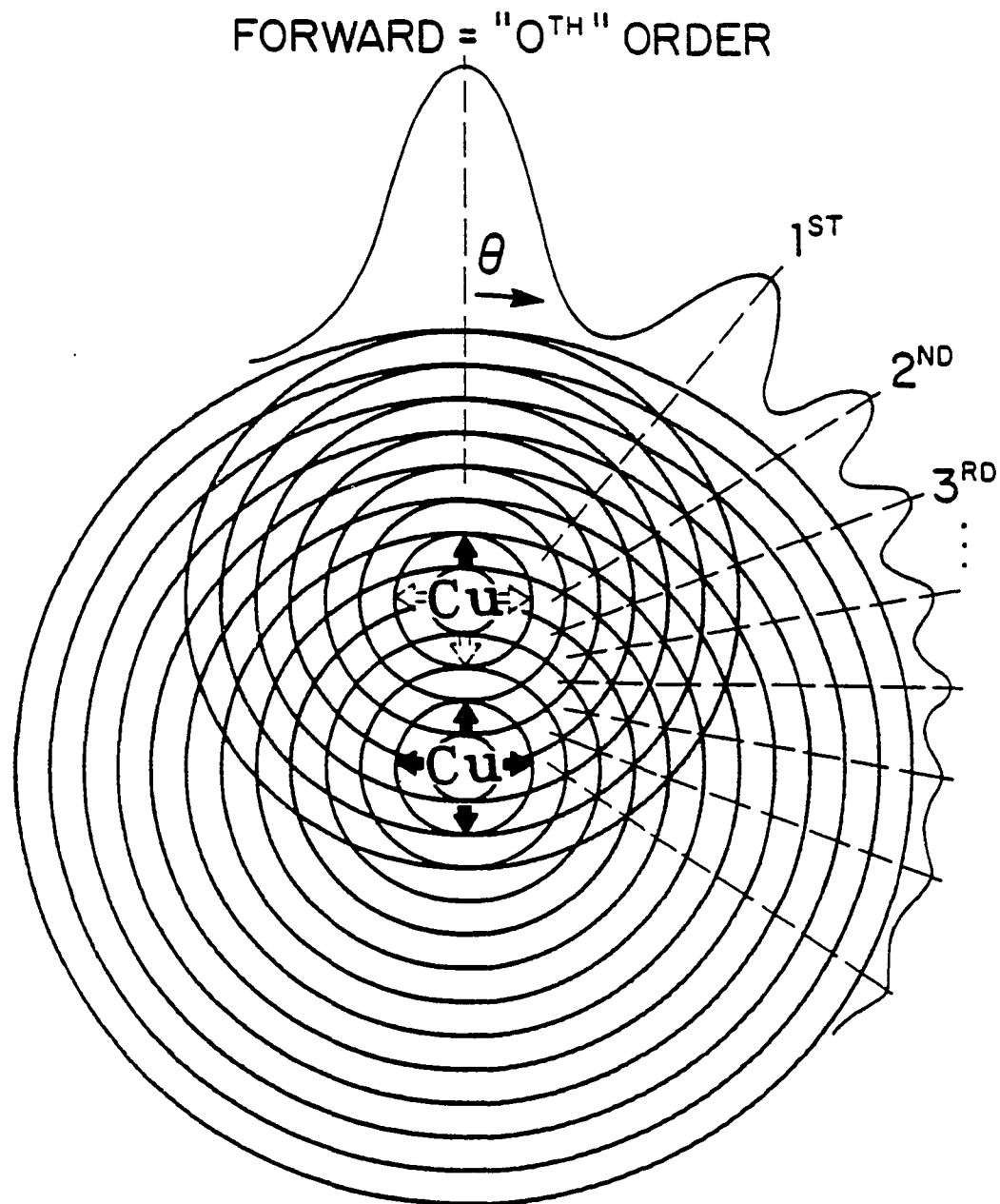


Fig. 3.1 Illustration of the origin of the diffraction features expected as a result of emission from a 2-atom chain, with the 0<sup>th</sup> order (forward scattering) peak and the higher-order peaks labeled. The scattering phase shift is, for simplicity, assumed to be zero.

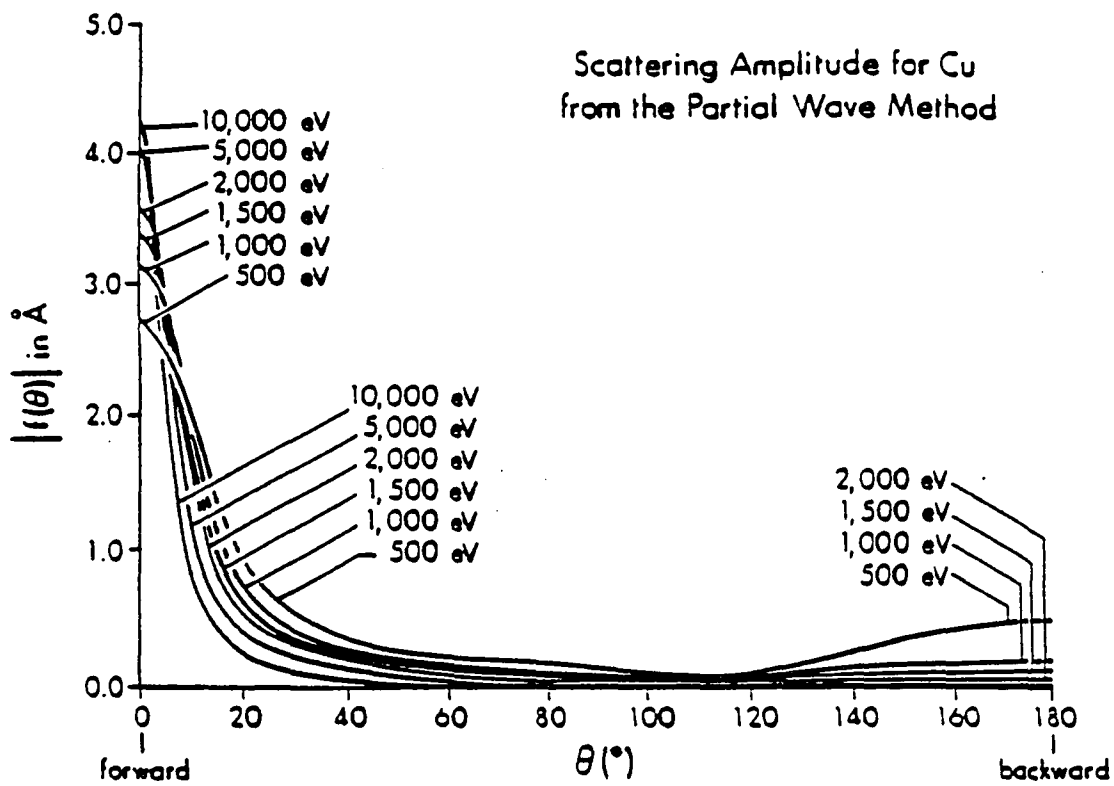


Fig. 3.2 The magnitude of the atomic scattering factor  $|f(\theta)|$  for Cu as a function of scattering angle  $\theta$  for various electron kinetic energies from 500 to 10,000 eV. Note the enhanced forward peaking as energy increases and the concomitant decrease in the importance of any backscattering.

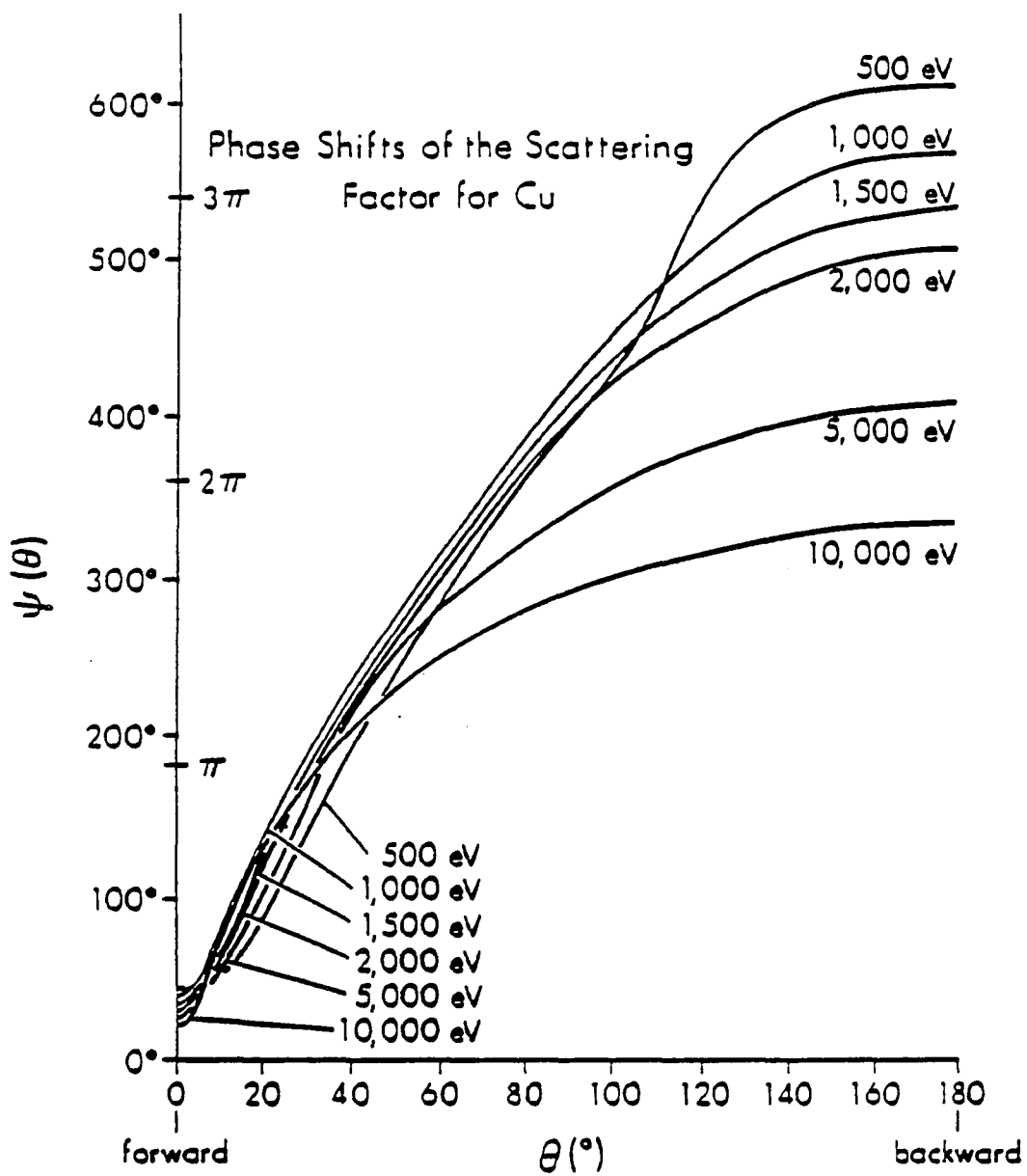


Fig. 3.3 The scattering phase shift  $\Psi(\theta)$  for Cu as a function of scattering angle  $\theta$  for various electron kinetic energies from 500 to 10,000 eV.

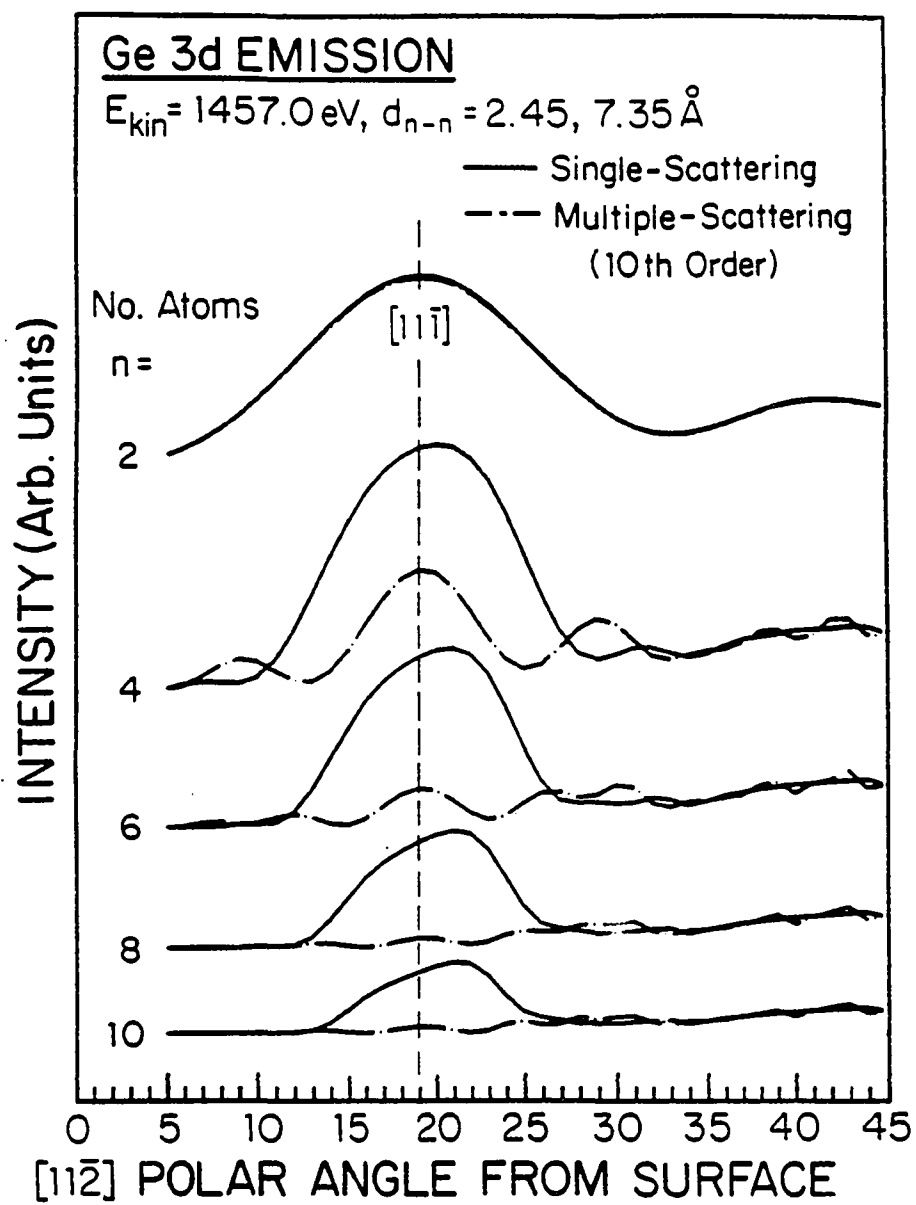


Fig. 3.4 Single and multiple scattering calculations of Ge 3d photoelectron diffraction at 1457.0 eV from linear Ge [111] chains. The emitter is at one end of the chain (from Refs. 9 and 11).

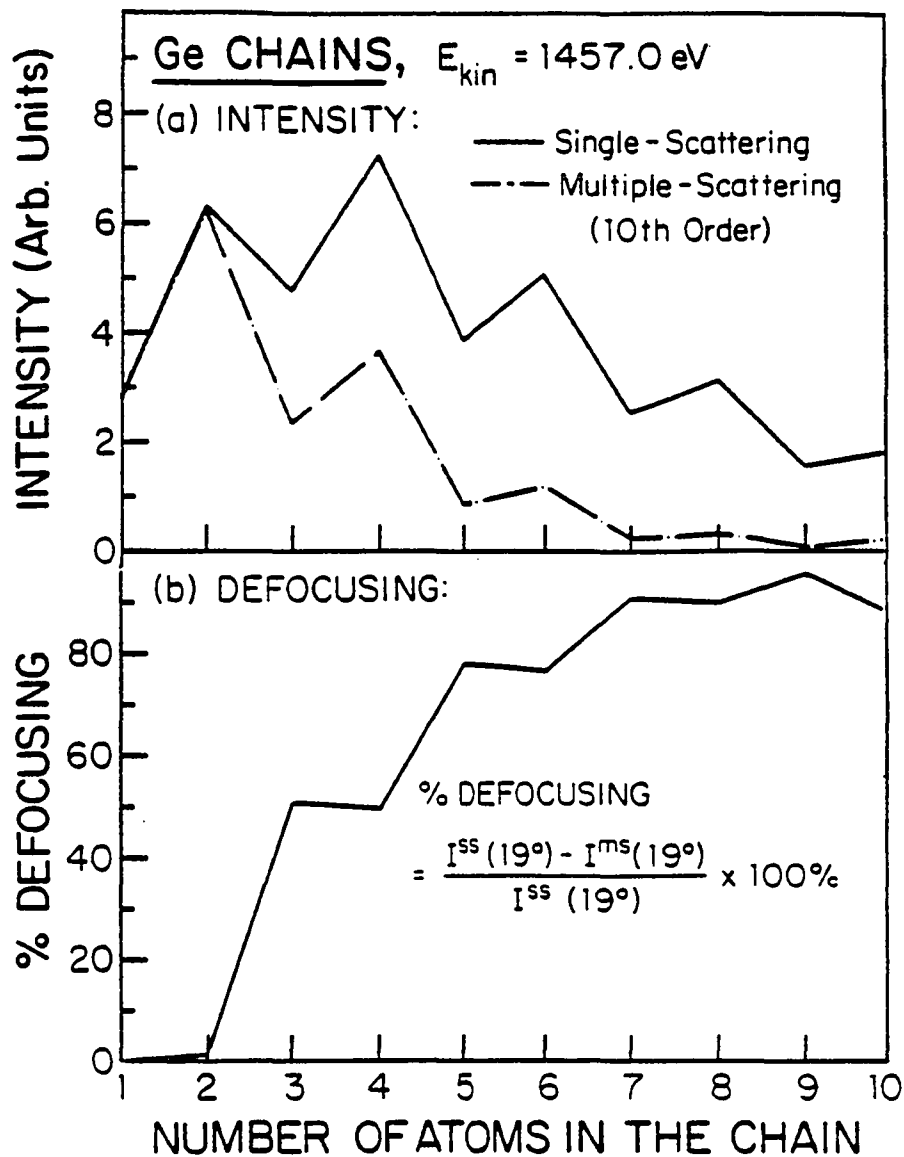


Fig. 3.5 (a) Total Ge 3d photoelectron diffraction intensity from linear Ge [111] chains at 1457.0 eV as a function of the number of atoms in the chain. (b) The percent defocussing in 3d photoelectron diffraction intensity based upon the results of (a).

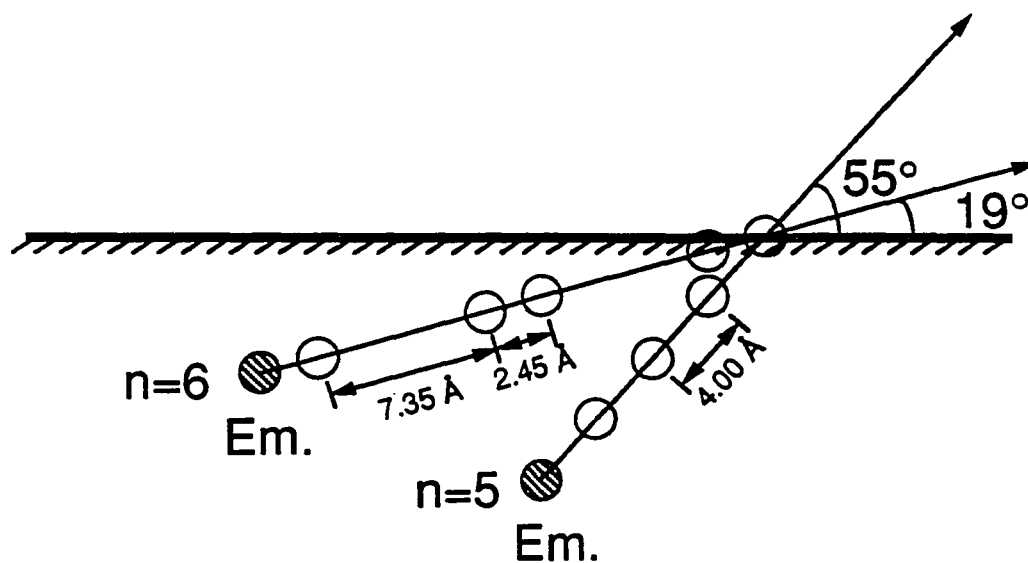


Fig. 3.6 Chain configurations used in multiple scattering calculations for the two forward scattering directions at  $\theta=19^\circ$  and  $55^\circ$ .

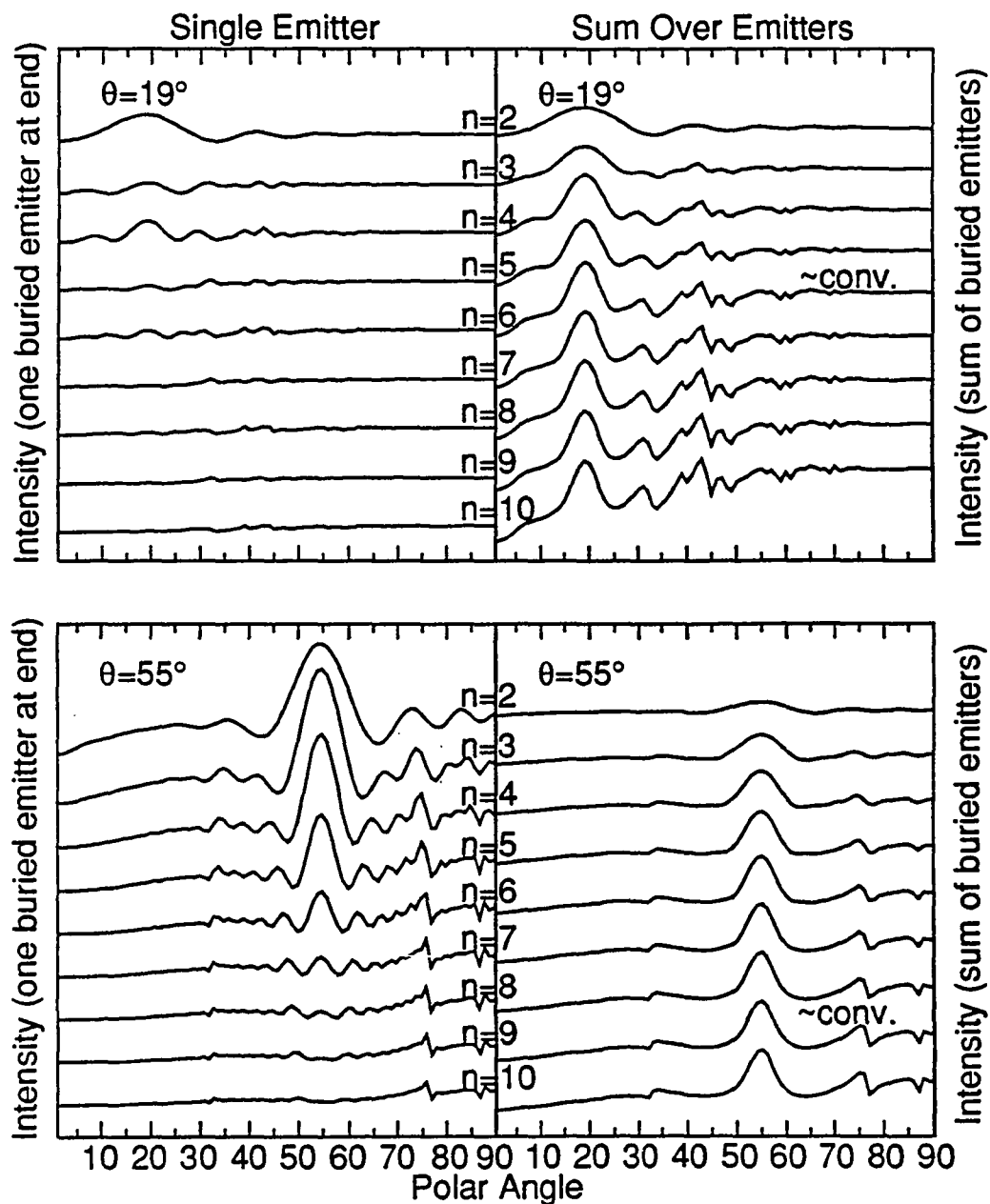


Fig. 3.7 Results from multiple scattering calculations on chains of up to ten Ge atoms at  $\theta=19^\circ$  and  $55^\circ$ . Intensities from a single emitter (left panels) as well as from the sum of all emitters (right panels) are shown, with the point at which the summed total intensity from the chain converges being indicated as "~conv.".

**Chapter 4**  
**Structural Disordering:**  
**Photoelectron Diffraction and Photoelectron Holography Study**  
**of A Ge(111) High-Temperature Surface Phase Transition**

**4.1 A Preliminary Examination**

Evidence for a reversible high-temperature surface phase transition on Ge(111) has been found previously by McRae et al. [1,2] using low-energy electron diffraction (LEED) and by Denier van der Gon et al. [3] using medium-energy ion scattering (MEIS). This transition occurs near 1060 K or about 150 K below the bulk melting point. From the LEED data, it has been proposed that this is not a surface melting or surface roughening transition, but rather a disordering transition in which small laterally-strained domains with a depth of one double layer (two Ge(111) monolayers) are produced [1,2]. However, beyond the suggestion based upon molecular mechanics modeling that there is a loss of registry between such strained domains and deeper layers [1,2], no precise structural conclusions have been possible concerning the type of disorder involved. From the MEIS data, it has been proposed that an "incomplete melting" occurs, with the formation of a thin and uniform film of positionally disordered atoms on the Ge surface [3]. The depth of disordering has been observed to remain constant up to temperatures within 25 K of the melting point and estimated to be from 1 to 1.5 Ge(111) monolayers.

We have studied this system with x-ray photoelectron diffraction (XPD) [4], a surface structure probe that is primarily sensitive to short-range order in the first 3-5 shells of neighbors around each emitter [5] and thus of comparable range to MEIS, but much shorter in range than LEED. We have examined the Ge 3p photoelectron intensity from Ge(111) as a function of both the polar and azimuthal angles of emission and temperature.

We also report results for this system obtained using a new variant of XPD, photoelectron holography [6-10], in which approximate direct imaging of atomic positions is achieved by a two-dimensional Fourier Transform (FT) of large scale data sets of intensity as a function of polar and azimuthal angles.

The XPD measurements were performed on a Vacuum Generators ESCALAB5 spectrometer modified for automated angle scanning [11]; Al K $\alpha$  radiation was used for excitation. Heating was done by a resistive button heater and temperatures were measured with an infrared pyrometer calibrated both by thermocouple and by passing through the melting point of Ge. The sample was a mirror-polished Ge wafer (n-type, Sb doped, 5-30  $\Omega$ -cm) oriented to within  $\pm 1.0^\circ$  of (111). Surface cleaning involved sputtering ( $10^{-5}$  torr Ar $^+$ , 800 eV, 850 K,  $45^\circ$  off normal incidence, 20 min.) and annealing (970 K, 30 min.). This treatment was found to give a sharp c(2x8) LEED pattern at ambient temperature, although the c(2x8) reconstruction is known to disappear at 573 K or well below the transition we are studying [1]. Surface cleanliness was monitored by XPS core-level peaks, and no detectable contaminant peaks were found before or after a full series of diffraction or holographic data.

In the diffraction experiments, the azimuthal dependence of Ge 3p core-level intensities (kinetic energy=1365 eV) was studied as a function of temperature from 300 to 1200 K. Azimuthal scans were performed at two polar angles of emission relative to the surface of  $\theta=19^\circ$  and  $55^\circ$ ; the scattering geometry is shown in Fig. 4.1.1(a) and some of the diffraction curves are shown in Figs. 4.1.1(b) and 4.1.1(c). In the holographic experiments, full intensity profiles for Ge 3p were measured at 300, 970, and 1130 K. These profiles consisted of azimuthal scans with  $1.8^\circ$  steps over  $80^\circ$  in  $\phi$ , which were then symmetry-reflected to give the full  $360^\circ$  in azimuth; the polar angle  $\theta$  was varied from grazing emission at  $\theta=10^\circ$  up to the normal at  $\theta=90^\circ$  in  $1.8^\circ$  steps.

The XPD results in Figs. 4.1.1(b) and 4.1.1(c) represent azimuthal scans taken at (b) 300, 800, and 1110 K and at (c) 300, 840, and 1130 K, and at both (b) a surface-sensitive polar angle of  $19^\circ$  containing nearest-neighbor scattering directions and (c) a more bulk-sensitive polar angle of  $55^\circ$  containing next-nearest-neighbor scattering directions [cf. Fig. 4.1.1(a)]. As temperature is increased, the diffraction peaks are damped, although they do not significantly change their fine structure. More specifically, comparing azimuthal scans in Fig. 4.1.1(b) taken at 800 and 1110 K (that is, just below and just above the expected transition point) the two main peaks at  $\phi=0^\circ$  (along the  $[11\bar{2}]$  azimuth) and  $60^\circ$  (along the  $[\bar{1}\bar{2}1]$  azimuth) are found to be much reduced in both absolute and relative intensities. The fine structure between these two peaks, from about  $\phi=14^\circ$  to  $52^\circ$ , also is reduced in intensity, with only slight changes in its form. The absolute intensity of the peak along the  $[11\bar{2}]$  azimuth decreases by  $\sim 40\%$  from 800 to 1110 K. Furthermore, the overall anisotropy, which we measure as  $(I_{\max} - I_{\min})/I_{\max} = \Delta I/I_{\max}$ , decreases significantly from 0.36 to 0.29, or by 19% over the same interval. In Fig. 4.1.1(c), analogous results are plotted for emission at  $\theta=55^\circ$ , and they lead to similar conclusions; the entire diffraction pattern is suppressed by  $\sim 30\%$  in crossing the transition, with little change in fine structure. The overall anisotropy here decreases from 0.27 for the scan taken at 840 K to 0.24 for that taken at 1130 K, or by 11%.

In Fig. 4.1.2, we show more detailed intensity and background measurements as a function of temperature. The top panel in Fig. 4.1.2(a) shows the absolute background intensity under the  $[11\bar{2}]$  forward scattering peak at  $\theta=19^\circ$  corresponding to nearest-neighbor scattering [cf. Fig. 4.1.1(b)] and the bottom panel shows the absolute  $[11\bar{2}]$  peak height, both plotted as a function of temperature. In Fig. 4.1.2(b), analogous results are plotted for emission at  $\theta=55^\circ$ . The points here were obtained with both increasing and decreasing temperature, and the form of the curve was found to be identical in both cases.

It is thus clear that an abrupt and reversible drop of 43% in the diffraction intensity for  $\theta=19^\circ$  occurs over the interval 900-1200 K. A similar drop of 31% is seen for  $\theta=55^\circ$ . By contrast, the background intensities at both  $\theta$  values exhibit only very small, and probably statistically not significant, deviations from constancy.

The drops in peak intensity at 1060 K cannot be explained by simple thermal vibrations. Debye-Waller (D-W) effects are expected to yield a smooth and linear temperature dependence in the intensity of the forward scattering peak, unlike the step-like transition observed. Model calculations of such a D-W attenuation in a simple single scattering cluster (SSC) approximation [12] are shown as the solid straight lines in Fig. 4.1.2. Thus, although such simple D-W calculations are known to underestimate the attenuation of the forward scattering peak height with temperature (an observation made previously in the analysis of XPD data from Cu(001) of Ref. 13), they at least qualitatively explain the experimental behavior below 900 K. However, the transition itself must be due to a larger-scale motion of the surface atoms, as proposed previously [1,2].

We now ask what a holographic analysis of our data can add to this description of the phase transition. Our experimental data have been first analyzed according to a procedure previously described by Barton [7]: the three-dimensional intensity distribution  $I(\vec{k})$  in the electron wave vector  $\vec{k}$  with angles of emission  $\theta$  and  $\phi$  is converted to a normalized  $\chi(\vec{k})$ , where  $\chi(\vec{k})=[I(\vec{k})-I_0(\vec{k})]/I_0(\vec{k})^{1/2}$ , with the unscattered intensity  $I_0(\vec{k})$  needed for normalization being obtained from polar-scan data for a heavily ion-bombarded surface in which no diffraction features were seen; this  $\chi(\vec{k})$  is then projected onto the  $k_x$ - $k_y$  plane with the average value of  $\chi(\vec{k})$  set to zero, and, after multiplication by a phase factor  $\exp[ik_z z]$  is Fourier transformed in  $k_x$  and  $k_y$  to yield what ideally is a cross section of the image in a plane at a distance  $z$  along [111] relative to a given emitter. Each intensity distribution or hologram occupies a cone centered along the  $z$ -[111] axis, with a full angle

given by  $\alpha=160^\circ$ . In Figs. 4.1.3(a) and 4.1.3(b), we show the experimental  $\chi(\vec{k})$  data for Ge(111) taken at temperatures of 970 and 1130 K, respectively (that is, just below and just above the disordering transition). Several low-index forward scattering directions with the most dense rows of scattering atoms along them are labeled in 4.1.3(a). Similar  $\chi(\vec{k})$  data were also measured at 300 K, but these are not shown due to length limitations; they were found to be very close to the results at 970 and 1130 K as to features and fine structure, as expected from Figs. 4.1.1(b) and 4.1.1(c).

Following a method suggested by Thevuthasan et al. [9] which has been shown to yield better subsequent FT image quality, we have multiplied the experimental  $\chi(\vec{k})$  by a Gaussian function of the form  $[1-\exp(-0.691\delta^2/\gamma^2)]$ , where  $\delta$  is the angular deviation of  $\vec{k}$  from a given low-index forward scattering axis and  $\gamma$  is a variable half-width at half maximum intensity (HWHM). This function was applied to reduce the value of  $\chi(\vec{k})$  along the highest-density  $\langle 11\bar{1} \rangle$ ,  $\langle 010 \rangle$ ,  $\langle 110 \rangle$ , and  $[111]$  directions, with an HWHM of  $7.5^\circ$  for all directions. This procedure reduces non-ideal scattering anisotropy due to forward scattering [9]. Figures. 4.1.3(c) and 4.1.3(d) show normalized images obtained after holographic inversion of the experimental data at 970 and 1130 K with Gaussian multiplication. The plane of these images at  $z=3.27\text{\AA}$  contains 6 nearest-neighbor atoms in the first double layer above a given emitter of either type 1 or type 2 in Fig. 4.1.1(a); the positions of these neighbors are labeled "a" and "b". The relative intensity of the "a" peaks in these images are 1.0, 0.63, and 0.37 for 300, 970, and 1130 K, respectively, although the FT at 300 K is not shown. Once normalized, however, all the features observed at the three different temperatures become essentially identical, in particular for the two highest temperatures. These holographic near-neighbor images above and below the transition temperature thus indicate an identical near-neighbor structure for all atoms present in ordered sites.

Our data thus overall indicate no significant perturbation of the diffraction patterns (and thus also the near-neighbor geometries) associated with Ge atoms in ordered sites upon passing through the transition. The drops in diffraction peak intensities seen in Fig. 4.1.2 can, in addition, be explained by simple inelastic attenuation in a fully disordered, liquid-like overlayer. And the constancy of the backgrounds in Fig. 4.1.2 is consistent with no loss of diffuse intensity as the overlayer disorders, since the contribution to diffuse intensity from a given scattering atom should be very nearly the same whether it is in a lattice site or in a disordered configuration.

We can finally estimate the thickness of the disordered overlayer from the inelastic attenuation it produces on a diffraction peak intensity,  $I$ , upon passing through the transition:  $I(\text{above})/I(\text{below}) = \exp[-d/(\lambda_e \sin\theta)]$ , where  $d$  is the overlayer thickness,  $\lambda_e$  is the inelastic attenuation length, and  $\theta$  is the takeoff angle as defined previously. With values  $I(\text{above})/I(\text{below})$  of approximately 0.57 for  $\theta=19^\circ$  and 0.69 for  $55^\circ$  (cf. Fig. 4.1.2), and  $\lambda_e$  of 25 Å [14], this yields  $d=4.5$  Å or 1.4 double layers for  $\theta=19^\circ$  and  $d=7.6$  Å or 2.3 double layers for  $\theta=55^\circ$ . These numbers are thus in qualitative agreement with, but significantly larger than, the approximately 1.0 double layers derived from LEED [1,2] and the 0.5-0.75 double layers derived from MEIS [3].

## References

- [1] E.G. McRae and R.A. Malic, *Phys. Rev. Lett.* **58**, 1437 (1987); E.G. McRae and R.A. Malic, *Phys. Rev.* **B38**, 13163 (1988).
- [2] E.G. McRae, J.M. Landwehr, J.E. McRae, G.H. Gilmer, and M.H. Grabow, *Phys. Rev.* **B38**, 13178 (1988).
- [3] A.W. Denier van der Gon, J.M. Gay, J.W.M. Frenken, and J.F. van der Veen, *Surf. Sci.* **241**, 235 (1991).
- [4] A preliminary account of this work based on lower quality Ge 3d data appears in: T.T. Tran, D.J. Friedman, Y.J. Kim, G.A. Rizzi, and C.S. Fadley in *The Structure of Surfaces III*, S.Y. Tong, M.A. van Hove, K. Takayanagi, and X.D. Xie, Eds. (Springer-Verlag, Berlin 1991) p. 522.
- [5] C.S. Fadley, *Physica Scripta* **T17**, 39 (1987); C.S. Fadley in *Synchrotron Radiation Research: Advances in Surface and Interface Science*, R.Z. Bachrach, Ed. (Plenum Press, New York, 1992).
- [6] A. Szoeké, in *Short Wavelength Coherent Radiation: Generation and Applications*, D.T. Attwood and J. Bokor, AIP Conference Proceedings No.147 (AIP, New York, 1986).
- [7] J.J. Barton, *Phys. Rev. Lett.* **61**, 1356 (1988); J.J. Barton, *J. Electron Spectrosc.* **51**, 37 (1990).
- [8] G.R. Harp, D.K. Saldin, and B.P. Tonner, *Phys. Rev. Lett.* **65**, 1012 (1990).
- [9] S. Thevuthasan, G.S. Herman, A.P. Kaduwela, R.S. Saiki, Y.J. Kim, W. Niemczura, M. Burger, and C.S. Fadley, *Phys. Rev. Lett.* **67**, 469 (1991).
- [10] G.S. Herman, S. Thevuthasan, T.T. Tran, Y.J. Kim, and C.S. Fadley, *Phys. Rev. Lett.* **68**, 650 (1992).

- [11] J. Osterwalder, M. Sagurton, P.J. Orders, C.S. Fadley, B.D. Hermsmeier, and D.J. Friedman, *J. Electron Spectrosc. Relat. Phenom.* **48**, 55 (1989).
- [12] D.J. Friedman and C.S. Fadley, *J. Electron Spectrosc. Relat. Phenom.* **51**, 689 (1990).
- [13] R. Trehan and C.S. Fadley, *Phys. Rev.* **B34**, 6784 (1986).
- [14] S.A. Chambers, *J. Vac. Sci. Technol.* **A7**, 2459 (1989).

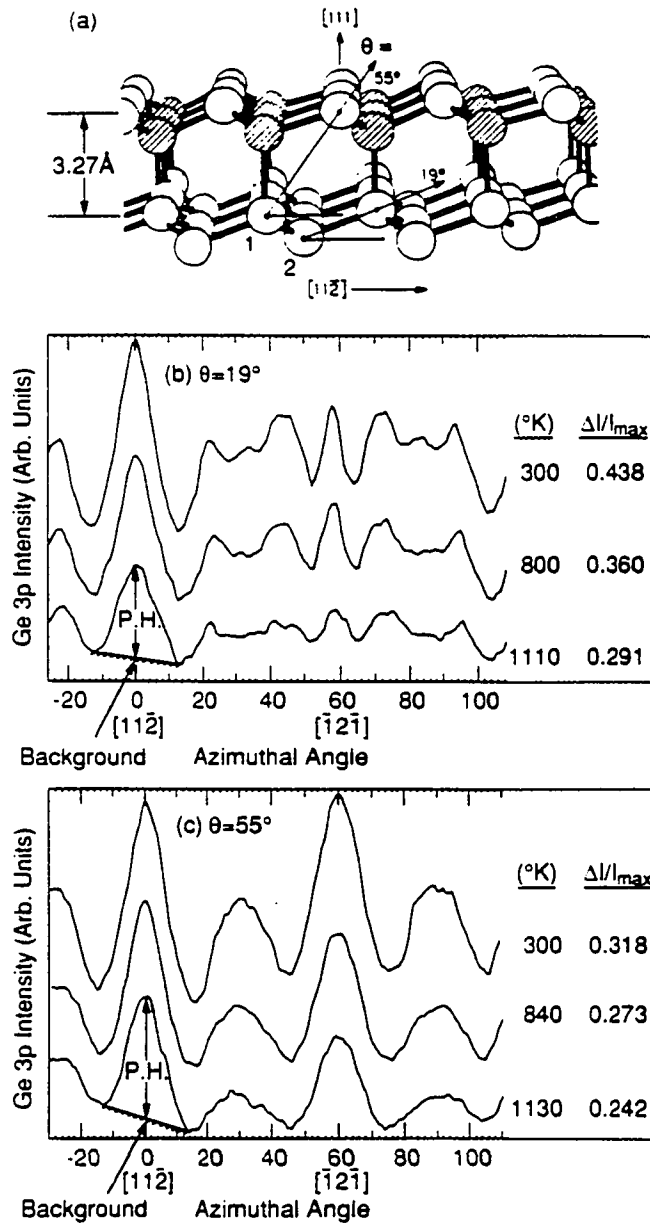


Fig. 4.1.1 (a) An unreconstructed Ge(111) surface showing nearest-neighbor and second-nearest-neighbor scattering directions at takeoff angles of  $\theta=19^\circ$  and  $\theta=55^\circ$  with respect to the surface;  $\phi=0^\circ$  ( $[11\bar{2}]$  azimuth) for both of these directions. (b) Temperature-dependent azimuthal XPD data for Ge 3p emission from Ge(111) at  $1365\text{ eV}$  and a low takeoff angle of  $\theta=19^\circ$ . (c) As (b), but for a takeoff angle of  $\theta=55^\circ$ .

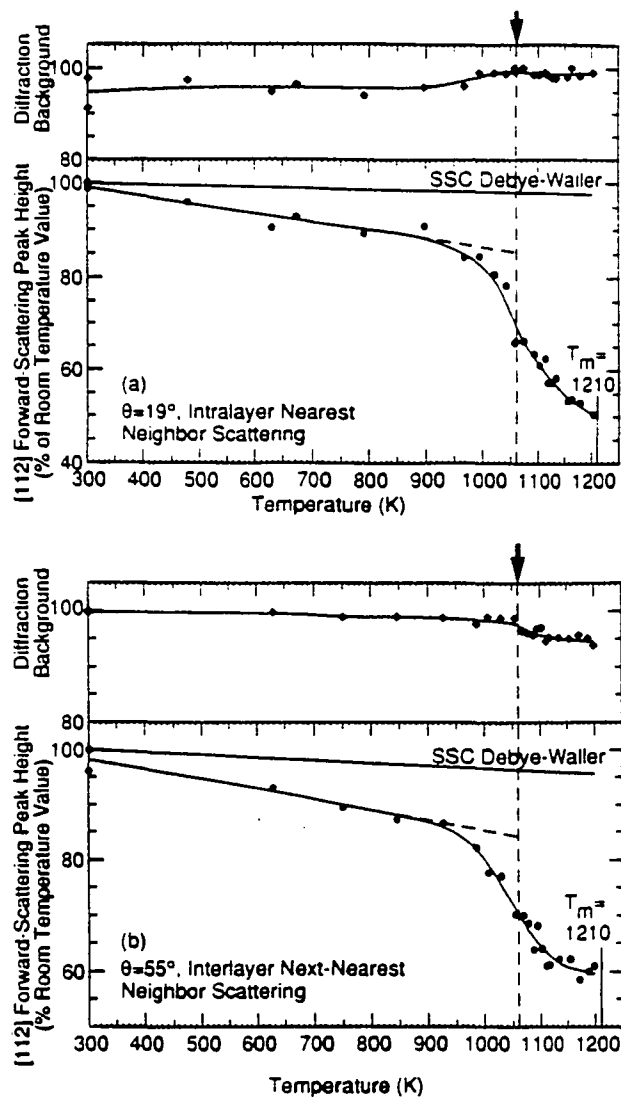


Fig. 4.1.2 (a) The temperature dependence of the height of the nearest-neighbor forward scattering peak in Fig. 4.1.1(b) along  $\theta=19^\circ$ ,  $\phi=0^\circ$ . Also shown are the temperature dependence of the background intensity under the forward scattering peak and the intensity expected on the basis of Debye-Waller effects in a single scattering cluster model. (b) As (a), but for the next-nearest-neighbor forward scattering peak in Fig. 4.1.1(c) along  $\theta=55^\circ$ ,  $\phi=0^\circ$ .

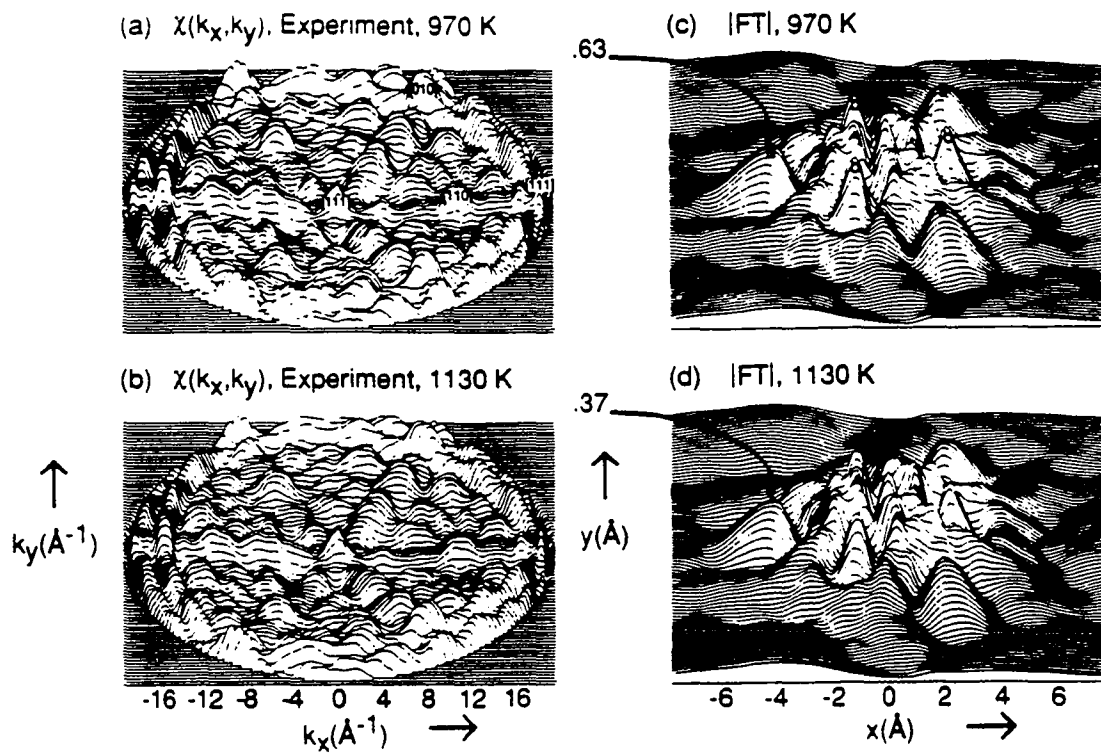


Fig. 4.1.3 (a) Projection of the experimental  $\chi(\vec{k})$  for Ge(111) at 970 K onto the  $k_x$ - $k_y$  plane. Several low-index directions are labeled. (b) As (a), but at 1130 K. (c), (d) Horizontal FT contour plots in the  $z=3.27$  Å plane obtained with Gaussian removal of forward scattering intensities along low-index directions in the initial  $\chi(\vec{k})$  functions of (a), (b). Contour plots are shown at (c) 970 K and (d) 1130 K.

## 4.2 A Detailed Investigation

### 4.2.1 Introduction

Surface phase transitions (SPT's) and surface melting (SM) constitute classes of phenomena which have attracted considerable theoretical and experimental interest [1]. These continuous and often reversible processes occur at temperatures below but often close to the bulk melting point ( $T_m$ ) and may be limited to within the surface and near-surface regions. Their experimental investigation thus requires a surface-sensitive structural probe, a very accurate means of measuring temperature, and a reliable control of surface cleanliness of the material studied. In this chapter, we apply core-level x-ray photoelectron diffraction (XPD) [2] and the related technique of photoelectron holography (PH) [3,4] to the study of a higher-temperature SPT on Ge(111) [5].

In the specific case of Ge(111) with a  $T_m$  of 1210.6 K, both a low-temperature ( $\sim 573$  K) and a high-temperature ( $\sim 1050$  K) SPT have been observed by various techniques. At room temperature, the stable structure of Ge(111) is predominantly  $c(2 \times 8)$ , thought to consist of Ge adatoms bonded on top of a bulk-terminated  $(1 \times 1)$  substrate [6]. However, even this surface is found in scanning tunneling microscopy (STM) studies to be a complex mixture of local adatom geometries [7-9]. Near 573 K, this surface undergoes a low-temperature phase transition leading to an apparent  $(1 \times 1)$  structure as seen by low-energy electron diffraction (LEED). It has been concluded by means of Ge 3d core-level photoemission that in the temperature interval around this phase transition point, the Ge(111) surface is made up of a nonadatom configuration, most probably a  $(2 \times 1)$  reconstruction, in addition to its original room-temperature adatom local arrangement [10]. Furthermore, the proportion of the nonadatom configuration increases with increasing temperature. Most recently, the coexistence of disordered and ordered regions below the transition temperature and the continuous enlargement of the disordered regions with

increasing temperature were observed by STM [8]. The diffusion of surface adatoms in the  $\langle 01\bar{1} \rangle$  directions was observed to be the disordering mechanism and the phase transition was identified as a first-order transition which includes two-dimensional premelting at domain boundaries ("edge melting") [8].

In the high-temperature regime, near 1050 K, the first observation of a SPT on Ge(111) was reported by McRae and Malic [11]. Their LEED data indicated that layerlike crystalline order is preserved in the transition, up to but possibly not including the outermost double layer. Based on the observed sharp decreases in certain LEED spot intensities, an effective thickness of disordering was first estimated to be four to six Ge(111) monolayers (ML). Further analysis and molecular-dynamics (MD) simulations later led to the proposal of a mechanism involving laterally strained domains of atoms to a depth of one double layer of crystalline Ge(111) [12]. The analysis of LEED intensity variations with temperature requires distinguishing between the effects of large-scale disordering and small-scale disordering due to atomic vibrations as most simply described by Debye-Waller (D-W) factors. Molecular-dynamics simulations employing the Stillinger-Weber potential [13] on a Ge crystal of 1440 atoms, and including 6 (111) double layers in a slablike arrangement, confirmed the validity of using a Gaussian distribution of thermal displacements of atoms from their equilibrium positions up to  $T_m$  [12]. Such simulations also ruled out true surface melting as the disordering mechanism; that is, the disordered layer does not diverge to infinite thickness as  $T_m$  is approached, but rather saturates at some limited value. Only in a model crystal that is compressed by 45% in both lateral directions and only above  $0.98 T_m$  did the simulations lead to such a divergent molten Ge(111) overlayer. This study concluded that the disordered overlayer contains both "islands" with the proper crystalline structure as well as regions of disordered Ge atoms. These results from MD simulations are consistent with the LEED experimental data;

however, they are very sensitive to the percent compression assumed in the top double layer. In qualitative support of the idea that the disordered layer is laterally compressed, we also note that the density of liquid Ge is higher than that of solid Ge ( $5.53 \text{ g-cm}^{-3}$  versus  $5.22 \text{ g-cm}^{-3}$ ) and so in the limit of complete melting of a surface layer, it would be expected to contract by about 1.9% along all three directions. These numbers are much smaller than those discussed in the MD study however.

Both the low-temperature and high-temperature SPT's on Ge(111) have also been studied with medium-energy ion scattering (MEIS) by Denier van der Gon and co-workers [14]. Experimental data and Monte Carlo simulations gave an estimate of  $60 \pm 15\%$  for the remaining adatom density after the  $c(2 \times 8)$  to  $(1 \times 1)$  transition at around 573 K, as compared to 100% for the original quarter monolayer present at room temperature. For the high-temperature SPT at 1050 K, a thin film of positionally disordered atoms with a constant thickness of 1 to 1.5 ML was shown to be responsible for the "incomplete melting" of the Ge(111) surface. The high-temperature MEIS results were shown to be in good agreement with predictions based on a theory of Mikheev and Chernov [15] describing the wetting of a solid surface by its own melt. This theory takes into account the layering of the liquid film (therefore making its application to the diamond structure of Ge with pronounced layering normal to the [111] direction very appropriate). The extra stabilization thus associated with each layer leads to oscillations in the free energy of the liquid-like film as a function of its thickness [15]. More details on this theory will be presented in a later section, where we compare our XPD data and their analysis to those from MEIS.

Of the surface sensitive techniques used to study Ge(111) SPT mentioned above, LEED is primarily a long-range order probe (on the order of  $100 \text{ \AA}$  in scale) whereas MEIS and core-level XPD or PH are short-range order probes (on the order of  $10\text{-}20 \text{ \AA}$ ). In XPD [2], the emission direction of core-level photoelectrons above a surface is varied and

intensity modulations produced by scattering and interference effects are measured. At high photoelectron kinetic energies such as the case of Ge 3p at 1365 eV of interest here, forward scattering peaks are the strongest features in these interference patterns, with these peaks being produced by scattering from nearest-neighbor atoms along low-index directions in a crystal. Additional fine structure is also seen in the diffraction patterns due to more complex higher-order interference effects occurring at larger scattering angles. Since the core photoemission process is localized at the site of a specific emitting atom, structural information concerning a given site type can be obtained due to the difference in intensity modulations for atoms in different sites. It is the goal of this study to explore the degree to which temperature-dependent XPD data may help elucidate the mechanism involved in the high-temperature SPT of Ge(111) [5], or in other SPT's in general. To our knowledge, XPD has been used to study only one other surface phase transition: the true surface melting of Pb(110), as carried out by Bonzel et al. [16].

PH, a much newer variation on XPD, is also employed in studying this SPT. Following suggestions first made by Szoeké [3] and later amplified theoretically by Barton [4] that the angular distributions of photoelectron or Auger electron above a single crystal surface form holograms which can be inverted via a two-dimensional Fourier transform (FT) to yield direct images of atomic structure, Tonner, Saldin, and co-workers [17] for the first time showed this procedure to be promising for the analysis of experimental data. In particular, the latter authors found that certain features in the images derived for both Auger emission and elastically back-scattered Kikuchi electrons can be associated with the positions of near-neighbor atoms of typical emitters in both the Cu lattice and an epitaxial overlayer of Cu on Ir(111) [17,18]. Recently, Herman and co-workers [19] have found that features in the holographic images for core-level photoelectrons from Si(111), a semiconductor with an open diamond lattice structure and two symmetry-inequivalent

emitter types that is very similar to the Ge(111) of the present study, also correspond to atomic positions. In addition to these experimental investigations using PH, several recent papers have also pointed out procedures by which holographic images might be improved [18,20-22] to correct for anisotropic-amplitude and/or phase-shift effects in the electron scattering involved that make it deviate from the ideal weak s-wave scattering with zero phase shift that would yield an exact reproduction of the lattice. Without these corrections, the resulting positions of certain near-neighbor atoms in planes nearly perpendicular to the surface and to low-index directions have been accurately predicted to  $\sim\pm 0.2 \text{ \AA}$ , but less accurately ( $\sim\pm 0.5\text{-}1.0 \text{ \AA}$ ) in planes containing low-index directions. In addition, the experimental holographic images obtained to date are often elongated and shifted along low-index directions, effects which are consistent with those expected from both anisotropic amplitudes and phase shifts in the scattering [18,20]. Overall however, the promising nature of PH as a surface structure technique has not been fully assessed and the amount of experimental data of this type remains very limited. We present here the first temperature-dependent PH study to date. Brief and preliminary accounts of this work appears elsewhere [5], but the considerable additional amount of experimental data and theoretical analysis in this paper permits more quantitative conclusions concerning the nature of the transition as measured by different techniques, and also confirms the general utility of XPD and its more recent variation, PH, to the study of surface phase transitions.

#### 4.2.2 Experimental

All photoelectron spectra for both the XPD and PH experiments were obtained with a specially modified Vacuum Generators ESCALAB5 spectrometer [23] equipped with a Surface Science Laboratories Model 3390 multichannel detector [24]. A custom-designed two-axis specimen goniometer permitted angle-resolved capability including high-precision

( $\pm 0.3^\circ$ ) automated rotation of both the polar ( $\theta$ ) and the azimuthal ( $\phi$ ) angles of emission. A non-inductively-wound resistive button heater (Spectra-Mat E-292) placed inside a cylindrical Mo sample holder allowed the specimen temperature to be varied between 300 and 1210 K. Temperature measurements were made with an infrared pyrometer cross-calibrated against chromel-alumel thermocouples and against the melting point of Ge. Standard Al  $K\alpha$  (1486.7 eV) radiation was used for excitation and full UHV conditions of  $5.0 \times 10^{-11}$  torr were maintained throughout all experimental measurements.

The experimental details were described in section 4.1 above. The samples used for this study were Ge single crystal discs of dimensions 0.4 mm thick and 8 mm diameter, cut from commercially-available (Scientific International) mirror-polished wafers (n-type, Sb doped, 5-30  $\Omega$ -cm). The surface orientation was  $(111) \pm 1.0^\circ$  or better as verified by Laue diffraction. Periodic surface cleaning during a continuous series of scans involved sputtering ( $10^{-5}$  torr  $\text{Ar}^+$ , 800 eV, 850 K,  $45^\circ$  off normal incidence, 20 min.) and annealing (970 K, 30 min.). This procedure lead to a highly ordered surface exhibiting a very sharp  $c(2 \times 8)$  LEED pattern with a low background and easily observed quarter-order beams. Surface cleanliness was monitored by XPS core-level peaks and no detectable contaminant peaks (e.g., C 1s or O 1s) were found before or after a full series of diffraction or holographic data.

#### 4.2.3 Results

##### Diffraction data:

In the diffraction experiments, the azimuthal dependence of Ge 3p core-level intensities was studied as a function of temperature from 300 to 1200 K. Azimuthal scans were measured at two polar angles of emission relative to the surface of  $\theta=19^\circ$  and  $55^\circ$ . As can be seen from the scattering geometry shown in Fig. 4.2.1(a),  $19^\circ$  is a surface-sensitive

polar angle containing nearest-neighbor scattering directions, while  $55^\circ$  is a more bulk-sensitive polar angle containing next-nearest-neighbor scattering directions. For  $\theta=19^\circ$ , both the emitter and scatterer are found in the same double layer whereas for  $\theta=55^\circ$ , they are located in different double layers.

For these two takeoff angles, we can estimate the corresponding sampling depths. First, using the standard equations for the overlayer attenuation in XPS intensities [23] we obtain the contributions to the total observed Ge 3p intensity from each layer of atoms inward from the surface. For  $\theta=19^\circ$ , these values are 17.4, 15.7, 11.6, 10.5, 7.8 and 7.0 percent for the first six atomic layers beginning with the topmost surface layer. In this case, the mean depth of emission (i.e., the depth that gives 50% of the total intensity) is two double layers and the depth yielding 90% of the total intensity is six double layers. Similarly, for  $\theta=55^\circ$ , the contributions to the total intensity from each of the topmost six layers are 7.5, 7.2, 6.4, 6.2, 5.5, and 5.3 percent leading to a mean depth of emission of 4.5 double layers and a 90%-contribution depth of 14 double layers. In addition, a second consideration in estimating sampling depths is to include both inelastic attenuation and multiple scattering defocussing, which yields mean depths of emission of 1 and 1.5 double layers and 90%-contribution depths of 2 and 2.5 double layers for the two low-index directions of particular interest,  $\theta=19^\circ$  and  $55^\circ$ , respectively.

Figures 4.2.1(b) and 4.2.1(c) show azimuthal scans taken at 300, 800, and 1110 K for  $\theta=19^\circ$  and at 300, 840, and 1130 K for  $\theta=55^\circ$ , respectively. With increasing temperature, all peaks in the azimuthal curves are reduced in intensity, although their shapes and positions are not significantly altered. More specifically, comparing azimuthal scans in Fig. 4.2.1(b) taken at 800 and 1110 K (that is, just below and just above the expected phase transition point), we find that the two main peaks at  $\phi=0^\circ$  (along the  $[11\bar{2}]$  azimuth) and  $\phi=60^\circ$  (along the  $[\bar{1}2\bar{1}]$  azimuth) are both much reduced in absolute intensity.

The fine structure between these two peaks, from about  $\phi=14^\circ$  to  $52^\circ$ , also is reduced in intensity, but with only slight changes in its form. Similar conclusions are obtained for the data at  $\theta=55^\circ$  in Fig. 4.2.1(c).

Azimuthal scans over the peak along the  $[11\bar{2}]$  azimuth in Fig. 4.2.1(b) were then measured as the sample temperature was varied in small increments. Figure 4.2.2 shows these more detailed intensity and background measurements as a function of temperature. Figure 4.2.2(a) presents the absolute background intensity under the  $[11\bar{2}]$  forward scattering peak at  $\theta=19^\circ$  (cf. Fig. 4.2.1(b)) and Fig. 4.2.2(b) shows the  $[11\bar{2}]$  peak height (P.H.), which we will refer to as  $\Delta I(T)$ , both plotted as a function of temperature.  $\Delta I(T)$  values at different temperatures are shown normalized to the highest  $\Delta I(T)$  value. In Figs. 4.2.2(c) and 4.2.2(d), analogous results are plotted for emission at  $\theta=55^\circ$ . The points in Fig. 4.2.2 were obtained with both increasing and decreasing temperature and the forms of the curves were found to be identical in both cases. It is thus clear from Fig. 4.2.2(b) that an abrupt and reversible drop of about 43% in the forward-diffracted intensity for  $\theta=19^\circ$  occurs over the interval 900-1200 K. A similar drop of about 31% is seen in Fig. 4.2.2(d) for  $\theta=55^\circ$ . By contrast, the background intensities at both  $\theta$  values exhibit only very small, and probably not physically significant, deviations from constancy.

The drops in peak intensity at 1060 K cannot be explained by simple thermal vibrations. Debye-Waller (D-W) effects are expected to yield a smooth and approximately linear decrease with temperature in the intensity of the forward scattering peak [25], unlike the step-like transition observed. Model calculations of such a D-W attenuation in a simple single scattering cluster (SSC) approximation [2,26] are shown as the solid straight lines in Fig. 4.2.2. The experimental lines (as indicated by  $W_\theta(T)$ ) have slopes of -1.9 %/K for  $\theta=19^\circ$  and -1.8 %/K for  $\theta=55^\circ$ , that are approximately 8.5x greater than those of these simple calculations.

We can extend this analysis of the region below the transition further by following a procedure introduced previously by Trehan and Fadley [25]. Specifically, this proceeds by introducing a theoretically-derived effective scattering angle  $\bar{\theta}_j$  as averaged over all strong scatterers in the XPD emission which yields an approximate temperature dependence for the sum over all scattering atoms  $j$  of:

$$\Delta I/I_{\max} \propto \exp[-2k^2 (1-\cos\bar{\theta}_j) \langle U_j^2(T) \rangle] \quad (4.1)$$

where  $k$  is the electron wave vector and  $\langle U_j^2(T) \rangle$  is the mean-squared displacement. At the high-temperature limit of the Debye model as appropriate for our experiments, the mean-squared displacement is given by:

$$\langle U_j^2(T) \rangle = 3\hbar^2 T/Mk_B\Theta_D^2 \quad (4.2)$$

where  $\hbar$  is the Planck's constant divided by  $2\pi$ ,  $T$  is the temperature in Kelvin,  $M$  is the mass of the atom,  $k_B$  is the Boltzmann constant, and  $\Theta_D$  is the Debye temperature. From plots similar to Fig. 4.2.2 but of  $\ln(\Delta I/I_{\max})$  versus temperature, four slopes of the linear temperature dependence in the 300-900 K range can be obtained: (1) a theoretical D-W slope for  $\theta=19^\circ$  of  $-5.16 \times 10^{-6} \text{ K}^{-1}$ , (2) an experimental slope for  $\theta=19^\circ$  of  $-1.3 \times 10^{-4} \text{ K}^{-1}$ , (3) a theoretical D-W slope for  $\theta=55^\circ$  of  $-7.7 \times 10^{-6} \text{ K}^{-1}$ , and (4) an experimental slope for  $\theta=55^\circ$  of  $-1.2 \times 10^{-4} \text{ K}^{-1}$ . First, from the theoretical D-W slopes and a  $\Theta_D$  for Ge of 374 K, effective scattering angles  $\bar{\theta}_j$  of  $1.8^\circ$  and  $2.2^\circ$  are obtained for  $\theta=19^\circ$  and  $\theta=55^\circ$ , respectively (i.e., forward single scattering dominates the calculated diffraction pattern). Then, together with the experimental slopes, these  $\bar{\theta}_j$  values in turn yield effective Debye temperatures of  $\Theta_D(\text{effective})=74 \text{ K}$  and  $\Theta_D(\text{effective})=93 \text{ K}$  for  $\theta=19^\circ$  and  $\theta=55^\circ$ ,

respectively. These values are thus about 4x smaller than the bulk value, a result which is consistent with multiple scattering events up to 4<sup>th</sup> or 5<sup>th</sup> order being important for describing the temperature dependence of the experimental data adequately. As a comparison, a prior similar analysis [25] of the temperature-dependent anisotropies for Cu 2p<sub>3/2</sub> at  $\theta=7^\circ$  and  $\theta=45^\circ$  yielded  $\bar{\theta}_j$  values of 17.7° and 7.3° and  $\Theta_D(\text{effective})$  values of 286 K and 117 K, respectively (the bulk Debye temperature for Cu is 343 K). Thus, although such simple single scattering D-W calculations significantly underestimate the attenuation of the forward scattering peak height with temperature and to yield effective Debye temperatures that are much reduced in value compared to the expected value of 374 K for Ge (an observation made previously in the analysis of XPD data from Cu(001) [25]), they at least qualitatively explain the experimental behavior below 900 K. However, the transition itself must be due to a larger-scale motion of the surface atoms, as proposed previously [11].

#### Holographic data:

In the holographic experiments, full intensity profiles for Ge 3p photoelectrons were measured at 300, 970, and 1130 K. These profiles consisted of azimuthal scans, similar to those shown in Figs. 4.2.1(b) and 4.2.1(c) and with 1.8° steps over 80° in  $\phi$ , which were then symmetry-reflected to give the full 360° in azimuth. The polar angle  $\theta$  was varied from grazing emission at  $\theta=10^\circ$  up to the normal at  $\theta=90^\circ$  in 1.8° steps.

In order to derive positional information that will help describe the nature of the phase transition, the full intensity profiles collected as described above were analyzed according to a procedure previously described by Barton [4]: (1) the three-dimensional intensity distribution  $I(\vec{k})$  in the electron wave vector  $\vec{k}$ , with angles of emission  $\theta$  and  $\phi$ , is converted to a normalized  $\chi(\vec{k})$ , where  $\chi(\vec{k})=[I(\vec{k})-I_0(\vec{k})]/I_0(\vec{k})^{1/2}$ , with the unscattered intensity  $I_0(\vec{k})$  needed for normalization being obtained from polar-scan data for a heavily

ion-bombarded surface in which no diffraction features were seen; (2) this  $\chi(\vec{k})$  is then projected onto the  $k_x, k_y$  plane and the average value of  $\chi(\vec{k})$  is set to zero, and, (3) after multiplication by a phase factor  $\exp[ik_z z]$   $\chi(\vec{k})$  is Fourier transformed in  $k_x$  and  $k_y$  to yield what ideally is a cross section of the image in a plane at a distance  $z$  along [111] relative to a given emitter.

Each intensity distribution or hologram thus occupies a cone centered along the  $z=[111]$  axis, with a full angle given by  $\alpha=160^\circ$ . In Figs. 4.2.3(a), 4.2.3(b), and 4.2.3(c) we show the experimental  $\chi(\vec{k})$  data for Ge(111) taken at temperatures of 300, 970, and 1130 K, respectively. Several low-index forward scattering directions with the most dense rows of scattering atoms along them are labeled in Fig. 4.2.3(b). Without any further analysis of these data, we can already note that there are no significant changes in any of the diffraction features in these  $\chi(\vec{k})$  curves as temperature is raised. After normalization to have the same maximum peak heights in these plots, the three sets of data are in fact remarkably alike, in agreement with the behavior of the individual curves in Fig. 4.2.1 discussed previously. The only noticeable difference is the greater statistical error in the higher temperature data due to the reduced absolute intensities involved (cf. Fig. 4.2.1).

In finally transforming these  $\chi(\vec{k})$  data to yield holographic images, we have followed a method suggested by Thevuthasan et al. [22] which has been shown to yield better subsequent Fourier transform (FT) image quality by reducing non-ideal scattering anisotropy due to forward scattering. We have multiplied the experimental  $\chi(\vec{k})$  by a Gaussian function of the form  $[1-\exp(-0.691\delta^2/\gamma^2)]$ , where  $\delta$  is the angular deviation of  $\vec{k}$  from a given low-index forward scattering axis and  $\gamma$  is a variable half-width at half maximum intensity (HWHM). This function was applied to reduce the value of  $\chi(\vec{k})$  along the highest-density  $\langle 11\bar{1} \rangle$ ,  $\langle 010 \rangle$ ,  $\langle 110 \rangle$ , and [111] directions to zero, with a HWHM of  $7.5^\circ$  being used for all directions. Figures. 4.2.4(a), 4.2.4(b), and 4.2.4(c) show

normalized images obtained after holographic inversion with Gaussian multiplication of the experimental data shown in Figs. 4.2.3(a), 4.2.3(b), and 4.2.3(c). The plane of these images at  $z=3.27\text{\AA}$  contains 6 near-neighbor atoms in the first double layer above a given emitter of either type 1 or type 2 in Fig. 4.2.1(a); the expected positions of these neighbors are labeled "a" and "b" in Fig. 4.2.4(b). The value of  $z=3.27\text{\AA}$  has been chosen to yield a plane in which the holographic images around both types of emitter should be identical as discussed previously for the very similar case of Si(111) by Herman et al. [19]. The relative intensity of the "a" peaks in these images are 1.0, 0.63, and 0.37 for 300, 970, and 1130 K, respectively. Once normalized, however, all the features observed at the three different temperatures become essentially identical, in particular for the two highest temperatures. The near-identity of these holographic near-neighbor images above and below the transition temperature are fully consistent with the high degree of similarity of the starting  $\chi(\vec{k})$  data, with both sets of results thus indicating an identical near-neighbor structure for all Ge atoms that are present in ordered sites.

#### 4.2.4 Discussion

In order to discuss our results in the context of previous closely related experimental work, mainly the XPD study of surface melting of Pb(110) [16] and the MEIS study of disorder transitions on the Ge(111) surface [14], we begin with the analysis of our XPD data. The effect of the SPT can be isolated by first dividing out the "normal" vibrational attenuation of diffraction as estimated over the temperature range of 300-900 K. The D-W curves shown as straight lines in Fig. 4.2.2 and obtained from simple SSC calculations, were not used for this purpose since they do not include contributions from multiple scattering [27] and detailed phonon modes [28], and do not adequately describe the experimental data below the transition. Instead, the correction for the experimental D-W

effect is accomplished by first fitting a linear function  $W_{\theta}(T)$  to the peak-height data points  $\Delta I_{\theta}(T)$  within the range of 300-900 K in Figs. 4.2.2. The vibrationally-corrected peak height changes for each  $\theta$  can then be represented as  $\Delta \hat{I}_{\theta}(T) = \Delta I_{\theta}(T) / W_{\theta}(T)$ . In order to test whether the SPT follows a simple logarithmic growth law [16], we plot in Fig. 4.2.5  $\ln \Delta \hat{I}_{\theta}(T)$  versus  $\ln(T_m - T)$  for the  $[11\bar{2}]$  forward scattering peaks at  $\theta = 19^\circ$  and  $55^\circ$ . The data exhibit different behaviors in three distinct temperature ranges: (I) in the lower temperature region below the SPT, the D-W corrected data show no temperature dependence, as expected from the way the correction is defined; (II) in the region between  $\sim 900$  and  $\sim 1130$  K, the slopes are 0.37 and 0.34 for  $\theta = 19^\circ$  and  $55^\circ$ , respectively, yielding good agreement as to the form of the transition between the two takeoff angles; and (III) in the highest temperature region up to 1200 K, there is a negligible slope of 0.0083 in the case of  $\theta = 19^\circ$  and a slope of zero in the case of  $\theta = 55^\circ$ . The constant, non-divergent nature of the data in region (III), in contrast to the divergent (slope=0.3) behavior observed for Pb(110) [16], clearly indicates that the Ge(111) high-temperature SPT in the present study is not a surface melting transition that continues to bulk melting with increasing temperature. These results further suggest that, although the SPT is initiated at  $\sim 900$  K and the thickness of the disordered layer on top of the ordered lattice increases in temperature region (II), this thickness reaches a saturation point at  $\sim 1160$ - $1190$  K and remains constant over much of region (III).

Both our diffraction and holography results are also consistent with the gradual growth of a disordered, liquid-like layer on the Ge surface, with an ordered substrate remaining underneath. This model explains why all ordered emitters yield both the same diffraction curves and resulting holograms, and why the holographic images do not change with temperature. Thus, we suppose that all emitters in the disordered overlayer yield an isotropic intensity profile, or more correctly, one that would follow the unscattered  $I_0$  that

was used to derive  $\chi(\vec{k})$ . With these assumptions, the thickness of the disordered overlayer at any temperature  $T$  can be estimated from the inelastic attenuation it produces on a diffraction peak intensity upon passing through the transition as follows:

$$\Delta\hat{I}(T) = \Delta\hat{I}(T_0)\exp[-d/\lambda_e\sin\theta] \quad (4.3)$$

where  $T_0$  is the onset temperature of the SPT,  $d$  is the overlayer thickness,  $\lambda_e$  is the inelastic attenuation length, and  $\theta$  is the takeoff angle as defined previously. Taking the onset temperature  $T_0$  of the transition to be 900 K, and a  $\lambda_e$  of 25 Å for Ge as measured previously by Chambers [29], we obtain the thickness increase of the overlayer as a function of temperature shown in Fig. 4.2.6(a). As expected, the first appearance of the overlayer occurs at ~900 K. The maximum overlayer thickness reached by 1200 K is determined to be 2.5 ML for the  $\theta=19^\circ$  data and 3.9 ML for the  $\theta=55^\circ$  data. The reasons for two different overlayer thicknesses obtained from data taken at the two different takeoff angles will be discussed in more detail later.

Our results can now be compared directly to MEIS results [14] for the same transition, as shown also in Fig. 4.2.6(a). The absolute thickness values derived from the XPD data are significantly larger than the 1-1.5 ML obtained from MEIS [14]. However, if the XPD and MEIS results are normalized to the same minimum and maximum values, as has been done in Fig. 4.2.6(b), it is clear that both our sets of XPD data show excellent agreement with one another and also with the MEIS data in terms of both the onset temperature of the SPT as well as the shape of the overlayer thickness growth versus temperature. In fact, it is rather remarkable that two such different short-range order probes as XPD and MEIS are in such good agreement as to the fundamental form of the transition.

In order to compare the two types of experiments more quantitatively and also in an attempt to better understand the difference in the estimate of the overlayer thickness, we examine more closely a theory developed by Chernov and Mikheev for the wetting of a surface by its own dense liquid [15] and the prior application of this theory to the MEIS results [14].

This begins by assuming that the fluctuations in the position of a liquid-vapor interface on a flat solid substrate are described by the Hamiltonian:

$$\mathcal{H} = \int d^2x \left\{ \frac{1}{2} \sigma (\nabla h)^2 + V(h) \right\} \quad (4.4)$$

where  $x$  is the 2D coordinate vector in the substrate plane,  $\sigma$  is the surface free energy of the bulk liquid,  $h$  is the equilibrium thickness of the liquid film that is adsorbed to the substrate, and  $V(h)$  is an effective interface-substrate interaction potential. Considering only the square-gradient (Landau) model of the liquid yields:

$$V(h) = V_L(h) = -a \exp(h/\xi_l) + b \exp(-2h/\xi_l) \quad (4.5)$$

where  $a$  and  $b$  are constants discussed in more detail below,  $\xi_l$  is the bulk correlation length of the liquid, and the long-range potential of Van der Waals forces is found to lead to correct descriptions of simple systems. However, a more general form of the interfacial potential requires taking into account contributions from the long-range attraction of the interface to the substrate due to hydrodynamic correlations, as well as contributions from the oscillatory potential in dense liquids due to the strong layerwise short-range order.

As an improvement to these Landau-type theories that are often used to describe surface wetting/melting, Chernov and Mikheev's theory further incorporates the layering,

parallel to the surface, of the liquid film, and this layering is assumed to lead to oscillations in the free energy of the film as a function of its thickness [15]. The final change in free energy per unit area,  $\Delta F$ , as a function of the film thickness,  $h$ , can in this model be written as:

$$\Delta F = h L_v(1-T/T_m) - \Delta\gamma - a \cos(k_1 h) \exp[-h/\xi_l] + b \exp[-2h/\xi_l] \quad (4.6)$$

where  $L_v$  is the latent heat of melting per unit volume,  $k_1$  is the reciprocal distance at which the first maximum occurs in the structure factor of the liquid,  $\xi_l$  is the correlation length in the bulk liquid. The second term,  $\Delta\gamma$  is given as  $\Delta\gamma = \gamma_{sv} - \gamma_{lv} - \gamma_{sl}$  where the  $\gamma$ 's are the different interfacial free energies of the dry solid-vapor, the liquid-vapor, and the solid-liquid interfaces, respectively, in the absence of a disordered liquid film. The parameters  $a$  and  $b$  balance between the layering effect as given by the third term and the residual order within the film as given by the fourth term, and they can be calculated from  $\Delta\gamma = -a + b$  and from:

$$\gamma'_{sv} = \gamma_{sl} + \gamma_{lv} - a \exp[-2\pi/k_1 \xi_l] + b \exp[-4\pi/k_1 \xi_l] \quad (4.7)$$

The values used in Ref. 14 were:  $L_v = 2.6 \times 10^9 \text{ J m}^{-3}$ ,  $k_1 = 2.56 \text{ \AA}^{-1}$ ,  $T_m = 1210.6 \text{ K}$ , and  $\xi_l = 5.3 \text{ \AA}$ . The experimental contact angle between Ge(l) and Ge(s) of  $\theta = 30^\circ$  [30] was used in this prior study to determine  $\gamma'_{sv}$ , the interfacial free energy of the solid-vapor interface in the presence of a disordered liquid film, from the relationship  $\gamma'_{sv} = \gamma_{sl} + \gamma_{lv} \cos\theta$ . This led to values of  $\Delta\gamma = \gamma_{sv} - \gamma_{lv} - \gamma_{sl} = 0.83 \text{ J m}^{-2} - 0.63 \text{ J m}^{-2} - 0.24 \text{ J m}^{-2} = -0.04 \text{ J m}^{-2}$  [14]. These values when combined with Eq. 4.7 gave estimates of  $0.295 \text{ J m}^{-2}$  and  $0.252 \text{ J m}^{-2}$

for the two parameters  $a$  and  $b$ , respectively [14]. The resulting dependence of the change in free energy,  $\Delta F$ , on the overlayer thickness is shown as the dashed curves in Fig. 4.2.7.

In an attempt to examine more closely the behavior of the free energy versus overlayer thickness curves at different temperatures, we have varied a few the above parameters within reasonable ranges. For our calculations, a value of  $0.91 \text{ J m}^{-2}$  for  $\gamma_{sv}$ , leading to the physically plausible case where  $\Delta\gamma > 0$  and a contact angle of  $21^\circ$  were used. More specifically, estimates of  $a = 0.25 \text{ J m}^{-2}$  and  $b = 0.29 \text{ J m}^{-2}$  followed from these new values. With all other parameters kept the same as in Ref. 14, we obtain the dependence of the change in free energy,  $\Delta F$ , on the overlayer thickness shown as the solid curves in Fig. 4.2.7. Below 1050 K (not shown in Fig. 4.2.7), the absolute minimum in  $\Delta F$  occurs at  $h=0$ , indicative of a completely dry surface with no overlayer. At 1050 K, shown in Fig. 4.2.7(a), a second minimum of  $\Delta F=0$  appears at  $h$  (in units of  $2\pi/k_1$ )=1, indicating the formation of an overlayer of thickness  $h=2.45 \text{ \AA}$ . As the temperature is increased to 1125 K, a third local minimum in  $\Delta F$  reaches zero (cf. Fig. 4.2.7(b)). However, since the absolute minimum is still at  $h=2\pi/k_1$ , the overlayer of thickness  $2.45 \text{ \AA}$  remains as the most stable configuration. As the temperature reaches 1200 K, however, the third local minimum crosses over  $\Delta F=0$  and passes the second local minimum at  $h=2\pi/k_1$  to become the absolute minimum at  $h=2(2\pi/k_1)=4.91 \text{ \AA}$ . Taking the density of liquid Ge to be  $5.50 \text{ g/cm}^3$  [31], the disordered overlayer of thickness  $4.91 \text{ \AA}$  corresponds to  $2.24 \times 10^{15} \text{ atoms/cm}^2$ , or 3.10 ML. These results are then in qualitative agreement with our XPD data and our estimation of overlayer thicknesses of 2.5 ML for  $\theta=19^\circ$  and 3.9 ML for  $\theta=55^\circ$ , as derived from the inelastic attenuation of forward scattering peak intensities as shown in Fig. 4.2.6(a). In the calculations by Denier van der Gon et al. [14] with slightly different parameters, the thickness  $h$  does not go beyond  $h=2.45 \text{ \AA}$ .

The difference in the estimated overlayer thickness from the XPD data at  $\theta=19^\circ$  and  $55^\circ$  may be due to a laterally strained double layer of Ge atoms located between the fully disordered overlayer and the ideal bulk-terminated surface. As can be seen from Fig. 4.2.1(a), the nearest-neighbor forward scattering for  $\theta=19^\circ$  is confined within one double layer. That is, both atoms, the emitter and the scatterer, are located in the same double layer. This more surface sensitive  $\theta=19^\circ$  case is then expected to probe intra-double-layer disordering. If a laterally strained (and probably laterally-compressed) double layer were present such that there were a loss of registry between it and the bulk atoms, the forward scattering peak height for  $\theta=19^\circ$  along the  $[11\bar{2}]$  azimuth would not be affected to first-order since the nearest-neighbor forward scattering bond direction is the same in the strained double layer as it is in the bulk. On the other hand, the two atoms forming the  $55^\circ$  scattering direction are in different double layers such that inter-double-layer disordering is probed in these data. Any lateral strain in a double layer with respect to the bulk beneath it will cause a change in the forward scattering angle resulting in a decrease in the forward scattering peak height. Thus, our XPD experimental data best fit a model in which there are approximately two monolayers (i.e., one double layer) of fully disordered overlayer, then one-to-two laterally-strained monolayers, and finally an ordered bulk-terminating substrate surface. This model thus can explain the discrepancy between the overlayer thicknesses derived from data taken at the two different  $\theta$  values. At  $\theta=19^\circ$ , only two monolayers contribute to the loss in forward scattering intensity while at  $\theta=55^\circ$ , both the two monolayers of fully disordered atoms as well as the one-to-two laterally strained monolayers beneath them contribute to the loss in forward scattering intensity.

The normalized intensity profiles  $\chi(\vec{k})$  at 300, 970, and 1130 K and their corresponding holographic images in Fig. 4.2.4 provide information on the ordered crystal lattice below the disordered overlayer. However, since the intensity profiles at the three

different temperatures are each made up of azimuthal scans, similar to those shown in Figs. 4.2.1(b) and 4.2.1(c), but taken at different polar angles  $\theta$  from grazing emission at  $\theta=10^\circ$  up to the normal at  $\theta=90^\circ$  in  $1.8^\circ$  steps, they add another dimension to our analysis: changes in the overall intensity and the azimuthal pattern as a function of polar angle.

Figure 4.2.8(a) shows the ratio of azimuthally-averaged total absolute intensities at two different temperatures, 1130 K (just above the transition) and 970 K (just below the transition). That is, we plot the total-intensity ratio  $\bar{I}_\theta(1130 \text{ K})/\bar{I}_\theta(970 \text{ K})$  from all of the azimuthal scans contributing to the data in Figs. 4.2.3(b) and 4.2.3(c). All of these values are very close to unity, with a gentle slope in the curve leading from about 0.93 at the lowest angles to 0.98 at the highest angles; that is, very little total intensity is lost in going through the transition. This can be understood by noting that the intensity from the ordered bulk crystal lattice and that from the disordered overlayer together yield the total intensity. For a semi-infinite ordered substrate covered by a uniform disordered overlayer of thickness  $d$ , the average intensity from the ordered substrate for an emission direction  $\theta$  and at a fixed kinetic energy  $E_k$  is given as [23]:

$$\bar{I}_\theta(\text{ordered})=I_0\Omega_0(E_k)A_0(E_k)D_0(E_k)\rho(d\sigma_k/d\Omega)\lambda_e(E_k)\exp(-d/\lambda'_e(E_k)\sin\theta) \quad (4.8)$$

where  $I_0$  is the incident x-ray flux,  $\Omega_0$  is the effective solid angle of the analyzer,  $A_0$  is the effective specimen area both illuminated and seen by the analyzer,  $D_0$  is the instrumental detection efficiency,  $\rho$  is the atomic density of the substrate,  $d\sigma_k/d\Omega$  is the differential cross section,  $\lambda_e$  is the inelastic photoelectron attenuation length in the substrate, and  $\lambda'_e$  is the attenuation length in the overlayer. This equation is strictly speaking valid only in the absence of any non-isotropic elastic scattering effects: that is, when diffraction is either absent or completely averaged over. We will here assume however, that averaging total

intensity over a single azimuthal scan at  $\theta$  is sufficient to yield something that is very close to averaging out all diffraction. The intensity from the disordered overlayer of thickness  $d$  at a kinetic energy  $E_l = E_k$  is similarly given as [23]:

$$\bar{I}_\theta(\text{disordered}) = I_0 \Omega_0(E_k) A_0(E_k) D_0(E_k) \rho' (d\sigma_k/d\Omega) \lambda'_e(E_k) [1 - \exp(-d/\lambda'_e(E_k) \sin\theta)] \quad (4.9)$$

where  $\rho'$  refers to the atomic density of the overlayer. If we now further assume that  $\rho = \rho'$  and  $\lambda_e = \lambda'_e$ , then the sum of  $\bar{I}_\theta(\text{ordered})$  and  $\bar{I}_\theta(\text{disordered})$  is predicted to remain constant at one value for the clean surface below the disorder transition:

$$\bar{I}_\theta(\text{ordered}) + \bar{I}_\theta(\text{disordered}) = I_0 \Omega_0(E_k) A_0(E_k) D_0(E_k) \rho (d\sigma_k/d\Omega) \lambda_e(E_k) \quad (4.10)$$

However, if we do not make such simplifying assumptions, then this sum becomes:

$$\begin{aligned} \bar{I}_\theta(\text{ordered}) + \bar{I}_\theta(\text{disordered}) = I_0 \Omega_0(E_k) A_0(E_k) D_0(E_k) \\ \times \{ \rho (d\sigma_k/d\Omega) \lambda_e(E_k) \exp(-d/\lambda_e(E_k) \sin\theta) \\ + \rho' (d\sigma_k/d\Omega) \lambda'_e(E_k) [1 - \exp(-d/\lambda'_e(E_k) \sin\theta)] \} \quad (4.11) \end{aligned}$$

The fact that there is a slight decrease in the intensity ratio over the transition of up to 8% could be due to an effective decrease in the electron attenuation length in the disordered overlayer (e.g. due to the greater disorder, enhanced vibrational effects, and/or a higher density). In fact, a model calculation using  $\rho' = 5.53 \text{ gcm}^{-3}$  and  $\rho = 5.22 \text{ gcm}^{-3}$  (the density of liquid and solid Ge at the melting point, respectively),  $\lambda_e = 25 \text{ \AA}$ ,  $\lambda'_e = 20 \text{ \AA}$  (or a value for the photoelectron attenuation length in the liquid that is 80% of that in the solid), and  $d = 3.27 \text{ \AA}$  (the average of our two experimental values for  $d$ ), yields the solid curve shown

superimposed on the data points in Fig. 4.2.8(a). This curve represents an excellent fit to the experimental values. Overall, however, our conclusion is still that the near constancy in Fig. 4.2.8(a) is just what is expected for the overlayer model under consideration.

Fig. 4.2.8(b) now shows the overall anisotropy, which we measure as  $(I_{\max} - I_{\min})/I_{\max}$ , plotted as a function of  $1/\sin\theta$  for each of the azimuthal scans and at each of the three temperatures. This curve simply measures the degree to which strong (usually forward scattering) peaks arise in the diffraction pattern for a given  $\theta$ . Thus, peaks are seen in all three of these curves for  $\theta$  approximately equal to 19-20°, 30-35°, and 55-60°, all of which are identifiable with low-index directions for forward scattering above the (111) surface [2]. Exactly along the normal, the values artificially go to zero because an azimuthal scan does not average over enough solid angle to show any variation in  $I_{\max} - I_{\min}$ .

As a final aspect of these large sets of holographic azimuthal scans, we ask how these data can add to the description of the Ge(111) high-temperature SPT and specifically whether an additional estimate of overlayer thickness can be derived from them. Keeping in mind the inelastic attenuation of a diffraction peak intensity caused by the presence of a disordered overlayer, we can rewrite Eq. 4.3 slightly as:

$$\Delta\hat{I}(T_{\text{high}})/\Delta\hat{I}(T_{\text{low}}) = \exp[-\Delta d/\lambda_e \sin\theta] \quad (4.12)$$

where the high and low temperatures now need not be fully above or below the transition, and it is thus only the change in layer thickness  $\Delta d$  over a more limited temperature interval that accounts for the attenuation observed. Of the three temperatures where data were taken, two fall within the high-temperature SPT region. We thus take  $T_{\text{high}}$  as 1130 K and  $T_{\text{low}}$  as 970 K, and directly obtain Fig. 4.2.8(c), which shows  $\ln[\Delta\hat{I}(1130\text{K})/\Delta\hat{I}(970\text{K})]$

as a function of  $1/\sin\theta$ . From the slope of the best-fit straight line going through the data points in Fig. 4.2.8(c) of  $-\Delta d/\lambda_e = -0.104$ , we obtain  $\Delta d_{970-1130\text{K}} = 2.61 \text{ \AA}$ . However, based on the XPD data in Fig. 4.2.2, we know that the range from 970 to 1130 K does not cover the entire SPT. Instead, the  $\Delta d_{970-1130\text{K}}$  value obtained above needs to be scaled to a temperature range of 900-1200 K in order to fully describe the complete transition region. Scaling factors of 1.51 obtained from the XPD data for  $\theta = 19^\circ$  and 1.27 for  $\theta = 55^\circ$  yield  $\Delta d_{900-1200\text{K}}$  values of  $3.9 \text{ \AA}$  (2.4 ML) and  $3.3 \text{ \AA}$  (2.0 ML), respectively, that are in good agreement with the 2.5-3.9 ML derived previously from two separate studies at  $\theta = 19^\circ$  and  $55^\circ$ . Our prior value of 3.9 ML for  $\theta = 55^\circ$  is however, somewhat high as judged against this self-consistent analysis of the holography data.

#### 4.2.5 Summary

This investigation of the Ge(111) high-temperature surface phase transition (SPT) by x-ray photoelectron diffraction (XPD) and photoelectron holography (PH) yields excellent agreement with previous LEED and MEIS studies in three aspects: 1) a model for the SPT involving an ordered substrate covered by a disordered overlayer, 2) an onset temperature for the SPT of 900 K and a saturation of the overlayer thickness at  $\sim 1160-1190 \text{ K}$ , and 3) the rate of development of the overlayer thickness as a function of temperature (particularly in comparison to MEIS data). However, our XPD and PH results lead to somewhat higher estimates of 2.5-3.9 ML and 2.0-2.4 ML, respectively, for the liquid-like overlayer thickness, as compared to 2 ML from molecular dynamics simulations in conjunction with LEED results and 1.0-1.5 ML from MEIS. LEED, MEIS, PH, and XPD together thus provide a complete and complementary collection of information on the Ge(111) high-temperature surface phase transition.

Our XPD data taken for  $\theta=19^\circ$  and  $55^\circ$  yield different values for the disordered attenuating layer of 2.5 ML and 3.9 ML, respectively. This difference was justified by the possibility of having a laterally-strained double layer located beneath the disordered layer. The direct forward scattering directions for  $\theta=19^\circ$  is intra-layer (although a small portion of the effect is also from inter-layer) and for  $\theta=55^\circ$  is inter-layer. This results in a greater loss in the forward scattering intensity for the  $\theta=55^\circ$  data if the topmost intact double layer is displaced with respect to the double layer beneath it. For the PH data, the loss in intensity is taken for a large number of different polar angles ranging from  $10^\circ$  to  $90^\circ$ , many of which may not have direct intra-layer or inter-layer forward scattering. For these cases, the total loss in intensity would be due only to the disordered overlayer. Thus, the average value of 2.0-2.4 ML for the disordered overlayer derived from PH is fully consistent with our XPD results for a model in which there is a 2.0-2.5 ML completely disordered overlayer located on a laterally strained double layer which is in turn located on a bulk terminated crystal. Overall, we thus conclude that the best estimate of the fully disordered thickness is 2.0-2.5 ML, or about one double layer.

## References

- [1] E. Tosatti in *The Structure of Surfaces II*, J.F. van der Veen, M.A. van Hove, Eds. (Springer-Verlag, Berlin, 1987) p. 535; J.W.M. Frenken, J.P. Toennies, C. Woll, B. Pluis, A.W. Denier van der Gon, and J.F. van der Veen in *The Structure of Surfaces II*, J.F. van der Veen, M.A. van Hove, Eds. (Springer-Verlag, Berlin, 1987) p.545; A. Trayanov and E. Tosatti in *The Structure of Surfaces II*, J.F. van der Veen, M.A. van Hove, Eds. (Springer-Verlag, Berlin, 1987) p.554.
- [2] C.S. Fadley, *Physica Scripta* T17, 39 (1987); C.S. Fadley, in *Synchrotron Radiation Research: Advances in Surface and Interface Science*, R.Z. Bachrach, Ed. (Plenum Press, New York, 1992).
- [3] A. Szoeké, in *Short Wavelength Coherent Radiation: Generation and Applications*, D.T. Attwood and J. Bokor, Eds., AIP Conference Proceedings No. 147 (AIP, New York, 1986).
- [4] J.J. Barton, *Phys. Rev. Lett.* 61, 1356 (1988); J.J. Barton, *J. Electron Spectrosc.* 51, 37 (1990).
- [5] Preliminary accounts of this work based on lower quality Ge 3d data and/or a more limited analysis of the Ge 3p data appear in : T.T. Tran, D.J. Friedman, Y.J. Kim, G.A. Rizzi, and C.S. Fadley in *The Structure of Surfaces III*, S.Y. Tong, M.A. van Hove, D. Takayanagi, and X.D. Xie, Eds. (Springer-Verlag, Berlin, 1991) p. 522; and T.T. Tran, S. Thevuthasan, Y.J. Kim, G.S. Herman, D.J. Friedman, and C.S. Fadley, *Phys. Rev.* B45, 12106 (1992).
- [6] R. Feidenhans'l, J.S. Pedersen, J. Bohr, and M. Nielsen, *Phys. Rev.* B38, 9715 (1988); P.M. Maree, K. Nakagawa, and J.F. van der Veen, *Phys. Rev.* B38, 1585 (1988).

- [7] R.S. Becker, B.S. Swartzentruber, J.S. Vickers, and T. Klitsner, *Phys. Rev.* **B39**, 1633 (1989).
- [8] R.M. Feenstra, A.J. Slavin, G.A. Held, and M.A. Lutz, *Phys. Rev. Lett.* **66**, 3257 (1991).
- [9] K. Higashiyama, S. Lewis, R.X. Ynzunza, E.D. Tober, and C.S. Fadley, to be published.
- [10] K. Hricovini, G. Le Lay, M. Abraham, and J.E. Bonnet, *Phys. Rev.* **B41**, 1258 (1990).
- [11] E.G. McRae and R.A. Malic, *Phys. Rev. Lett.* **58**, 1437 (1987); E.G. McRae and R.A. Malic, *Phys. Rev.* **B38**, 13163 (1988).
- [12] M.H. Grabow and G.H. Gilmer, *Surf. Sci.* **194**, 333 (1988); E.G. McRae, J.M. Landwehr, J.E. McRae, G.H. Gilmer, and M.H. Grabow, *Phys. Rev.* **B38**, 13178 (1988).
- [13] F.H. Stillinger and T.A. Weber, *Phys. Rev.* **B31**, 5262 (1985).
- [14] A.W. Denier van der Gon, J.M. Gay, J.W.M. Frenken, and J.F. van der Veen, *Surface Science* **241**, 335 (1991).
- [15] L.V. Mikheev and A.A. Chernov, *Sov. Phys. JETP* **65**, 971 (1987); A.A. Chernov and L.V. Mikheev, *Phys. Rev. Lett.* **24**, 2488 (1988); A.A. Chernov and L.V. Mikheev, *Physica A* **157**, 1042 (1989).
- [16] U. Breuer, O. Knauff, and H.P. Bonzel, *J. Vac. Sci. Technol.* **A8**, 2489 (1990); U. Breuer, H.P. Bonzel, K.C. Prince, and R. Lipowsky, *Surf. Sci.* **23**, 258 (1989).
- [17] G.R. Harp, D.K. Saldin, and B.P. Tonner, *Phys. Rev. Lett.* **65**, 1012 (1990); G.R. Harp, D.K. Saldin, and B.P. Tonner, *Phys. Rev.* **B42**, 9199 (1990).
- [18] S. Hardcastle, Z.-L. Han, G.R. Harp, J. Zhang, B.L. Chen, D.K. Saldin, and B.P. Tonner, *Surf. Sci.* **245**, L190 (1991).

- [19] G.S. Herman, S. Thevuthasan, T.T. Tran, Y.J. Kim, and C.S. Fadley, *Phys. Rev. Lett.* **68**, 650 (1992).
- [20] D.K. Saldin, G.R. Harp, B.L. Chen, and B.P. Tonner, *Phys. Rev.* **B44**, 2480 (1991).
- [21] S.Y. Tong, C.M. Wei, T.C. Zhao, H. Huang, and Hua Li, *Phys. Rev. Lett.* **66**, 60 (1991).
- [22] S. Thevuthasan, G.S. Herman, A.P. Kaduwela, R.S. Saiki, Y.J. Kim, W. Niemczura, M. Burger, and C.S. Fadley, *Phys. Rev. Lett.* **67**, 469 (1991).
- [23] C.S. Fadley in *Electron Spectroscopy: Theory, Techniques, and Applications*, C.R. Brundle and A.D. Baker, Eds. (Academic Press, London, 1978) Vol. II, Ch. 1; C.S. Fadley, *Prog. in Surf. Sci.* **16**, 275 (1984).
- [24] J. Osterwalder, M. Sagurton, P.J. Orders, C.S. Fadley, B.D. Hermsmeier, and D.J. Friedman, *J. Electron Spectrosc. Relat. Phenom.* **48**, 55 (1989).
- [25] R. Trehan and C.S. Fadley, *Phys. Rev.* **B34**, 6784 (1986); R. Trehan, C.S. Fadley, and P.J. Orders, *Solid State Commun.* **50**, 315 (1984); R. Trehan, Ph.D. thesis, University of Utah, 1985.
- [26] D.J. Friedman and C.S. Fadley, *J. Electron Spectrosc. Relat. Phenom.* **51**, 689 (1990).
- [27] M.L. Xu and M.A. van Hove, *Surf. Sci.* **207**, 215 (1989).
- [28] M. Sagurton, E.L. Bullock, and C.S. Fadley, *Surf. Sci.* **18**, 287 (1987).
- [29] S.A. Chambers, *J. Vac. Sci. Technol.* **A7**, 2459 (1989).
- [30] Y.V. Naidich, N.F. Grigorenko, V.M. Perevertailo, *J. Cryst. Growth* **53**, 261 (1981).
- [31] R.C. Weast, M.J. Astle, Eds., *Handbook of Chemistry and Physics*, 61st ed. (CRC Press, Boca Raton, 1980).

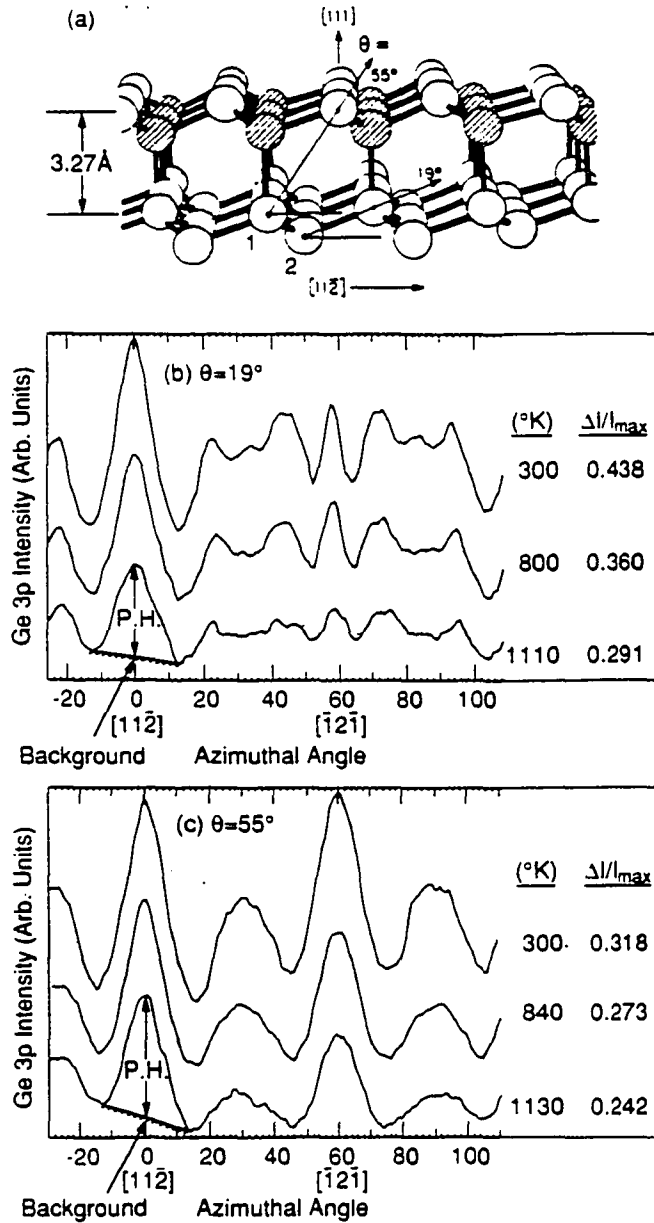


Fig. 4.2.1 (a) An unreconstructed Ge(111) surface showing nearest-neighbor and second-nearest-neighbor scattering directions at takeoff angles of  $\theta=19^\circ$  and  $\theta=55^\circ$  with respect to the surface;  $\phi=0^\circ$  ( $[11\bar{2}]$  azimuth) for both of these directions. Note the two symmetry-inequivalent emitter types. (b) Temperature-dependent azimuthal XPD data for Ge 3p emission from Ge(111) at 1365 eV and a low takeoff angle of  $\theta=19^\circ$ . (c) As (b), but for a takeoff angle of  $\theta=55^\circ$ .

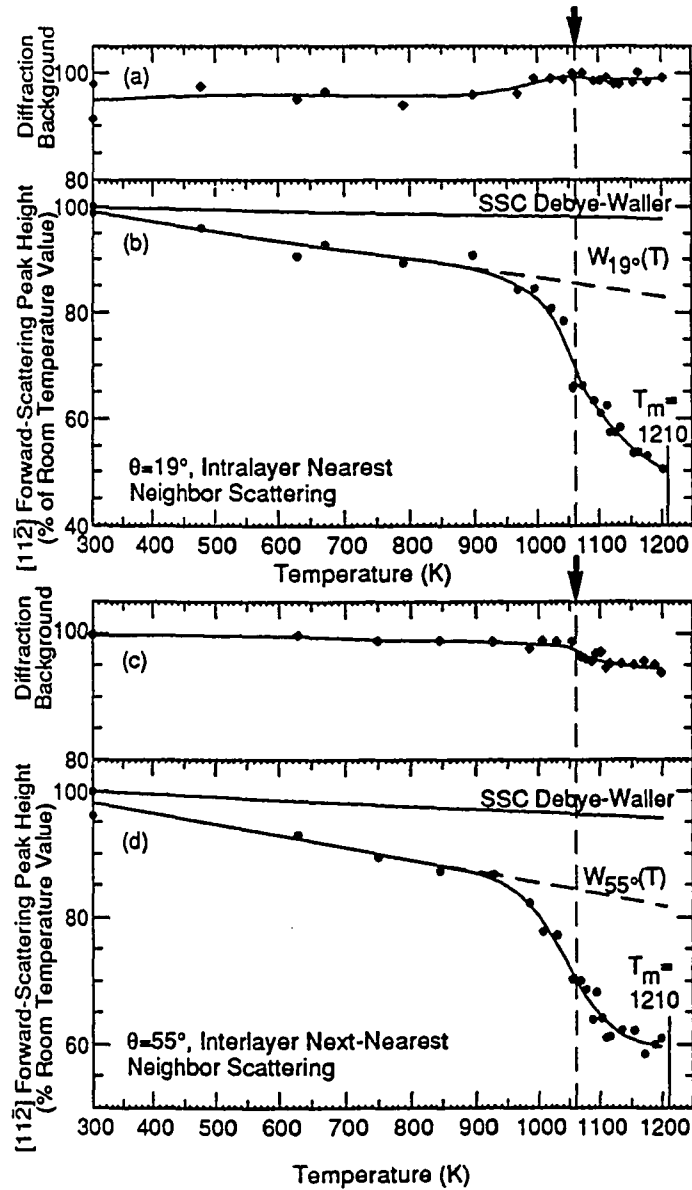
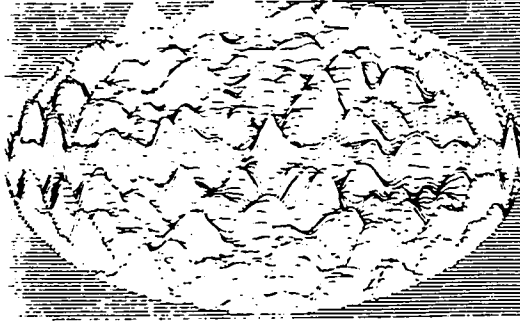
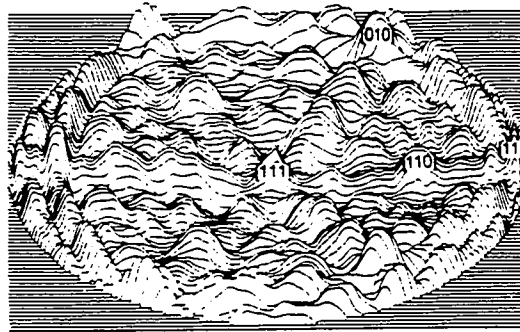


Fig. 4.2.2 (a) Temperature dependence of the background intensity under the nearest-neighbor forward scattering peak in Fig. 4.2.1(b) along  $\theta=19^\circ$ ,  $\phi=0^\circ$ . (b) The temperature dependence of the height  $\Delta I = I_{\text{peak}} - I_{\text{background}}$  of the same nearest-neighbor forward scattering peak.  $\Delta I(T)$  values are plotted as a percentage of the room temperature value. Also shown in (b) is the intensity expected on the basis of Debye-Waller effects in a single scattering cluster model. (c) and (d) are as (a) and (b), but for the next-nearest-neighbor forward scattering peak in Fig. 4.2.1(c) along  $\theta=55^\circ$ ,  $\phi=0^\circ$ .

(a)  $\chi(k_x, k_y)$ , Experiment, 300 K



(b)  $\chi(k_x, k_y)$ , Experiment, 970 K



(c)  $\chi(k_x, k_y)$ , Experiment, 1130 K

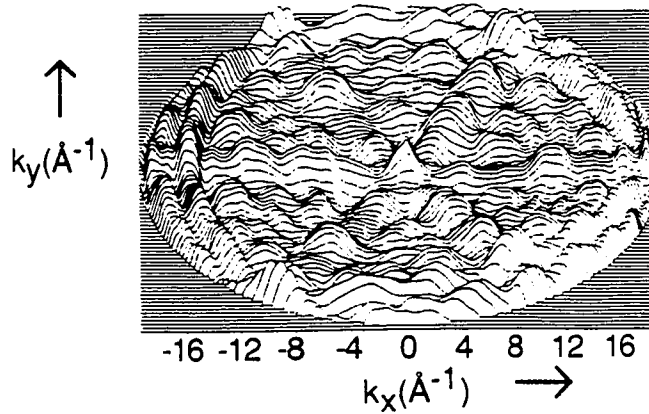


Fig. 4.2.3 (a) Projection of the experimental  $\chi(\vec{k})$  for Ge(111) at 300 K onto the  $k_x$ - $k_y$  plane. (b) As (a), but at 970 K; several low-index directions are labeled. (c) As (a), but at 1130 K.

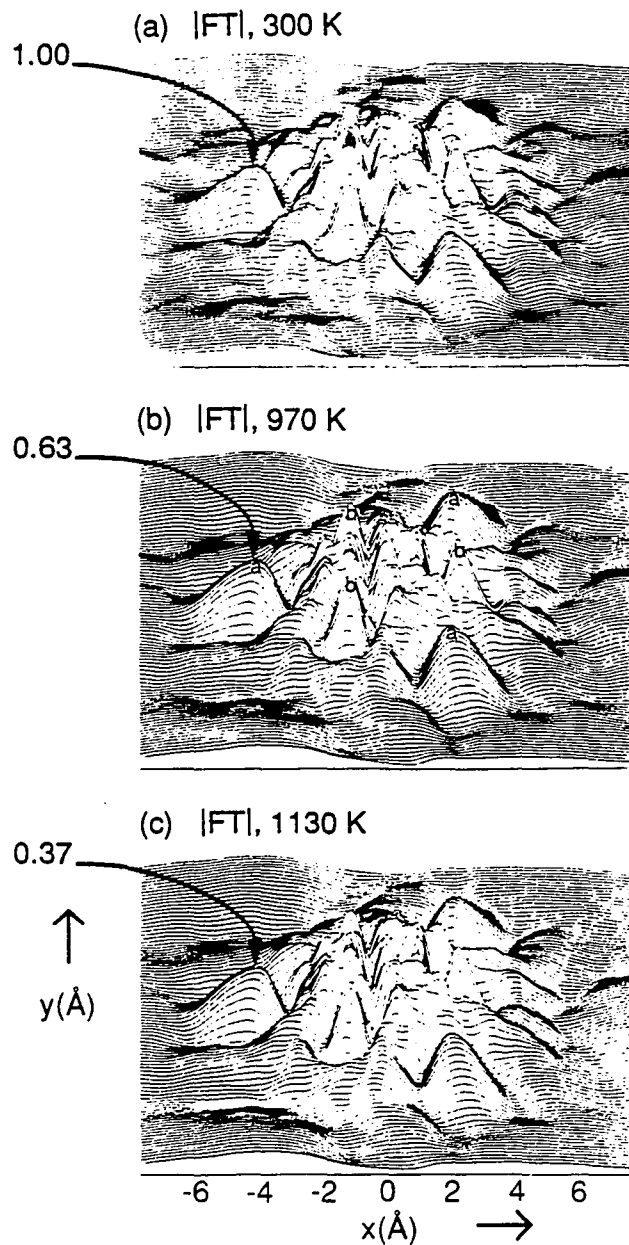


Fig. 4.2.4 Horizontal FT contour plots in the  $z=3.27 \text{ \AA}$  plane obtained with Gaussian removal of forward scattering intensities along low-index directions in the initial  $\chi(\vec{k})$  functions of Fig. 4.2.3 (a-c). Contour plots are shown at (a) 300 K, (b) 970 K, and (c) 1130 K.

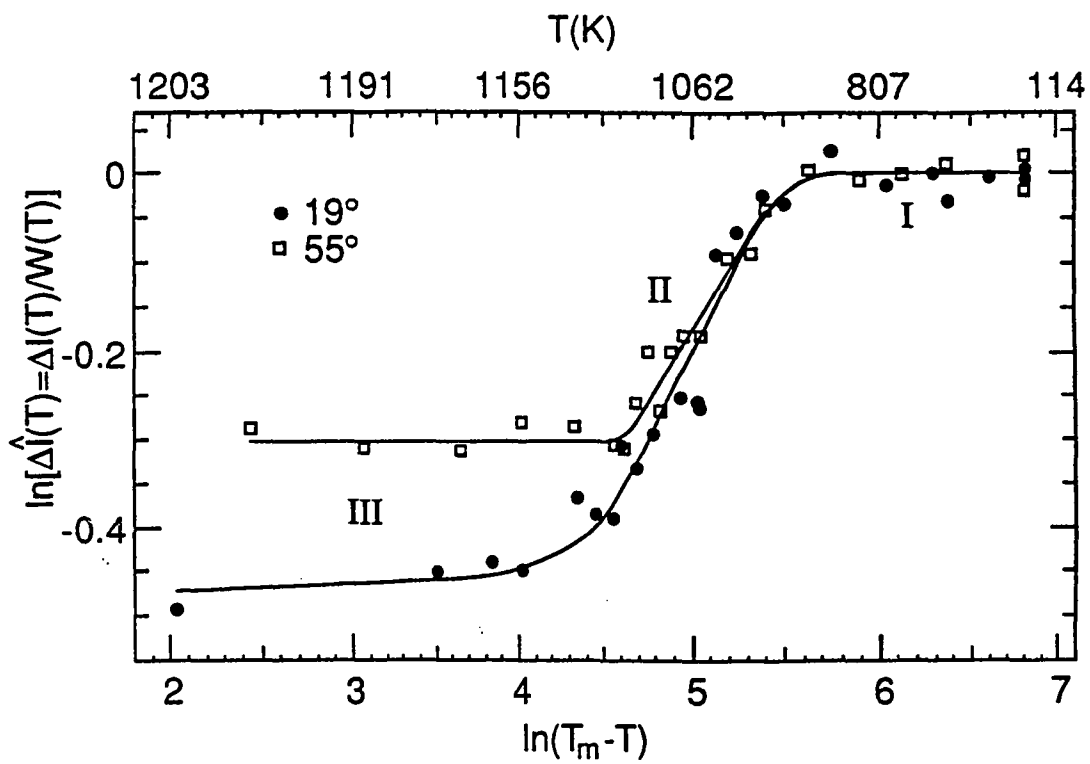


Fig. 4.2.5 Plot of  $\ln\hat{\Delta I}=\ln[\Delta I/W]$ , the vibrationally-corrected intensity change, versus  $\ln(T_m-T)$  for  $\theta=19^\circ$ ,  $\phi=0^\circ$  ( $\bullet$ ) and for  $\theta=55^\circ$ ,  $\phi=0^\circ$  ( $\square$ ).

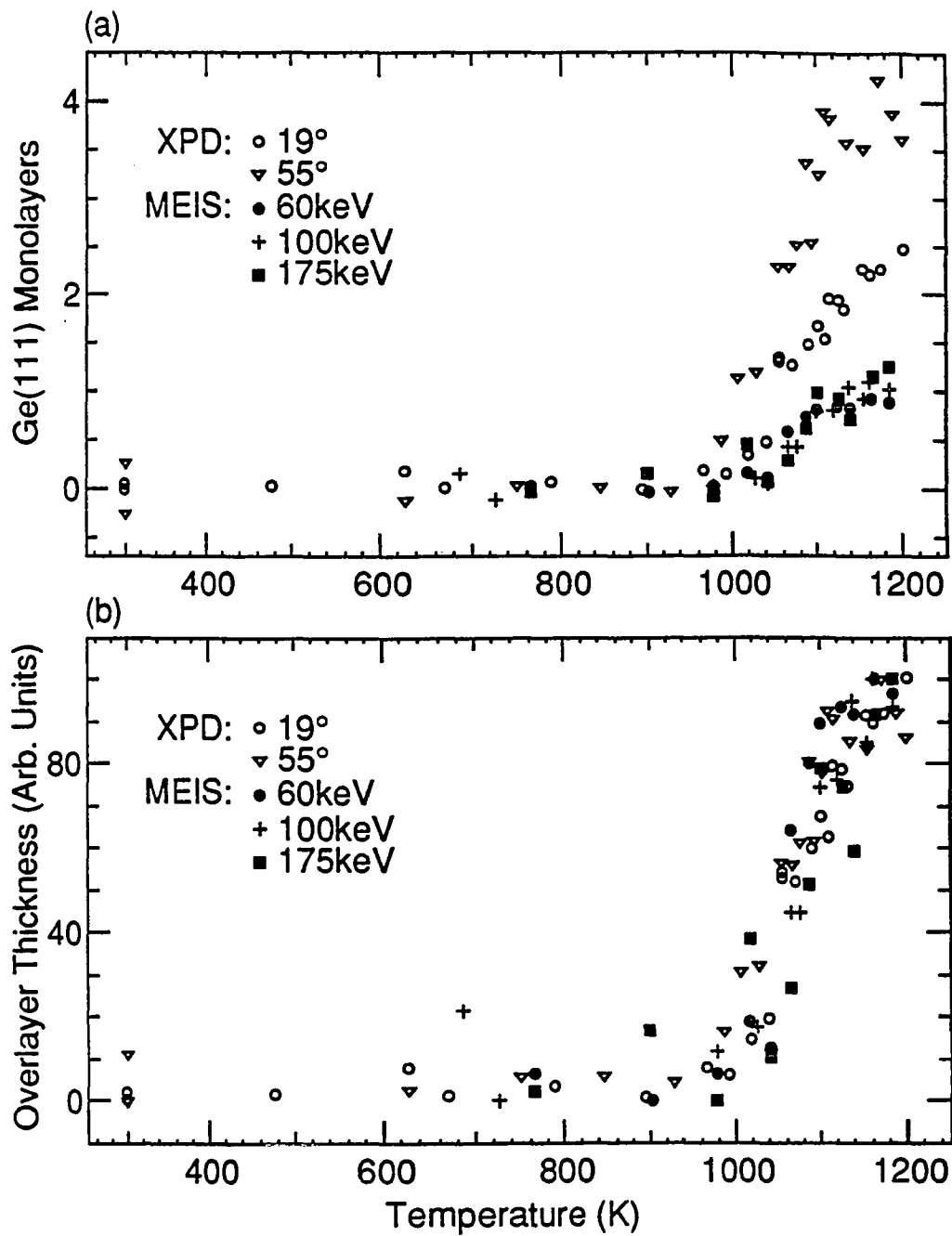


Fig. 4.2.6 (a) XPD and MEIS data plotted as measured overlayer thickness (ML) versus temperature. (b) As in (a) but with XPD and MEIS curves normalized to the same maximum and minimum values. (MEIS data from Ref. 14)

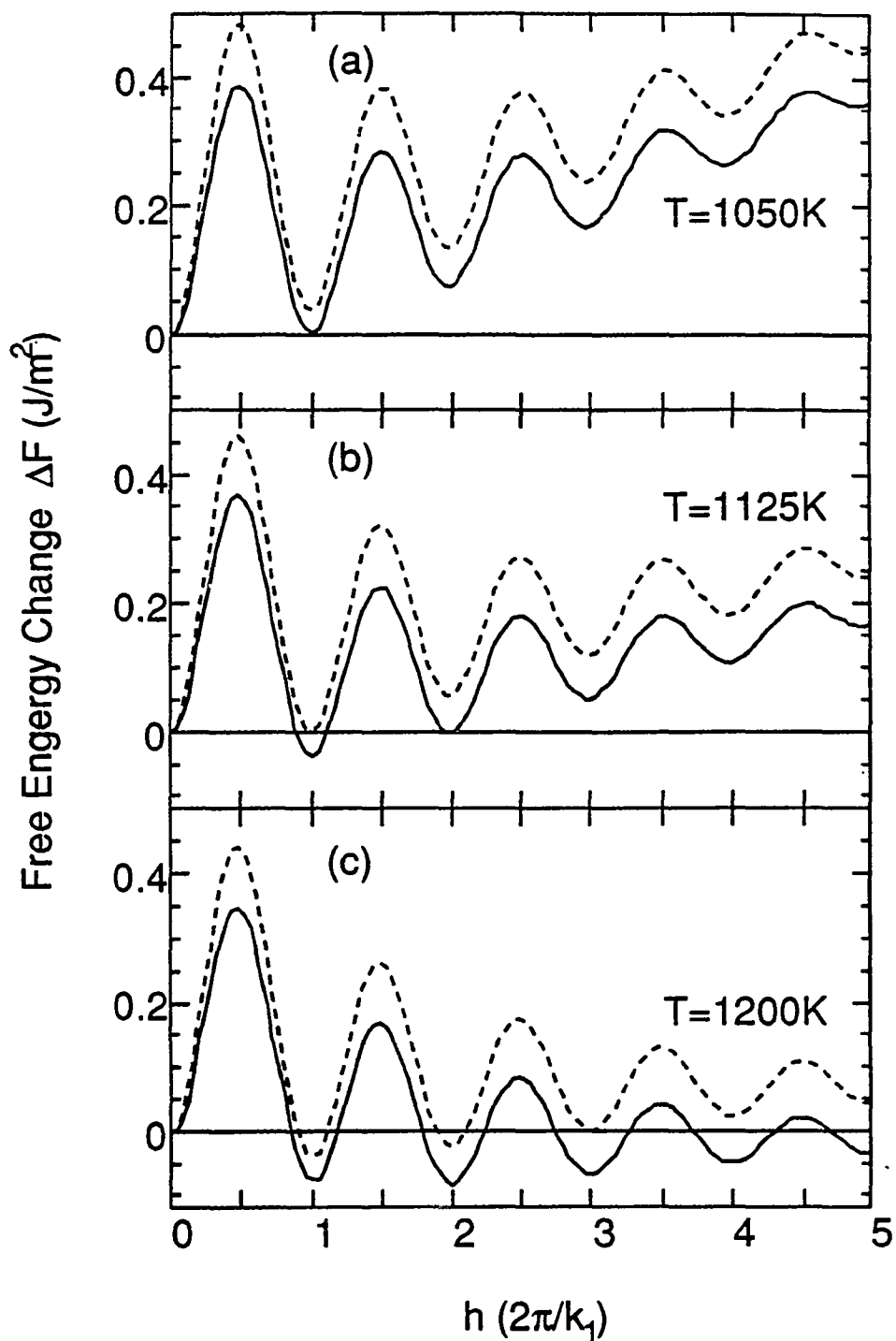


Fig. 4.2.7 Plot of the change in free energy,  $\Delta F$ , as a function of overlayer thickness at 1050, 1125, and 1200 K, as calculated with the model of Mikheev and Chernov [15].

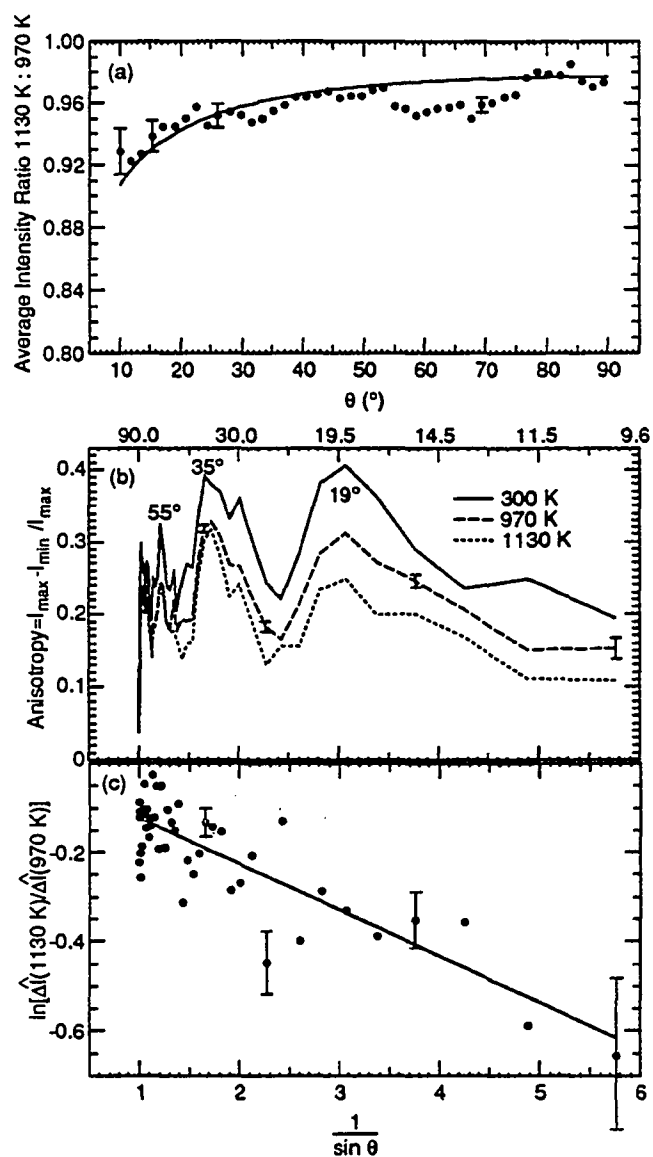


Fig. 4.2.8 (a) The ratio of the average total absolute intensity of each azimuthal scan taken at 1130 K to that of each corresponding azimuthal scan for the same polar angle but taken at 970 K. (b) Overall anisotropies from our holography data at 300, 970, and 1130 K plotted versus  $1/\sin\theta$ . (c)  $\ln[\hat{\Delta I}(1130\text{K})/\hat{\Delta I}(970\text{K})]$  versus  $1/\sin\theta$ ; the best-fit straight line through the data points has a slope of  $-d/\lambda_e = -0.104$ .

## Chapter 5

### Magnetic Disordering: Spin-Polarized Photoelectron Diffraction on MnO and Preliminary Results with Possible Future Applications to Fe and Gd

#### 5.1 Introduction

Multiplet splittings in transition and rare earth metal core-level binding energies for fairly ionic materials are well understood [1,2]. For the outer core levels such as the 3s in the 3d transition metal series the splitting is due to the exchange interaction between the unpaired outermost 3d electrons and the 3s electron remaining after photoemission. These core-level multiplet splittings produce a very highly spin-polarized photoelectron source that is internally referenced to the emitting atom. For certain materials, the large exchange interaction between the highly overlapping 3s and 3d electrons is responsible for the easily resolvable splittings between the different final states of the photoemission process.

An example of such a splitting can be found in the Mn 3s core level of the highly ionic antiferromagnet  $\text{KMnF}_3$ . Fig. 5.1(a) shows the Mn 3s doublet with the single-configuration multiplets primarily responsible for each of the two peaks and the resulting predominant spin polarization. A splitting of 6.7 eV between the two peaks was observed [3] with the spin-down  $^7S$  peak being 71.4% polarized and the spin-up  $^5S$  peak being 100% polarized [4]. Another example is illustrated in Fig. 5.1(b) but this time for the more complex case of a metallic ferromagnet, Fe. Spin-resolved photoemission data for Fe 3s by Hillebrecht et al. show two peaks separated by 4.5 eV [5]. An intensity ratio of 1.16 for the minority- ( $\downarrow$ ) to majority- ( $\uparrow$ ) spin peaks was measured. From an analysis of the line shape of the Fe 3s spectrum, it was further concluded that, although the exchange

interaction may not be the only cause for the splitting, it must be the major contributing factor [5].

In an angle-resolved experiment on single crystals these spin-resolved multiplet-split peaks may behave differently due to spin-dependent scattering effects in the presence of a magnetically-ordered set of scatterers. This phenomenon has been termed spin-polarized photoelectron diffraction (SPPD) by Sinkovic and Fadley [3], who further theoretically predicted that exchange-induced asymmetries as high as 8% would be observable for Mn 3s emission from the antiferromagnet  $\text{KMnF}_3$  if the spin-up and spin-down intensities were scanned in polar angle. Experimentally, spin-up and spin-down photoelectrons from the two dominant peaks in a multiplet can be monitored separately to determine whether there is any difference in their scattering and diffraction due to the presence (or absence) of a magnetically-ordered set of near-neighbor scatterers. Measurements can be made as a function of both direction and temperature.

The first experimental observations of SPPD were made by Sinkovic et al. for  $\text{KMnF}_3$  [6]. The spin-up/spin-down intensity ratio was measured for the temperature range from 95 K to 580 K and for various emission directions. The normalized asymmetry ratios ( $\Delta S_{\text{expt}}$ ) exhibit an abrupt change of -17% and -10% for the two emission directions  $\theta=36^\circ, \phi=0^\circ$  and  $\theta=45^\circ, \phi=0^\circ$ , respectively. In both cases, the point of maximum slope in the drop occurs at a temperature termed the short-range order transition temperature,  $T_{\text{SR}}$ , of  $240 \pm 5$  K, or 2.7 times the Néel temperature ( $T_{\text{N}}=88$  K) for this material.

More recently, the antiferromagnet  $\text{MnO}$  was studied in detail by Hermsmeier et al. [7] in the temperature range from 70 to 750 K, in experiments on which the author of this dissertation was a collaborator. For  $\theta=90^\circ, \phi=0^\circ$  (normal emission), a  $\Delta S_{\text{expt}}$  of about -11% centered at 540 K and for  $\theta=75^\circ, \phi=0^\circ$ , a  $\Delta S_{\text{expt}}$  of +15% centered at 520 K were

observed; these results are summarized in Fig. 5.2. These temperatures correspond to approximately 4.5 times the Néel temperature of MnO.

From these results it was deduced that the sharp changes in the spin-up/spin-down intensity ratio observed may be due to short-range magnetic transitions since photoelectron diffraction is a very short-range order probe. More specifically, they led to the conclusion that short-range antiferromagnetic order persists up to approximately  $2.7 T_N$  for  $KMnF_3$  and up to  $4.5 T_N$  for MnO, where it abruptly disappears. Such a sharp loss of short-range order at high temperature has not been predicted by any prior theory. Moreover, it was further noted that the transition temperatures obtained from these SPPD data are very close to the relevant Curie-Weiss constants [7], although no firm theoretical foundation for this near identity has as yet been found.

These experimental results, together with extensive theoretical diffraction calculations modeling SPPD in terms of exchange scattering effects [3,7,8] clearly indicate that SPPD is a unique probe of magnetic short-range order. Despite the requirement of using synchrotron radiation in order to both tune electron kinetic energies to about 100 eV where magnetic effects are larger, and to yield spectra with better peak-to-background ratios for measuring very small effects, SPPD possesses several advantages. Its non-spin-dependent counterpart, PD, is also inherently a very short-range probe primarily sensitive to the first few spheres of neighbors. Thus PD and SPPD should be ideally suited for studies of short-range structural order and short-range magnetic order, respectively. The data can, in some cases, be interpreted using simple single scattering theory. The ability to change photon energy and emission direction permits a variation in the degree of surface sensitivity. The strongly directional effects observed in diffraction peaks should also allow studies of anisotropic media such as magnetic surface layers. The short time scale involved in this method ( $10^{-16}$ - $10^{-18}$  sec.) provides a snapshot of spin configurations. Finally and

most importantly, since no external spin detector is needed and since the photoelectrons are internally referenced with respect to the emitter, both antiferromagnets and ferromagnets can be studied and, if short-range order is present, it can be measured at temperatures above the Néel temperature for antiferromagnets and above the Curie temperature for ferromagnets.

With this last point in mind, it was the goal of this project to explore the interesting new physics of short-range magnetic order as manifested through SPPD data. First, we extended the work on MnO by using synchrotron radiation to reproduce earlier data and by varying photon energy to determine to what degree the short-range order transition observed is a surface effect. The next logical point of interest was to measure SPPD effects in ferromagnetic systems. Fe and Gd were the candidates for this attempt. Eventually, a complete set of SPPD data for KMnF<sub>3</sub>, MnO, Fe, and Gd as a function of temperature, emission direction, and photon energy would serve to establish both the systematics of the technique and its range of utility, while at the same time probably providing additional provocative data on the existence of short-range order at higher temperatures.

## 5.2 Experimental

Experimental data presented in this chapter for both MnO and Fe were obtained with an angle-resolved 127° cylindrical electron analyzer and the 15° toroidal grating monochromator at the SA73 synchrotron radiation beamline of the Super-ACO storage ring at LURE, Orsay, France. Preliminary XPS spectra for Gd were taken on a VG ESCALAB5 spectrometer equipped with a Surface Science Laboratories Model 3390 multichannel detector, using standard Al K $\alpha$  radiation for excitation. In all cases, a base pressure of  $5 \times 10^{-11}$  torr was maintained in the chamber during data acquisition.

The MnO specimen was a well-characterized single crystal wafer, with  $(100) \pm 0.4^\circ$  surface orientation. This wafer had been used in previous SPPD studies [7]. A standard procedure for sample preparation, involving repeated cycles of Ar<sup>+</sup> bombardment at  $\sim 45^\circ$  incidence and 500-V energy followed by annealing at  $\sim 900$  K, eliminated all surface impurities commonly found such as carbon, silicon, potassium, calcium, and aluminum.

The Fe specimen was a (100) single crystal of 7.1 mm diameter x 1.25 mm thick in dimensions and 99.95% in purity, obtained commercially from Electronic Space Products International. It was polished with 200, 320, 400, and 600 grit CARBIMET<sup>®</sup> silicon carbide paper, followed by METADI<sup>®</sup> diamond abrasive pastes of 15, 6, and 1  $\mu$  in size, and finally by 0.05  $\mu$  BUEHLER<sup>®</sup> Micropolish<sup>®</sup> alumina (Al<sub>2</sub>O<sub>3</sub>). This procedure led to a mirror-finish surface with no imperfections observable through a monocular microscope. The orientation was  $(100) \pm 0.6^\circ$ , as verified by Laue diffraction. Iron single crystals are difficult to clean since the irreversible bcc to fcc phase transition occurs at 1183 K and therefore all cleaning and annealing must be done below this temperature. In addition, they often contain many impurities such as carbon, sulfur, oxygen, nitrogen, phosphorus, chlorine, and silicon. Our actual sample cleaning began with a pretreatment of the crystal in hydrogen to remove those impurities that form volatile hydrides. This was done by H. Viehhaus at the Max-Planck-Institut für Eisenforschung GMBH. Prior to synchrotron radiation experiments, the crystal was also exposed to repeated cycles of argon-ion sputtering and annealing in UHV for one week. At LURE, after periods of data acquisition at high temperatures, it was found that trace amounts of Si segregated to the surface. It was necessary, therefore, to ion bombard the sample at 910-1120 K for 60 minutes ( $10^{-5}$  torr Ar<sup>+</sup>, sample current of 6  $\mu$ A,  $45^\circ$  off normal-incidence), then at 300 K for 30 minutes, and to flash anneal it at 910-1120 K for 5 minutes between series of high-temperature

scans. The temperatures used for cleaning and annealing were chosen to correspond with the temperatures at which these high-temperature scans were taken.

The Gd specimen was cut from 0.25 mm thick polycrystalline foil of 99.9% purity, obtained from Johnson Matthey Inc.. Sample preparations also included ion bombardment at  $10^{-5}$  torr  $\text{Ar}^+$ , 500 V,  $45^\circ$  off normal-incidence for extended periods of time. The purpose of this experiment on Gd was to obtain preliminary information on the splittings of the Gd 4s and 5s doublets in preparation for future SPPD experiments. A single crystal sample and extensive cleaning and annealing procedure were therefore not necessary.

### 5.3 Results and Discussion

#### 5.3.1 MnO(001)

There were two separate synchrotron radiation experimental runs at LURE for MnO in March and May of 1989. The data obtained from the March experiment can be divided into three parts: 1) determination of  $T_{SR}$  for the normal emission direction using a series of scans from high to low temperature of the Mn 3s doublet, 2) study of the behavior of the abrupt step in the spin asymmetry versus temperature curve at  $T_{SR}$  as a function of the polar angle,  $\theta$ , and 3) examination of the effect on the polar scans as a result of changes in photon energy.

First, data for the normal emission direction as a function of temperature are summarized in Table 5.1. Intensity ratios,  $R = {}^5S$  (spin-up peak) to  ${}^7S$  (spin-down peak), were obtained from a Gaussian/Lorentzian curve fitting and spin asymmetries  $S_{\text{expt}}$  were obtained from the equation [7]:

$$S_{\text{expt}}(\text{LT}) (\text{in } \%) = 100 [(R_{\text{LT}} - R_{\text{HT}})/R_{\text{HT}}] \quad (5.1)$$

where  $R_{HT}$  represents the  $^{55}\text{S}:^{57}\text{S}$  intensity ratio for the highest-temperature data point in the series (assumed to be in the fully disordered or paramagnetic limit) and  $R_{LT}$  represents the same ratio for any lower-temperature data point below HT. From the data,  $R_{HT}$  was estimated to be 0.614. Fig. 5.2 shows the excellent agreement between this work and previous results obtained using standard Mo  $M\zeta$  radiation [7]. Second, the study of the behavior of the abrupt step in the spin asymmetry curve versus temperature at  $T_{SR}$  as a function of the polar angle,  $\theta$ , was done by taking polar scans at different temperatures. Due to the limited amount of beam time, data acquisition was limited to three temperature values: 373, 473, and 573 K and four theta values: 90, 75, 60, and 45°. Further problems of charging made it difficult to obtain results at 373 K. A plot of the  $^{55}\text{S}:^{57}\text{S}$  intensity ratio versus theta is shown in Fig. 5.3. At all three temperatures, there is a general increase in the  $^{55}\text{S}:^{57}\text{S}$  intensity ratio as the polar angle is increased from  $\theta=45^\circ$  to  $\theta=90^\circ$  (the surface normal). At each polar angle, however, the  $^{55}\text{S}:^{57}\text{S}$  intensity ratios do not exhibit a consistent dependence on temperature. The existing data are not sufficient to yield conclusive, systematic trends. Finally, no systematic variations could be found in the limited photon-energy-dependent data available. This is partly due to the difference in the background at  $h\nu = 150$  eV, which is steep, and at  $h\nu = 170$  eV which is flat, resulting in inconsistencies in the curve fitting.

The aim of the second synchrotron radiation experimental run on MnO at LURE, carried out in May 1989, was to reexamine the effect of changing the photon energy on the dependence of  $S_{\text{expt}}$  for normal emission on temperature. Fig. 5.4 shows the results taken at  $h\nu = 150$  eV (■) and at  $h\nu = 170$  eV (●). For  $h\nu = 150$  eV,  $S_{\text{expt}}$  values remain relatively constant in the temperature range of 350-500 K. Above this temperature range, there is a slight increase in  $S_{\text{expt}}$  but with a corresponding increase in the scatter of the data points. For  $h\nu = 170$  eV, however, there is a definite decrease in  $S_{\text{expt}}$  with increasing

temperature. The drop is not smooth. Instead, the data suggest a possible step in the temperature region from 500-630 K that may be connected with T<sub>SR</sub> at 530-540 K. Better data will be necessary to confirm this, however.

### 5.3.2 Fe(001)

The next step in our investigation was to attempt to measure SPPD effects in the ferromagnet Fe. In June 1990, available LURE beam time was used to study changes in the spin-split Fe 3s multiplet as the Curie temperature is approached. Twelve temperature series, each one consisting of one initial room-temperature scan followed by one or more high-temperature scans and then a final room-temperature scan, were obtained. The major problem encountered in this experiment is the presence of Si impurity diffusing from the bulk to the surface. In terms of data analysis, this means that the Si 2p peak partially overlaps with the tail of the Fe 3s doublet. The data can be summarized as follows:

- Out of the twelve series, four were eliminated from the analysis due to steep, sloping background problems and/or poor statistics.
- One series shows a decrease in the Fe 3s spin-up/spin-down intensity ratio with an increase in temperature from 300 K to 970 K.
- Three other series are incomplete series. That is, they consist of only one or two out of the three spectra needed: initial room temperature, high temperature, and final room temperature. From various portions of these three series, a very small increase in the spin-up/spin-down intensity ratio can be observed in going from room temperature to 1040 K.
- The four useful sets of data show the same increasing trends in the spin-up/spin-down intensity ratio with increasing temperature. Of these, one series, shown in Fig. 5.5 with

the high temperature scans taken at 1106 K is most complete, has sufficiently good statistics, and will be discussed below:

- The initial room temperature spectrum shows no silicon contamination. The Fe 3s splitting is approximately 4.3 eV with the spin-up peak at  $E_b=101.5$  eV and the spin-down peak at  $E_b=97.2$  eV.
- The first high-temperature spectrum at 1106 K shows no silicon. There is a 5% increase in the intensity of the spin-up peak relative to that of the spin-down peak, as measured with respect to the room temperature spectrum.
- The second high-temperature spectrum at 1106 K shows a Si 2p peak at  $E_b=108$  eV. However, the splitting as well as the relative intensity of the two Fe 3s peaks are in very good agreement with the previous 1106 K spectrum.
- The final room-temperature spectrum shows a strong Si 2p peak which corresponds to an estimate of 9-10% of a monolayer of Si on the Fe(100) surface. The Fe 3s relative intensities, however, do not reproduce those observed in the initial room-temperature scan.

A few general observations can be made from the four useful data sets discussed above. First, the final room-temperature scan does not reproduce the initial room-temperature scan from the same set. In addition to the presence of a Si peak in the final room-temperature scan, there is also an increase in the spin-up/spin-down intensity ratio in the final room-temperature scan relative to that of the initial room-temperature scan. This increase can measure up to 9% and is probably due to the presence of the Si peak. Second, there is a large change in background intensities accompanying a change in temperature. Most high-temperature scans tend to have a higher background than the room-temperature scans. Finally, all high-temperature scans exhibit an increase in the spin-up/spin-down peak ratio relative to the initial room-temperature scan. It is not conclusive, however, that

an SPPD effect is observed. This increase in ratio may be due to the presence of Si and/or background fluctuations accompanying changes in temperature.

This study of Fe thus was not successful in observing SPPD effects unambiguously, but it did assist in identifying what sorts of experimental problems will need to be surmounted in any future study of this system (particularly as to reducing Si impurity levels even further).

### 5.3.3 Gd (polycrystalline)

Finally, an additional specimen of considerable interest is ferromagnetic Gd which would serve as a test case for SPPD in lanthanides. The purpose of this study was to obtain preliminary data on the Gd 4s and 5s multiplets, to determine how well-resolved they are by measuring their splitting, and to suggest which of the two multiplets should be used for future SPPD investigations. Fig. 5.6(a) shows the Gd 4s doublet with a splitting of  $\sim 8$  eV while Fig. 5.6(b) shows the Gd 5s doublet with a splitting of  $\sim 3.4$  eV. These scans were repeated after various cleaning procedures and were found to be very reproducible. The oxygen contaminant level was reduced from 6.6 ML before sputtering cycles began to 1.4 ML by the end of the cleaning procedures. Also, no observable carbon impurity was found at the end of the cleaning procedures. Data acquisition conditions such as x-ray power, pass energy, angular broadening, and slit size were also optimized to yield the highest intensity while keeping a good resolution. The satellite features S<sub>1</sub>, S<sub>2</sub>, and S<sub>3</sub> in the spectra are thought to be due to gadolinium oxide species present in the sample. Since both 4s and 5s doublets ride on approximately similar backgrounds, but the 4s peaks are stronger in intensity than the 5s, and they also exhibit a larger splitting, they should be the choice for future SPPD studies on Gd.

#### 5.4 Conclusions

The temperature-dependent MnO results discussed here confirm prior SPPD observations. The theta- and photon energy- dependent MnO data suggest interesting trends in the  $S_{\text{expt}}$  values with changing parameters. The Fe spectra indicate possible SPPD effects in ferromagnetic materials but they also confirm the inherent difficulties of using Fe due to contaminant diffusion to the surface at high temperatures and the experimental temperature limit imposed by the irreversible bcc to fcc phase transition. Finally, the preliminary Gd 4s and 5s energy scans provide a starting point for future SPPD experiments and afford an alternative ferromagnetic material to the previously examined Fe.

## References

- [1] C.S. Fadley, D.A. Shirley, A.J. Freeman, P.S. Bagus, and J.V. Mallow, *Phys. Rev. Lett.* **23**, 1397 (1969).; C.S. Fadley and D.A. Shirley, *Phys. Rev.* **A2**, 1109 (1970); C.S. Fadley in *Electron Spectroscopy: Theory, Techniques, and Applications*, C.R. Brundle and A.D. Baker Eds. (Academic Press, London, 1978) Vol. II, Chap. 1.
- [2] P.S. Bagus, A.J. Freeman, and F. Sasaki, *Phys. Rev. Lett.* **30**, 850 (1973).
- [3] B. Sinkovic and C.S. Fadley, *Phys. Rev.* **B31**, 4665 (1985).
- [4] G.M. Rothberg, *J. Magn. Magn. Mater.* **15-18**, 323 (1980).
- [5] F.U. Hillebrecht, R. Jungblut, and E. Kisker, *Phys. Rev. Lett.* **65**, 2450 (1990).
- [6] B. Sinkovic, B. Hermsmeier, and C.S. Fadley, *Phys. Rev. Lett.* **55**, 1227 (1985).
- [7] B. Hermsmeier, J. Osterwalder, D.J. Friedman, and C.S. Fadley, *Phys. Rev. Lett.* **62**, 478 (1989); B. Hermsmeier, J. Osterwalder, D.J. Friedman, B. Sinkovic, T. Tran, and C.S. Fadley, *Phys. Rev.* **B42**, 11895 (1990).
- [8] D.J. Friedman, B. Sinkovic, C.S. Fadley, *Phys. Scripta* **41**, 909 (1990); B. Sinkovic, D.J. Friedman, and C.S. Fadley, *J. Magn. Magn. Mater.* **92**, 301 (1991).

Table 5.1 Intensity ratio, R, and spin asymmetry,  $S_{\text{expt}}$ , from Mn 3s versus temperature, listed in the time sequence the data points were taken.

Temperature (K)	Intensity Ratio, R	Spin Asymmetry, $S_{\text{expt}}$
683	0.601	-2.11
628	0.628	2.27
578	0.611	-0.49
523	0.655	6.60
478	0.689	12.15
423	0.685	11.56
599	0.637	3.68
513	0.669	8.96
373	0.709	15.52
573	0.621	1.16
478	0.688	12.09

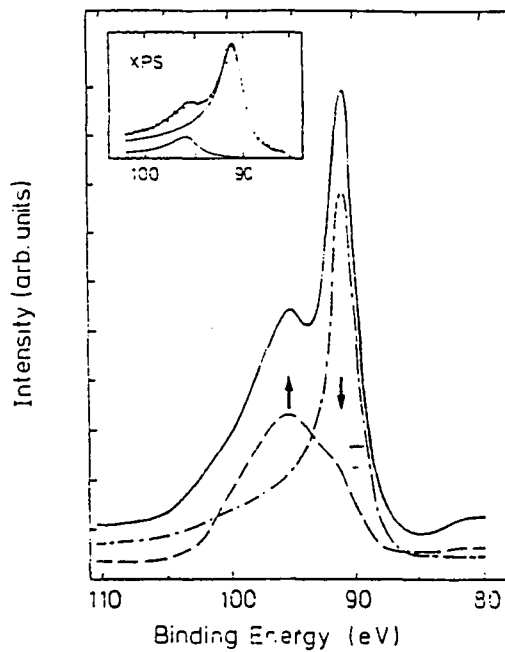
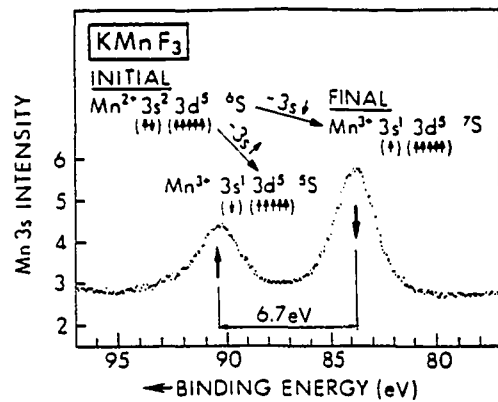


**Fig. 5.1** (a) The multiplet-split Mn 3s spectrum of  $\text{KMnF}_3$ , with the initial and final states and the predominant photoelectron spin orientations indicated (from Ref. 3). (b) Spin-integrated (solid line) and spin-resolved (dashed lines) Fe 3s photoemission spectra after subtraction of background and averaging over the data points (from Ref. 5).

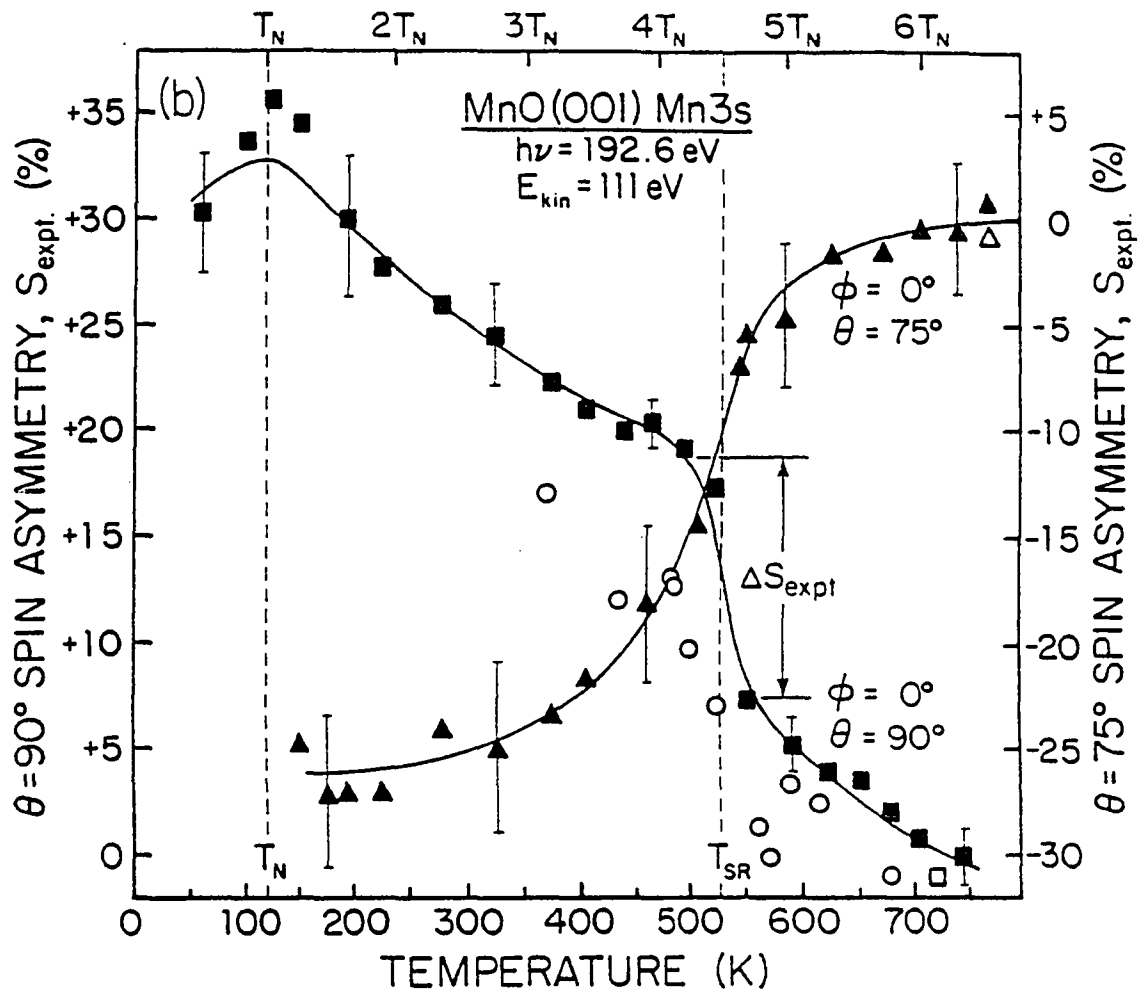


Fig. 5.2 The temperature dependence of Mn 3s spin asymmetries  $S_{\text{expt}}$  for MnO taken with standard Mo  $M\zeta$  radiation ( $\blacksquare$ ,  $\blacktriangle$ ) and with synchrotron radiation (O).

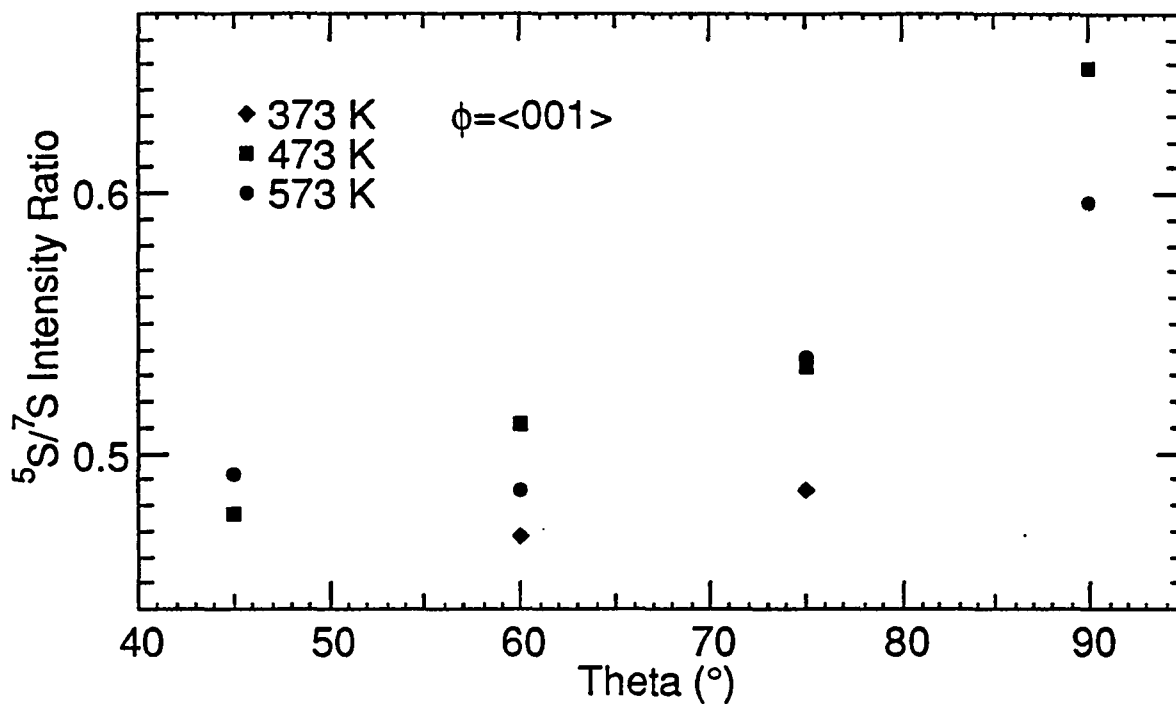


Fig. 5.3 The spin-up/spin-down intensity ratio for the Mn 3s level of MnO as a function of polar angle, taken at three temperatures 373 K (◆), 473 K (■), and 573 K (●).

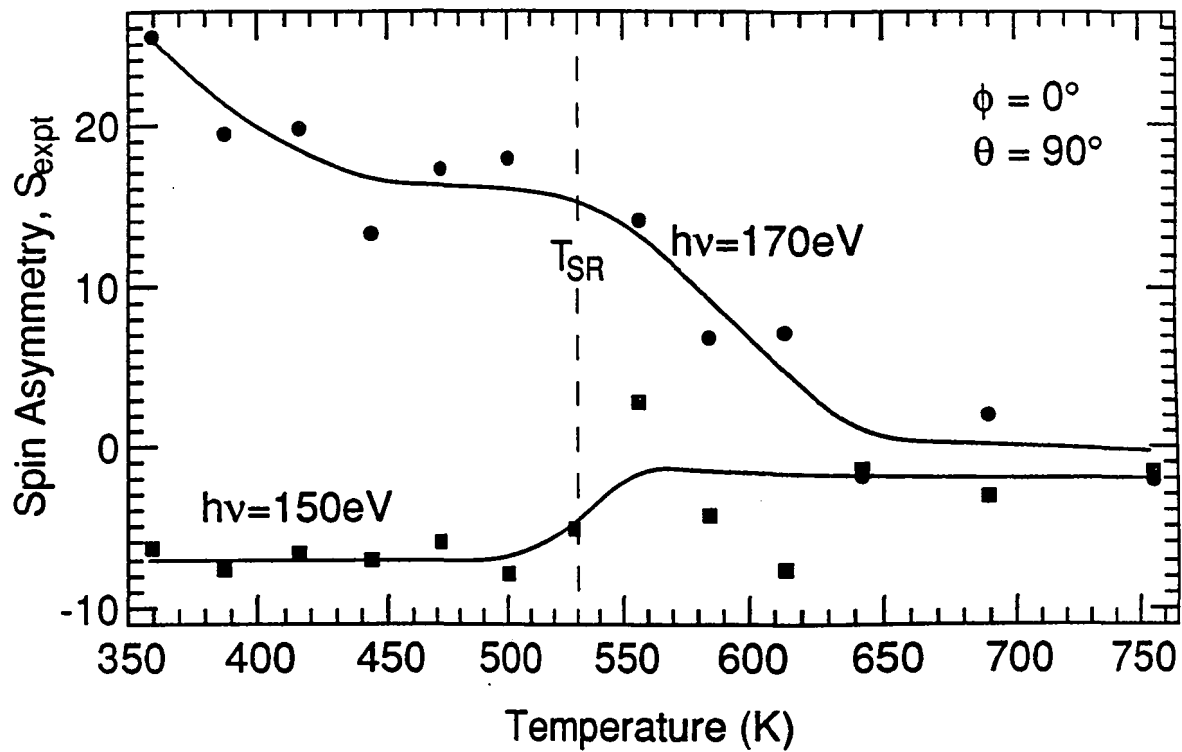


Fig. 5.4 The temperature dependence of Mn 3s spin asymmetries  $S_{sexpt}$  for MnO taken with synchrotron radiation at  $h\nu$  of 150 eV (■) and 170 eV (●).

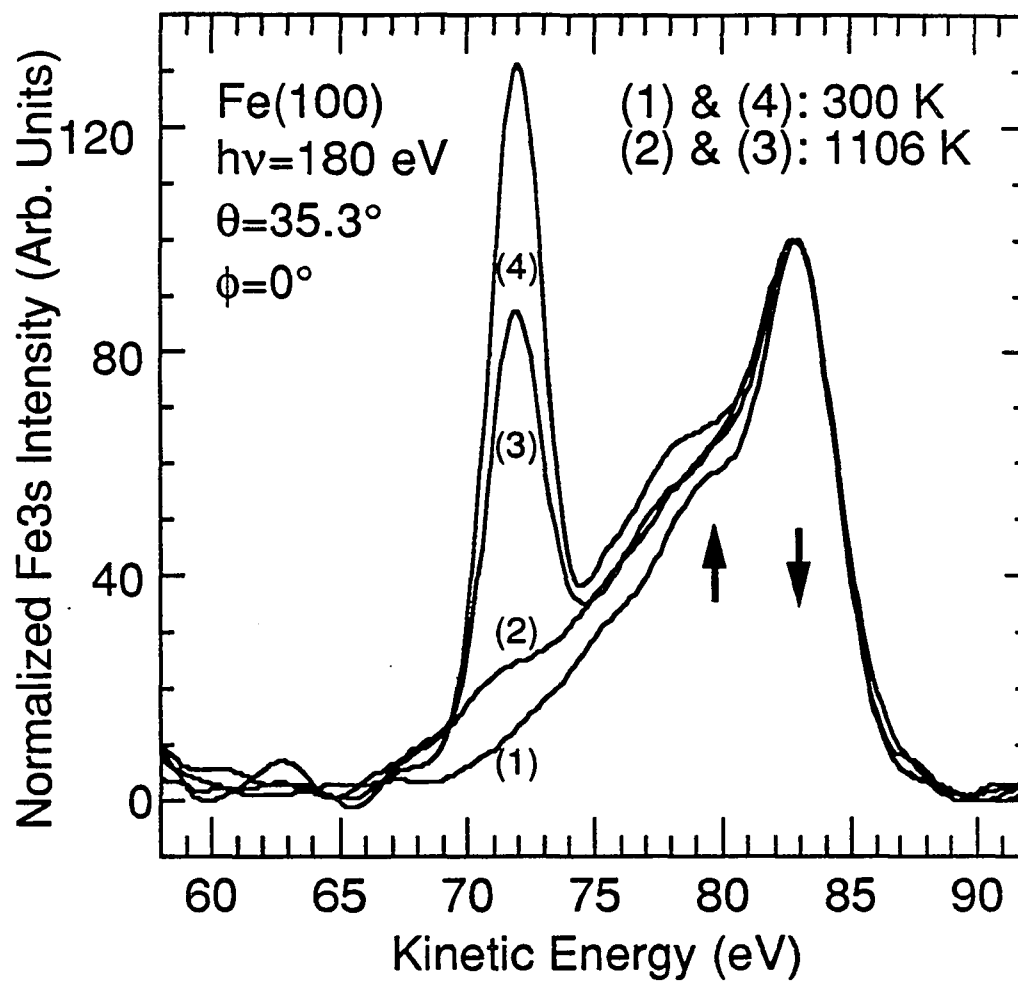


Fig. 5.5 Fe 3s spectra taken four times and at two different temperatures (room temperature and 1106 K) during a single run: (1) = initial room temperature, (2) = first 1106 K, (3) = second 1106 K, and (4) = final room temperature.

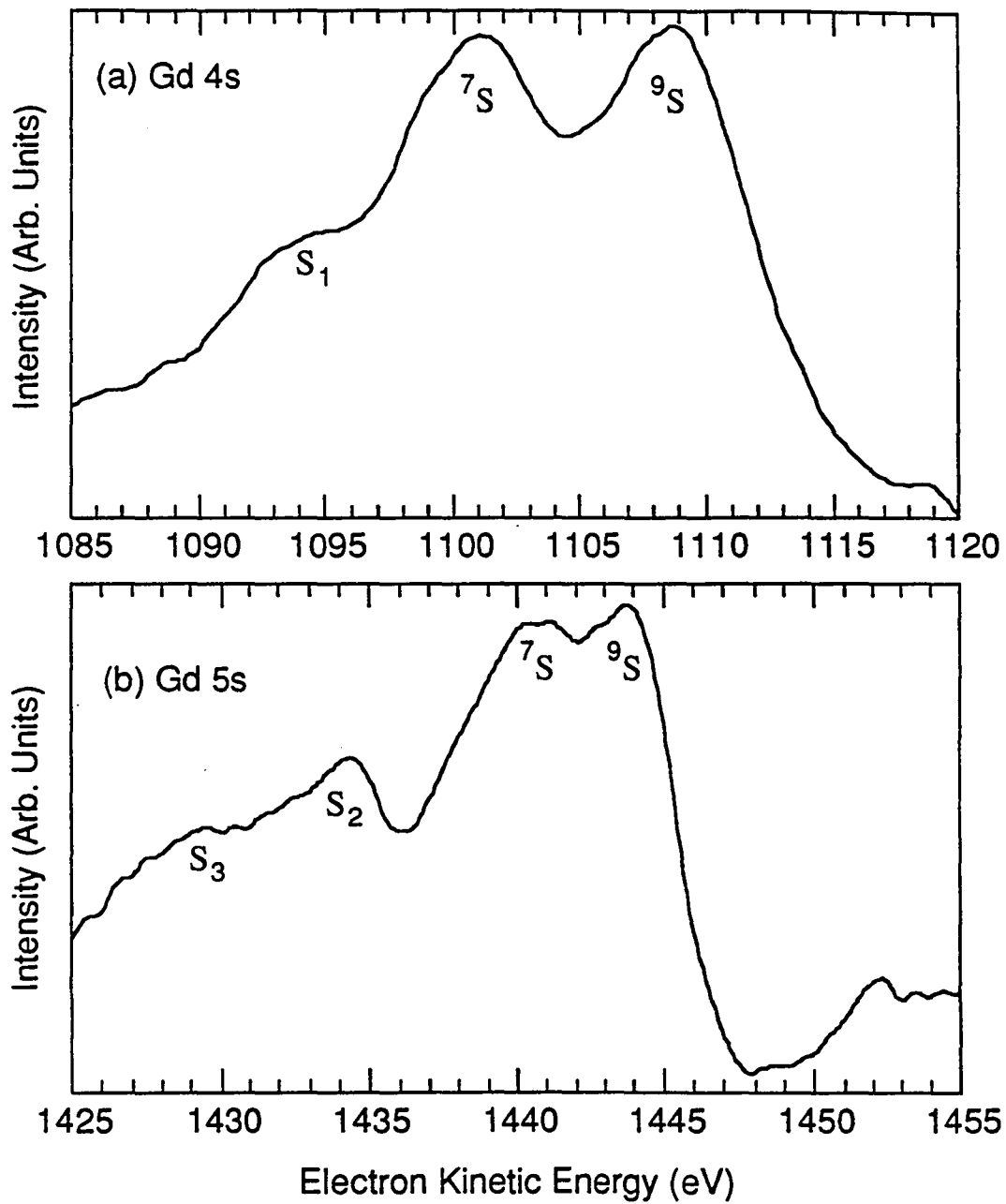


Fig. 5.6 (a) Gd 4s doublet and (b) Gd 5s doublet, as excited by Al K $\alpha$  radiation.

## Chapter 6

### Concluding Remarks

The physical phenomena of disordered surface and near-surface systems, together with the models and theories used to describe them, encompass a very large subject of considerable interest. The advent of modern surface science techniques has transformed many of these ideas into concrete and plausible experiments. While it is true that no single technique can yet provide a definitive description of a disordered system, a combination of several techniques along with their respective collection of experimental data and theoretical analyses may permit consensus on models for such physical phenomena. In this dissertation, two types of disordering were examined: structural and magnetic.

For the first case, the Ge(111) high-temperature surface phase transition was explored using XPD and its new variant, PH. An analysis of our data in light of existing results from other techniques such as LEED and MEIS on the same system led to a model in which, at 160 K below  $T_m$ , the bulk-terminated Ge surface is covered by a laterally strained double layer below another liquid-like disordered double layer of Ge atoms.

For the second case, the loss of short-range magnetic order in the antiferromagnet MnO was confirmed, and attempts to measure similar effects in the ferromagnets Fe and Gd were made. The Fe results were rendered ambiguous by the presence of Si contaminant. Although minute in amount, Si has a 2p peak which unfortunately overlaps with the Fe 3s doublet being measured. It is hoped, however, that the results accumulated will serve as a foundation from which future SPPD studies can originate.

Overall, the work presented here has validated the usefulness of PD and its two variants, PH and SPPD, in a wide range of systems and phenomena despite their relatively recent introduction to the previously existing array of surface science tools. Along with SS

and MS cluster calculations, PD, PH, and SPPD have provided unique information covering the nature of a variety of systems and phenomena including adsorbate/substrate systems, metal-semiconductor interfaces, clusters, and structural as well as magnetic phase transitions. For the future, with the increased availability of synchrotron radiation and the high brightness of radiation sources which will, in turn, permit better energy resolution, PD, PH, and SPPD will continue to expand as powerful probes of surfaces.